Quasi 3D electrochemical and thermal modeling of lithium ion polymer battery in time and frequency domain and its validation

by

Meng Xiao

A dissertation submitted to the Graduate Faculty of
Auburn University
in partial fulfillment of the
requirements for the Degree of
Doctor of Philosophy

Auburn, Alabama
August 3, 2013

Keywords: Lithium ion polymer battery, electrochemical model, heat of mixing, transference number, double layer

Approved by

Song-Yul Choe, Chair, Professor of Mechanical Engineering
Daniel Harris, Associate Professor of Mechanical Engineering
Jeffrey Fergus, Professor of Materials Engineering
Stephen Stuckwisch, Assistant Professor of Mathematics and Statistics

Abstract

A dynamic model for a pouch type Li-polymer battery based on electrochemical, thermal, and double layer principles is developed to analyze static and dynamic performances of a single cell. The model is built in three steps: Firstly, the model for the single cell is a quasi-three-dimensional, constructed by connecting one-dimensional models for micro cells using current collectors. The developed model can represent distributions of temperature, potentials, and current flows along with distribution of lithium ions through the plane. The model is coded using MATLAB and validated against a $LiMn_2O_4$/Carbon pouch type power cell. Secondly, by theoretically analyzing the heat source terms, a new heat generation equation considering heat of mixing and enthalpy is proposed based on energy conservation and integrated into the electrochemical model. A specially designed calorimeter with high accuracy and fast response is used to validate the hypothesis. Finally, potential and ion transport governing equations for double layers and bulk are used to replace the Butler-Volmer and ion transport equation used in electrochemical model, which enables representation of high frequency behavior of a cell. The behaviors of the sub-models are analyzed. The sub-models are integrated into the microcell model that is validated against experiment data collected by EIS.

Table of Contents

Nomenclature

a   Specific surface area for electrode (cm^{-1})

b   Ion mobility ($cm^2 \cdot V^{-1} \cdot s^{-1}$)

c   Concentration ($mol \cdot L^{-1}$)

D   Diffusion coefficient ($cm^2 \cdot s^{-1}$)

E   Energy storage (J)

F   Faraday's constant (96,487 $C \cdot mol^{-1}$)

e   Energy storage density ($J \cdot cm^{-1}$)

i_0 Reference exchange current density ($A \cdot cm^{-2}$)

j   Transfer current density($A \cdot cm^{-3}$)

SOC   State of charge

n   Amount of active electrode material

N   Ion flux ($mol \cdot s^{-1} \cdot cm^{-2}$)

R   Universal gas constant (8.3143 $J \cdot mol^{-1} \cdot K^{-1}$)

T   Cell temperature (K)

U   Standard potential affected by solid concentration (V)

x   Stoichiometric number in negative electrode or coordinate

y   Stoichiometric number in positive electrode or coordinate

W   Work (J)

t_0^+ Initial transference number

Greek symbols

ε Porosity of a porous medium

ϕ Potential in a phase (V)

η Surface overpotential (V)

κ Ionic conductivity of electrolyte ($S \cdot cm^{-1}$)

κ_D Diffusion conductivity ($A \cdot cm^{-1}$)

ρ Density ($g \cdot cm^{-3}$)

σ Conductivity of solid active material ($S \cdot cm^{-1}$)

μ Chemical potential ($J \cdot mol^{-1}$)

Subscripts

a   Anode reaction

B   Bulk

c   Cathode reaction

D   Double layer

e	Electrolyte phase
eff.	Effective
s	Solid phase

1   Introduction

1.1   Background

Energy efficiency of future power systems can be substantially improved using energy storage that can capture energy and retrieve energy that is otherwise dissipated. Batteries are the most preferred energy storage because of high columbic efficiency, high energy and power density. Among different batteries technologies, Li-polymer battery is mostly preferred because of its highest power and energy density, and its drastic price drop that was triggered by the rapidly growing electronic market. The mass production of cells for the consumer electronics ensures a high production volume with increased quality. On the other hand, new applications such as electric and hybrid vehicles require increased power and energy density that is accomplished by employing a large size of active areas by means of wrapping or folding electrodes, electrolytes, and separators together. Dependent upon the way of packaging, the cells can be manufactured into three different types, cylindrical, prismatic, or pouch type. Compared with the cells used for consumer electronics, these high power cells can be quickly degraded and performances might drop fast and becomes unstable because of high ion transport and gradient of ion concentrations and the associated high heat generation in conjunction with varying environmental operating conditions. The working mechanism of a cell is very complex and hard to understand in details, which presents one of technical barriers that prevents from optimal design of a cell and systems. Terminal behavior of a battery cell can be described in three

different ways, using empirical equations, equivalent circuit components, or electrochemical-thermal principles.

1.2 Electrochemical model

Traditionally, empirical or electric circuit model are preferably used for batteries because of simplicity to approximate the terminal behaviors. These approaches enable to describe terminal behaviors, but ignore detailed physical effects that include spacious distribution of charging and discharging ionic and electronic current and the associated temperature rise at different SOC. In addition, operating conditions like cycling, ambient temperature, and storage times cannot be considered. By contrast, the model based on electrochemical-thermal principles can better represent those major effects, but parameters necessary for the model are difficult to characterize and obtain. The electrochemical model known as a thin-film model was proposed by M. Doyle, T. Fuller, and J. Newman [1]. The model was extended by reflecting other cathode materials like $LiCoO_2$, $LiMn_2O_4$ [2] and $LiFePO_4$ [3]. Later, performance of cells for a mixture of two different active materials in electrodes, $Li_yNi_{0.80}Co_{0.15}Al_{0.05}O_2$ and $Li_yMn_2O_4$ was studied [4]. In addition, the model was used to investigate effects of material properties on performance, which include transference number [5], activity coefficient in electrolyte [6], diffusion coefficient in $LiPF_6$ electrolyte [7], and particle size distributions on the discharge capacity [8]. Furthermore, the model was improved by adding the energy equation [9] and the efficiency of batteries during cycling was investigated [10]. Effects of side reactions were also studied [11]. Other studies include relaxation phenomena of a lithium ion battery [12], current limitation on pulse operation [13], degradation of the battery in a pocket computer [14], calculation of heat transfer [15], and optimal design of a battery system used for electric vehicles [16]. However, the research work

2

above has not extended to a high power pouch cell type lithium Polymer battery that is currently widely accepted for applications to electric vehicle (EV) and hybrid electric vehicle (HEV). Therefore, we developed a quasi-three-dimensional dynamic model based on the principles of electrochemical kinetics, mass balances, charge conservations and energy balance. The model is capable of representing ion transport, gradients of ion concentrations and two-dimensional distribution of potentials, current density and temperature as well as terminal voltage and current as a function of time.

1.3 Motivation of the research

This project is supported by General Motor Company, by studying the characteristic and build precise model of high power pouch type Lithium ion batteries they were using in order to design the battery manage system (BMS) that will be used in hybrid vehicles. During the research, it turns out the calculation speed and model stability is important issues need to be solved. In addition, some unclear mechanisms are revealed such as the disagreement of computed individual heat source terms with the total heat generation and the absence form of electrochemical impedance spectroscopy (EIS) expression in electrochemical model.

1.4 Objectives and Dissertation Structure

The objectives of the this research is to build quasi 3D electrochemical-thermal model for high power pouch type lithium ion battery using Matlab, based on physical principles such as Butler-Volmer kinetics, ion diffusion theory, ohm's law etc. The solver will be self-designed in order to achieve faster speed than the ode function provided by Matlab and easier to integrate

into onboard computers. And the thermal model will be developed which can precisely predicts the heat generation as well as the temperature distribution of a single cell. In addition, the ion diffusion equation will be altered to be able to present the double layer effect so that the model can match EIS curve. After that, corresponding experiments will be done to validate the model. The basic structure of the dissertation is shown as follows:

1. Introduction

    This section involves the research background, motivation and objectives.

2. Principle of Lithium ion battery

    This section includes the chemistry and structure of a lithium battery, and how it works when charging and discharging.

3. Quasi three dimensional electrochemical-thermal model and experimental validation of micro cell model and single cell model

    The section will describe a micro cell as 1D model that can calculate lithium ion concentrations, potentials and heat generation, and introduce the 2D model spans in the other two dimensions to form single cell model based on the micro cell model. An experiment setup is designed to validate the electrochemical model including the static and dynamic performance of terminal voltage, current and temperature distribution.

4. Thermal analysis

    The heat source terms of li-ion battery are theoretically analyzed. A new formulation is derived based on the energy conservation that includes both terms that are incorporated into electrochemical thermal model. The hypothesis is validated against measurement result from a specially designed calorimeter.

5. High frequency model

A sub-model for the DL and bulk is newly developed and integrated into the electrochemical model for a pouch type LiPB. The integrated model is validated against experimental EIS and time response. The proposing model is capable of representing the responses at charging and discharging not only in time domain, but also in the wide range of frequency domain.

6. Conclusion

2   Principle of Lithium ion battery

The working principle of lithium battery should be discussed from four scales. As shown in Figure 2-1, in decimeter scales, we can design the geometry of the battery and simulate the thermal behavior during charge and discharge; in one tenth millimeter scale, we can calculate the thickness of the electrodes-separator layers according to the energy-power ratio requirement, or study the transport mechanism of lithium ion in materials; surface chemistry and crystal deformation is focused on micron scale; in nanometer scale, the lattice structures of different materials with additives will be the issue in order to improve the capacity of battery or voltage profile.
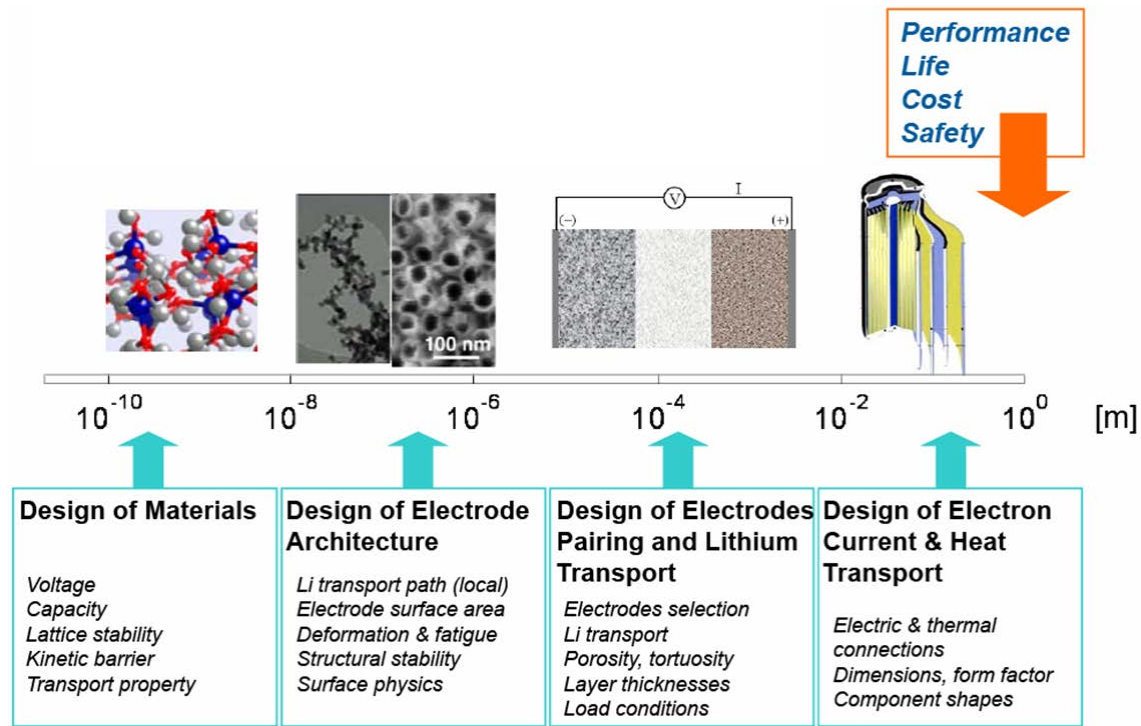
Figure 2-1 Lithium ion battery designing in different scales [17]

2.1 Decimeter scale

Same as other batteries, a Li-ion battery cell consists of electrolyte and two electrodes. The typical prismatic structure of a single cell is shown in Figure 2-2. The grounded electrode material is mixed with polymer binders and pasted onto both sides of current collectors to form double sided electrode thin sheets. Polymer separator is placed between positive electrode sheets and negative electrode sheets alternately. Once the stacked electrodes and separators are wrapped and placed into battery case, the electrolyte is injected and penetrates into pores of electrodes. The upper part of the case is covered by a cap plate and sealing gasket. The cap plate has a safe vent to release any pressure that can be built up during operation. A positive electrode tab and a negative electrode tab are connected to the corresponding current collectors. As a safety

7

precaution, insulation between the electrodes and battery case is used to prevent a potential short circuit.
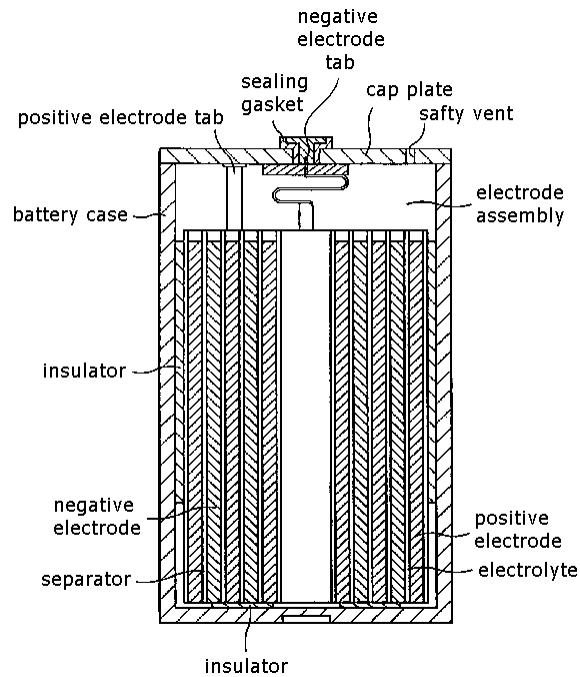
Figure 2-2 Structure of a prismatic Li-ion battery [18]

2.2   One tenth millimeter scale

Figure 2-3 shows the sandwich structure of a micro cell with five layers that are negative current collector, anode, separator, cathode and positive current collector respectively.
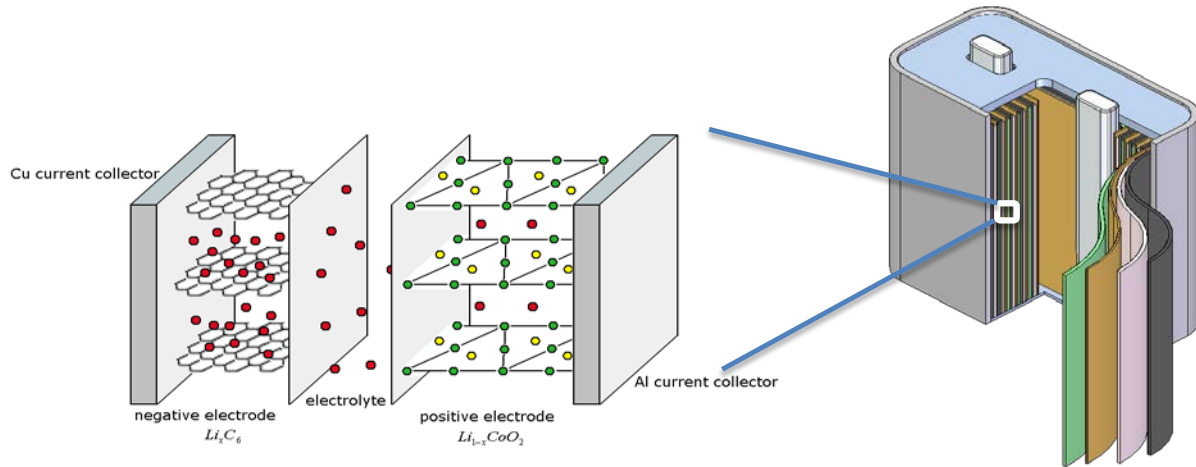
Figure 2-3 Sandwich structure of electrode couple

When a battery is charged or discharged, chemical reactions take place at the interface between electrode and electrolyte. As a result, the electrons and lithium ions will separate at cathode, transport through external circuit and electrolyte respectively to anode and combine again there to complete the total battery reaction.

Theoretically anode and cathode may switch when charging and discharging, but people always call negative electrode as anode and positive electrode as cathode.

Figure 2-4 Paths of anion and cation when battery is operating

The current inside battery is contributed by ion current which flows in electrolyte and the electron current that carried by electrode. In order to have large electrode surface area, the electrodes in high power Lithium ion battery are made porous which allow the electrolyte soak into them. In that case, the electrode area is mixture of electrode and electrolyte so that the ion current and electron current will coexist.
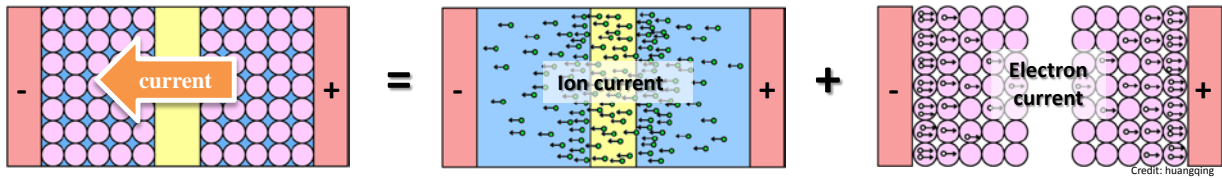
Figure 2-5 current inside battery

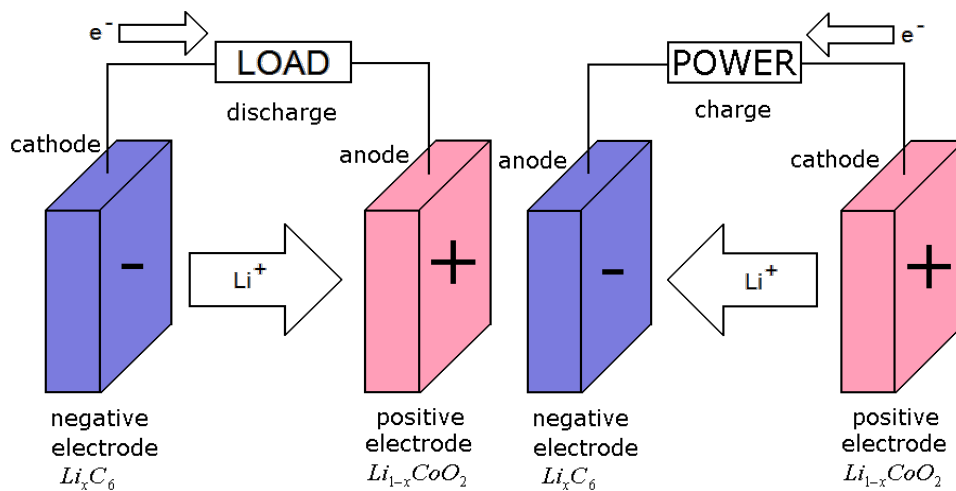The ion transport in the electrolyte can be described using the Nernst-Planck equation.

$$N = j(d) + j(e) = -D_e \frac{dc_e}{dx} - zc_e \frac{D_e F}{RT} \frac{d\varphi_e}{dx} \qquad (2\text{-}1)$$

where j(d) is the flux of diffusive mass transfer, j(e) is the flux of electro-migration mass transfer, N(x) is the mass transfer with unit of $(\text{mol}\cdot\text{m}^{-2}\cdot\text{s}^{-1})$ that presents the amount of certain charges passing through given area per second, De is the diffusion coefficient in electrolyte, $c_e(x)$ is the concentration of lithium ion in electrolyte, $\phi_e(x)$ is the potential of electrolyte, T the temperature, z the number of electrons transferred in the cell reaction, R is the universal gas constant: R = 8.314472 J $\text{K}^{-1}\cdot\text{mol}^{-1}$ and F is the Faraday constant, the number of coulombs per mole of electrons: F = 96485 C$\cdot\text{mol}^{-1}$.

In fact, the electrolyte is stagnant because of non-liquid electrolyte used in the Li battery and thus the mass transfer in the cell is only affected by two factors, the flux of diffusive mass

transfer driven by concentration gradient is represented by j(d) and the flux of electro-migration mass transfer driven by electric field is the second term, j(e).

At an equilibrium state, the ion flux caused by diffusive mass transfer is equal to that caused by electro-migration, which provides the concentration in the electrolyte given in the below. The terminal voltage is determined by the charges present in the anode and cathode side.

$$0 = \frac{dc_e}{dx} - zc_e \frac{F}{RT} \frac{\varphi_{e-} - \varphi_{e+}}{L_s}$$

$$c_e(x) = const \times \exp(\frac{zF}{RT} \frac{\varphi_{e+} - \varphi_{e-}}{L_s} x)$$

(2-2)

2.3   Micron scale

In this scale, we can see lots of interspaces among the granular crystalline grains from Figure 2-6(b). When the $LiCoO_2$ electrode material is used in lithium ion batteries, $LiCoO_2$ contacts with liquid electrolyte. The liquid electrolyte can soak into the interspaces and directly contacts with the crystalline grains. Thus, the Li^+ in the liquid electrolyte can easily diffuse throughout the $LiCoO_2$ electrode, which is beneficial to good electrochemical performance of the material at high current density.
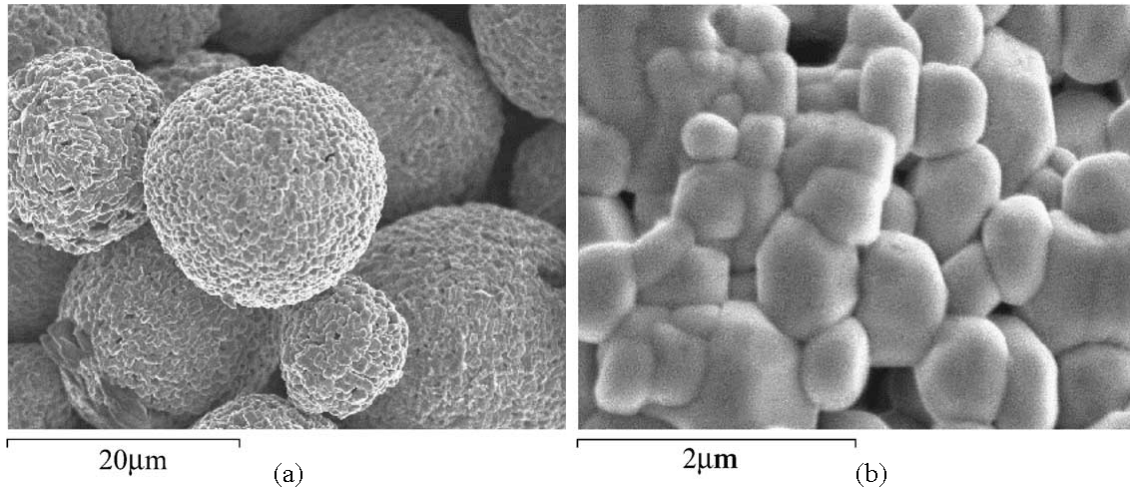
Figure 2-6 SEM images of the $LiCoO_2$ powders [19]

The particle morphology is an important factor on the performance of Lithium ion battery because on one hand, the chemical reactions will take place at the interface between the electrode particles and electrolyte so that larger surface area will result in lower overpotential at certain current density and consequentially reduce power loss; on the other hand, side reaction also take place at this interface which will consume active material and eventually cause capacity loss. In addition, the mechanical stress occurred at intercalate and de-intercalate processes will cause particle crack followed by further side reactions at newly formed surfaces and crystal exfoliation which is considered the strongest impact on material change that contribute to cell aging. [20]

In recent years, the commonly used materials for anode are graphite, Sn and Si-based alloys, Metal oxides and $Li_4Ti_5O_{12}$ spinel. And the top five cathode materials are Li–S, Li–air, $LiMPO_4$ (M = Mn, Fe, Co), $Li_2MnO_3 \cdot Li[MnNiCo]O_2$ and $LiMn_{1.5}Ni_{0.5}O_4$ [21]. Each material has intrinsic equilibrium potential which is only function of stoichiometry number of lithium in the material. That means at equilibrium state (i.e. no macroscopic current across surface), there is potential difference between electrode and electrolyte which is determined by equilibrium potential and affected by Lithium ion concentration in electrolyte according to Nernst equation. A certain

combination of stoichiometry numbers of two electrodes can determine the potential difference of two electrodes, which in known as open circuit voltage (OCV).
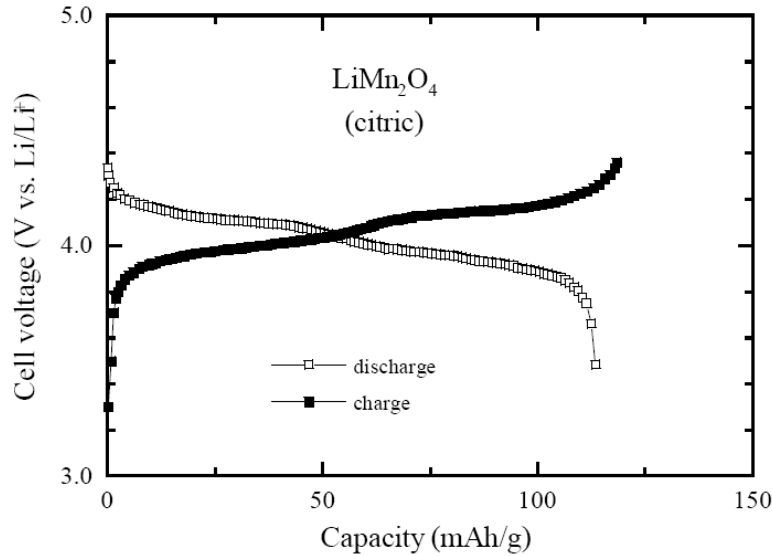
Figure 2-7 Cell voltage vs. charge and discharge capacity of $LiMn_2O_4$ battery [22]

The OCV will change with charging or discharging of the battery as shown in Figure 2-7, after setting the fully charged and fully discharged voltage according the degradation condition, the maximum charge Q_{max} is defined as the charge involved in charging the battery from empty to full or discharge from full to empty. And the state of charge (SOC) is defined as the ratio of useable charge of a battery at certain time to the maximum charge with unit of percentage. At full SOC, anode will have high lithium ion concentration while cathode has low lithium ion concentration, vice versa for zeros SOC. Changing of SOC is equivalent to moving around the Lithium ion between anode and cathode. It worth to mention that the Lithium ion concentration in electrodes never go to maximum value or zeros at any time because people need constraining the concentration in solid to certain range to avoid significant degradation.

Low SOC   Medium SOC   High SOC
charging
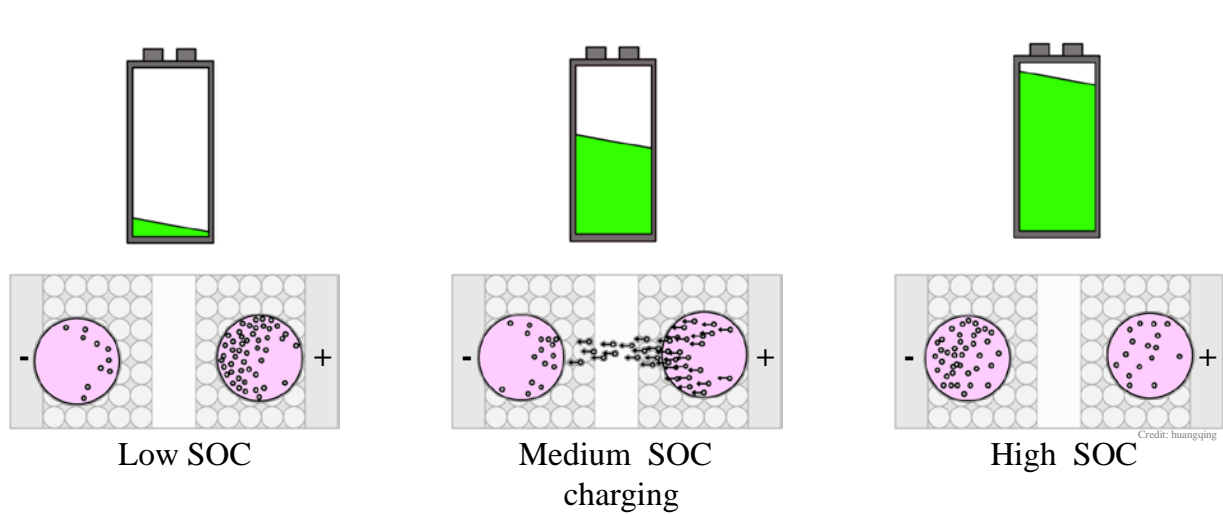
Figure 2-8 SOC and Lithium ion concentration in solid phase

2.4 Nanometer scale

A separated layered structure of a cathode material, $LiCoO_2$, shown in Figure 2-9, indicates the location of atoms of the lithium, cobalt and the oxygen in crystal structure.
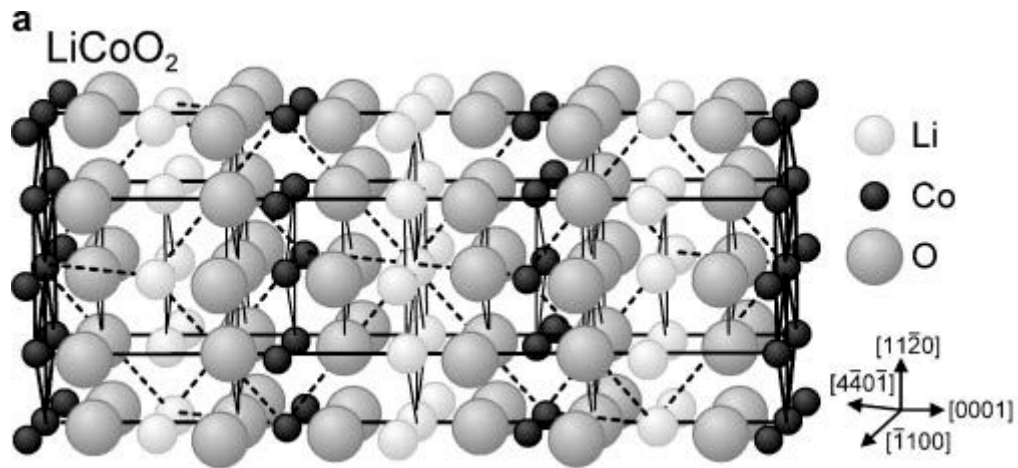
Figure 2-9 Separated structure of $LiCoO_2$ [23]

Another type of cathode material $LiMn_2O_4$ has spinel structure shown in Figure 2-10
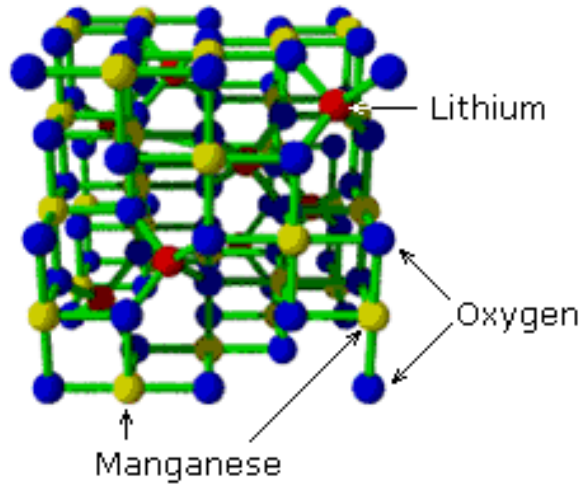
Figure 2-10 Spinel structure of LiMn$_2$O$_4$

Take LiCoO$_2$/C battery for example, the half reaction at cathode while charging or discharging (backward) has the following expression

$$LiCoO_2 \leftrightarrow Li_{1-x}CoO_2 + xLi^+ + xe^- \qquad (2\text{-}3)$$
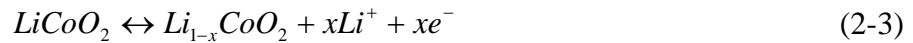
Conversely, the half reaction occurs at anode while charging or discharging (backward) is

$$xLi^+ + xe^- + 6C \leftrightarrow Li_xC_6 \qquad (2\text{-}4)$$

Consequently, the overall reaction becomes

$$Li_{1-x}CoO_2 + Li_xC_6 \leftrightarrow LiCoO_2 + 6C \qquad (2\text{-}5)$$

It should be noted that the lithium ions are not being oxidized during the migration from one electrode to other, while Cobalt is oxidized from Co^{3+} to Co^{4+} during charging, and reduced from Co^{4+} to Co^{3+} during discharging.

However, the crystal lattice likely becomes instable and an irreversible reaction can take place if more than half of the lithium ions are extracted from the electrode. The irreversible overcharging and over-discharging reactions of LiCoO₂ cathode are:

$$\text{Overcharge: } LiCoO_2 \rightarrow Li^+ + CoO_2 + e^-$$

$$(2\text{-}6)$$

$$\text{Overdischarge: } Li^+ + LiCoO_2 \rightarrow Li_2O + CoO$$
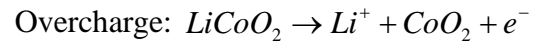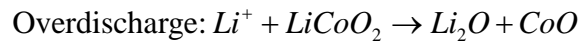
3   Electrochemical-thermal modeling

A pouch type of a single cell and a micro cell are shown in Figure 3-1, respectively. The single cell is assumed to be made of micro cells that are connected in parallel by current collectors of both electrodes.
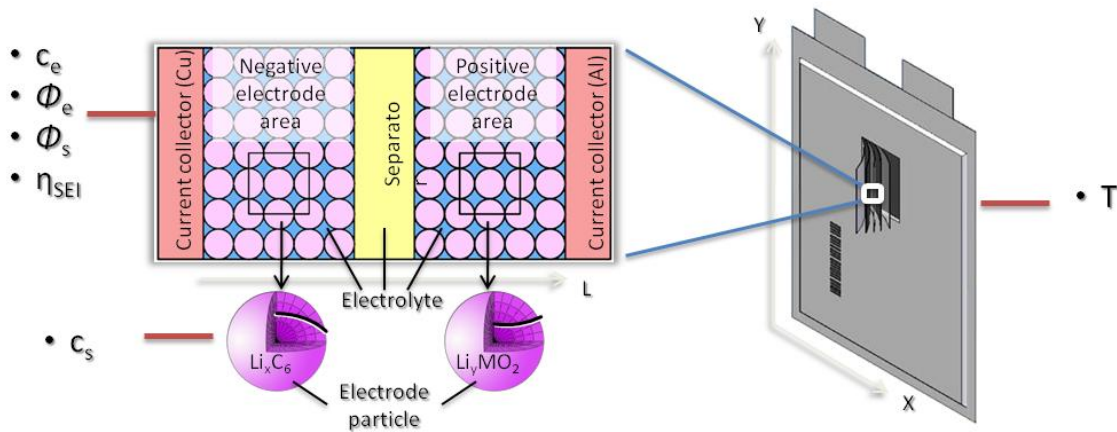
Figure 3-1 A pouch type cell and a micro cell

Each of the micro cells is assumed to be a sandwiched model that is composed of a negative electrode, a separator, and a positive electrode. The materials are porous and equally mixed with electrolyte materials. In addition, particles dispersed at the cathode and anode electrodes have a same radius, r_s, and are in contact with neighboring particles. The working mechanism of the microcell is described using five variables that present concentrations in electrodes and electrolyte, potentials in solid and electrolyte, and overpotentials under isothermal condition. Since the conductivity of current collectors is relatively high, it is assumed that no lateral current flows from one micro cell to another, so all lateral effects can be ignored. In addition, the current

collectors on each layer have the same potential, so that only two current collectors are considered for the model. The micro cell becomes a one-dimensional model. The tab current of the two collectors in the model are obtained by dividing total tab current by the number of layers.

The number of micro cells is equal to that of the grids, given by meshing the single cell. The number of grids in the following calculation is 1900, resulting from 38 divisions in the X direction (x=38) and 50 divisions in the Y direction (y=50). The area of each individual micro cell may be obtained by dividing the cell area by the number of grids.

When ions and electrons are transported though electrolyte and external circuit, chemical reactions will take place at the surface of the electrode particles that contact electrolyte. After the reactions have been completed, the free ions are located in electrodes and diffuse until intercalated. The electrodes are approximated with spheres and it is assumed that the lithium ions diffuse only in the radial direction, driven by the gradient of the Li-ion concentration.

A schematic diagram for the model of a single cell is shown in Figure 3-2, where initial conditions, input variables and parameters for the model, and outputs are included. The parameters used for the model are appended. The input variables are electric loads that can be bi-directional current and voltage as a function of time, while the outputs are responses of the loads in terminal voltage or current, SOC, and temperature distributions as well as other internal variables. In addition, the diagram shows how governing equations of the micro cells are connected each other and with those in the single cell.
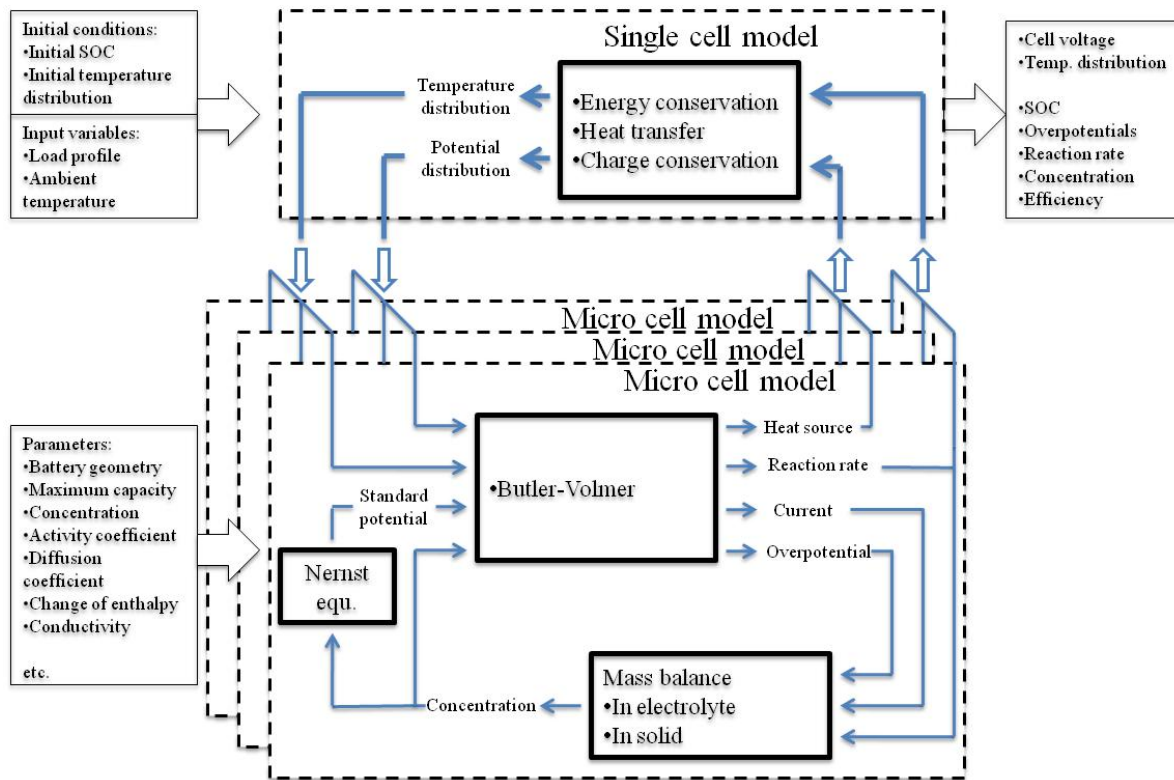
Figure 3-2 Scheme of the model

This section proposed a non-isothermal transient model of PEM fuel cell which is used to be integrated with the FDS. The liquid water dynamics in the gas flow channels, gas diffusion layer and catalyst layer at cathode and anode sides are considered in the model. It is known that the accumulated liquid water in the gas flow channels can block the transport path in the gas diffusion layer for the reactant gases and degrade the performance of the fuel cell, while the proper water amount in the gas flow channels can help to maintain high proton conductivity in the membrane.

3.1 Governing equations

3.1.1 Overpotentials

Current generated by chemical reactions are described by the Butler-Volmer equations, shown in equation (3-1).

$$
j_N^{Li} = a_{S,N} \cdot i_{0,N} \left(\exp\left(\frac{\alpha_{a,N} \cdot n \cdot F}{R \cdot T}(\eta_N - \eta_{SEI}) \right) - \exp\left(-\frac{\alpha_{c,N} \cdot n \cdot F}{R \cdot T}(\eta_N - \eta_{SEI}) \right) \right)
$$

$$
j_P^{Li} = a_{S,P} \cdot i_{0,P} \left(\exp\left(\frac{\alpha_{a,P} \cdot n \cdot F}{R \cdot T}\eta_P \right) - \exp\left(-\frac{\alpha_{c,P} \cdot n \cdot F}{R \cdot T}\eta_P \right) \right) \tag{3-1}
$$

$$
\eta = \phi_s - \phi_e - U
$$

where subscription N and P is the variable in negative or positive electrode, j^{Li} is the current density, i_0 is the exchange current density, a_s is the specific interfacial surface area, ϕ_s is the solid potential, ϕ_e is the electrolyte potential, U is the equilibrium potential, T is the absolute temperature, n is the number of electrons involved in the electrode reaction, F is the Faraday constant and R is the universal gas constant. α is the symmetry factor that is dimensionless and presents a ratio between oxidation and reduction. η_{SEI} is the additional overpotential caused by the Solid Electrolyte Interphase (SEI) layer, which only exist at negative electrode.

As described in previous chapter, the equilibrium potentials are different between materials and are function of stoichiometry number of the electrode. In addition, the equilibrium potentials are also affected by Li ion concentration in electrolyte according Nernst equation

$$
U_{equ} = U_{equ}^{\Theta} + \frac{RT}{zF}\log\left(\frac{c_e}{c_{e0}}\right) \tag{3-2}
$$

where U_{equ}^{Θ} is the equilibrium potential when standard lithium ion concentration in electrolyte

(c_{e0}=1mol·L^{-1}). And U_{equ} is the corrected equilibrium potential when the lithium ion

concentration in electrolyte is non-standard c_e.

The exchange current density, i_0, is the intrinsic rates of electrons and ions transfer at the

interface between electrolyte and electrodes. It can be expressed with concentrations and

symmetric factors, α_a and α_c, that describe bi-directions of one reversible semi-reaction.

$$i_0 = k(c_{s,\max} - c_s)^{\alpha_a} c_s^{\alpha_c} c_e^{\alpha_c} \tag{3-3}$$

where c_s and c_e refer to the lithium ion concentration in solid and electrolyte and $c_{s,\max}$, is the

theoretical maximum ion concentration in solid. α_a and α_c is the oxidation and reduction

symmetry factor.

3.1.2 Charge conservations

To fully understand the electrochemical dynamics of a lithium ion battery, it important to

examine the physical processes that cause the reactions to occur. First, current flowing through

the electrolyte phase of the positive electrode is driven by electric potential and the varying

concentrations near the electrode-electrolyte interface. Movement of ions and flow of electrons

are vital processes in battery performance, and the conductivity of the active materials

determines the rate of that flow. Quantifying the ionic electrolyte conductivity, as with the

diffusion coefficient, requires calculations as a function of electrolyte concentration [24].

$$\kappa = 2.37c_e \exp(-8983c_e^{1.4}) \tag{3-4}$$
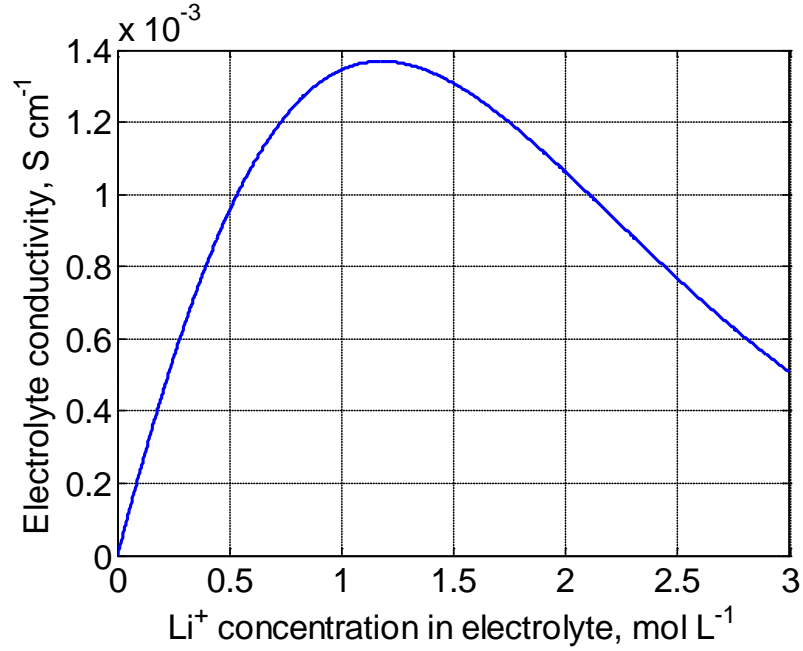
Figure 3-3 Electrolyte conductivity as a function of concentration

The ionic conductivity achieves maximum value when Lithium ion concentration is 1.2 mol·L^{-1}, which is because more ions can carry more charge in order to conduct electricity at low concentration. But they tend to interact with each other and convert to electro-neutral coordination compound at high concentration. The optimal concentration may change with different solute, electrolyte solvent or additives.

The charges produced in oxidation processes should be the same as those consumed in the reduction process. This relationship is described using Ohm's law, expressed as a function of current and potential gradients. Ion transport in the electrolyte is governed by the Nernst-Planck equation, where migration and diffusion terms are considered, as shown in the following equation.

$$\frac{\partial}{\partial l}(\kappa_e^{eff} \cdot \frac{\partial}{\partial l}\phi_e) + \frac{\partial}{\partial l}(\kappa_{D,e}^{eff} \cdot \frac{\partial}{\partial l}(\ln c_e)) + j^{Li} = 0 \tag{3-5}$$

where j^{Li} is the current density in the electrolyte or solid phase, ϕ_e is the electrolyte potential, c_e is the concentration of the electrolyte, κ^{eff} is the effective electrolyte conductivity, while κ_D^{eff} is the concentration driven diffusion conductivity.

As for charge transport in solid, no diffusion term is necessary for electron transport in solid because it is solely governed by Ohm's law.

$$\frac{\partial}{\partial l}(\sigma^{eff} \cdot \frac{\partial}{\partial l}\phi_s) = j^{Li} \tag{3-6}$$

where σ^{eff} is the solid phase electronic conductivity.

3.1.3 Material balance

Charges produced or consumed by chemical reactions taking place in the electrodes are conserved. The chemical process in the entire cell can be described using a material balance principle. Hence, the balance of materials in electrolyte is affected by the gradient of ion concentrations. Since the electrode pores are filled with electrolyte, the balance should consider the porosity of the material. Therefore, the diffusion coefficient is redefined by considering the porosity as follows:

$$D_e^{eff} = D_e \cdot \varepsilon_e^p \tag{3-7}$$

where the diffusion coefficient, D_e, is constant. The material balance equation for the electrolyte considering the porosity is as follows:

$$\frac{\partial(\varepsilon_e c_e)}{\partial t} = \frac{\partial}{\partial l}(D_e^{eff} \cdot \frac{\partial}{\partial l}c_e) + \frac{1-t_+^0}{F}j^{Li} \tag{3-8}$$

where c_e is the concentration of lithium ion in electrolyte, F is the Faraday's constant, t_+^0 is the initial transference number, ε_e is the porosity, and j^{Li} is the current density [26].

For electrodes,

$$\frac{\partial c_s}{\partial t} = \frac{D_s}{r^2} \frac{\partial}{\partial r}\left(r^2 \frac{\partial c_s}{\partial r} \right)$$ (3-9)

where c_s is the lithium ion concentration in electrode and r is the radius of an electrode particle.

When reaction rates change, the current density varies accordingly. Consequently, the concentration is changed.

The reaction rate, j^{Li}, determined by the Butler-Volmer equation is the most important variable that affects not only the charge conservation equations but also the mass transport equation.

3.1.4   Double layer and concentrated ion transport

The double layer is based on the theory of electro-capillarity that a polarized electrode may adsorb a mono-layer of anion onto the surface by covalent force, as a sequence, another thin layer of cation will diffuse near to the adsorption layer by electrostatic force. This theory is invented to explain the extra surface tension in a mercury dropping experiment. [27]
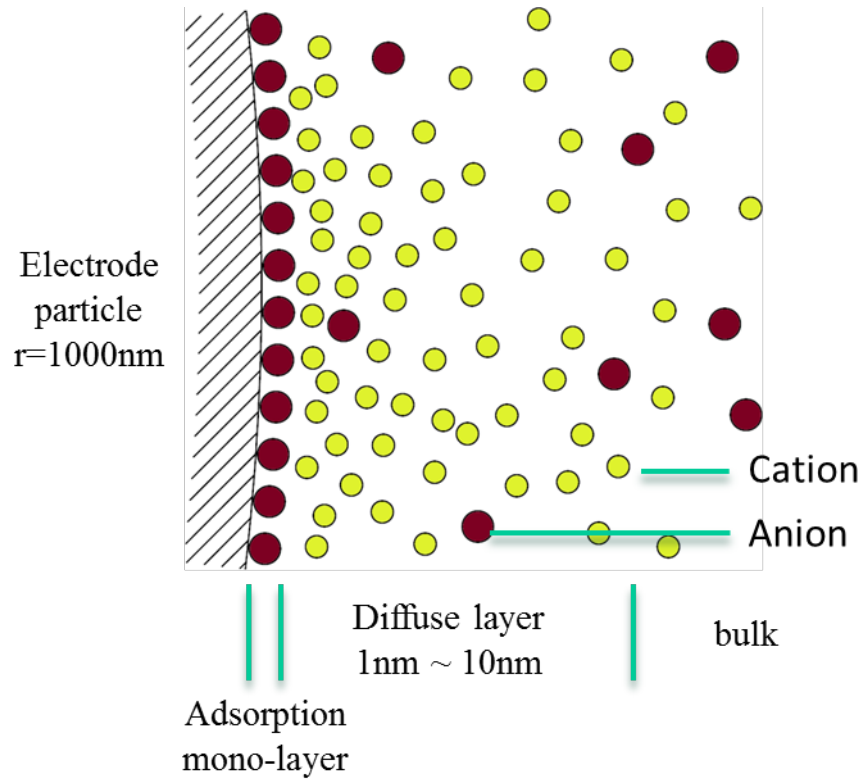
Figure 3-4 Structure of double layer

Due to the large ion concentration, dilute ion transport equation fails to calculate the behavior of ions near electrode surface. The concentrated ion transport consider the chemical potential difference as motivation of ion transport, and the interaction between the specific ion with the solvent as the drag force while ignore the interaction between ions. [28]

$$\frac{\partial c_{\pm}}{\partial t} = \nabla \cdot (b_{\pm} c_{\pm} \nabla \mu_{\pm}) \qquad (3\text{-}10)$$

where c is concentration, b is mobility, and μ is chemical potential that calculated as follows

$$\mu_{\pm} = \frac{\partial F}{\partial c_{\pm}} = \frac{\partial (U - TS)}{\partial c_{\pm}} \qquad (3\text{-}11)$$

where F is free energy, U is internal energy, T is temperature and S is the entropy

The internal energy of the electrolyte is the energy of electrical field itself and the energy of ions inside it shown in equation (3-12). When calculate the concentrated entropic contribution, since it is concentrated solution, Borukhov considered the entropy of three species: anions, cations and free space. [29]

$$U = \int dr(-\frac{\varepsilon}{2}|\nabla\phi|^2 + zec_+\phi - zec_-\phi) \tag{3-12}$$

$$-TS = \frac{kT}{a^3}\int dr(c_+a^3 \ln(c_+a^3) + c_-a^3 \ln(c_-a^3) \\ + (1 - c_+a^3 - c_-a^3)\ln(1 - c_+a^3 - c_-a^3)) \tag{3-13}$$

In equation (3-13), a is assumed to be the length of a single ion, averaged from the crystal volume and molecular number.

3.1.5 Energy conservation

Temperature in operating cells affects the performance and degradation of materials, which is described using the energy equation:

$$\rho C_p \frac{\partial T}{\partial t} = \frac{\partial}{\partial x}\left(k_X \frac{\partial T}{\partial x}\right) + \frac{\partial}{\partial y}\left(k_Y \frac{\partial T}{\partial y}\right) + \frac{\partial}{\partial l}\left(k_l \frac{\partial T}{\partial l}\right) + Q + Q_{convec.} \tag{3-14}$$

where ρ, C_p, k and Q are the density, heat capacity, thermal conductivity, and heat-generation rate per unit volume, respectively.

The heat source term below in equation (3-15), Q, is generally used to calculate the temperature [30].

$$Q = I(U_{OCV} - V_t - T \cdot \frac{\partial U_{OCV}}{\partial T}) \qquad (3\text{-}15)$$

The equation indicates that no heat will be generated when the current goes zero. In reality, heat is continuously generated by the currents that are caused by the non-uniformity of electrochemical energy state gradients, which is called the heat of mixing. Therefore, the heat source term, Q, is divided into three terms, a reversible heat in microcell (q_{rev}), an irreversible heat in microcell (q_{irr}), and the Joule heating caused by the current collectors (q_{cc}) in a single cell per unit volume.

$$Q = \int_V q_{rev} dV + \int_V q_{irr.} dV + \int_V q_{cc.} dV \qquad (3\text{-}16)$$

The reversible heat is a result of the change of entropy during a chemical reaction (TΔS). The rate of the heat generated per volume can be expressed as follows:

$$q_{rev} = j^{Li} \cdot T \cdot \frac{\partial E}{\partial T} \qquad (3\text{-}17)$$

For calculation of irreversible heat generation, a following modification is suggested. When a battery is charged, electric energy supplied to the cell at the terminal is equal to a sum of electrochemical energy stored in the battery and irreversible heat dissipated. When discharged, the electric energy obtained at the terminal is the difference between the electrochemical energy and the irreversible heat. When the charging current is very low, it can be assumed that the energy dissipated is negligible. Then, the electrochemical energy can be expressed as follows:

$$E_{chem}(SOC) = Q_{max} \int_{SOC_0}^{SOC} U_{OCV} \cdot dSOC = Q_{max} \int_{SOC_0}^{SOC} (U_+^{equ} - U_-^{equ}) \cdot dSOC \qquad (3\text{-}18)$$

Since there are always gradients of lithium ion concentrations, equilibrium potentials and current density, total amount of the electrochemical energy can be obtained by integrating the energy in a small control volume. On the other hand, change of SOC is proportional to change of concentration in a volume, so the SOC in the equation above can be substituted by C_s as follows:

$$E_{chemical} = -\varepsilon_{s+} \cdot F \cdot \int_V C_{s+} \cdot U_+^{equ} \cdot dV - \varepsilon_{s-} \cdot F \cdot \int_V C_{s-} \cdot U_-^{equ} \cdot dV \tag{3-19}$$

where ε_s is the active material volume fraction, F is the faraday's constant, c_s is the solid phase lithium ion concentration and U_{equ} is the equilibrium potential.
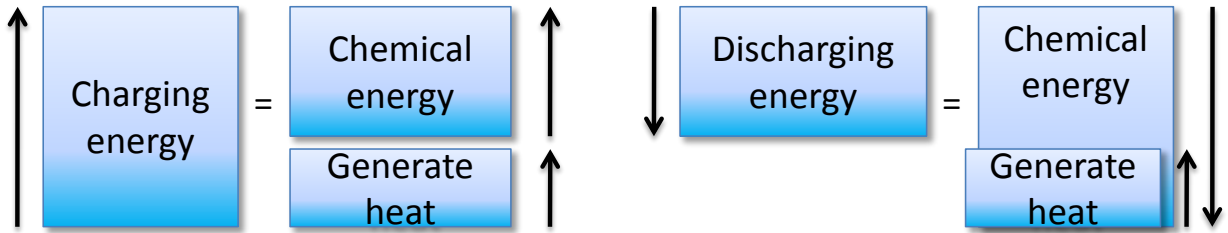
Figure 3-5 Electrical energy, chemical energy and heat

The irreversible heat generation rate for a micro cell is the difference between the electrical power supplied to the cell ($-V_{micro} \cdot I_{micro}$) and the power ($P_{chem.}$) contributing to the chemical energy increase that is obtained by differentiating the electrochemical energy with respect to the time. . When charging, $0 < P_{chem.} < -V_{micro} \cdot I_{micro}$ and when discharging, $P_{cheml} < -V_{micro} \cdot I_{micro} < 0$, so that q_{irr} always becomes positive.

$$q_{irr} = -V_{micro} \cdot I_{micro} - P_{chemical} \tag{3-20}$$

The heat generation rate caused by the Joule heating in the current collectors is as follows:

$$q_{cc} = \sigma \cdot (\nabla \phi_{cc})^2 \tag{3-21}$$

In addition, the heat transfer by convection is considered.

$$Q_{convec.} = h_C \cdot (T_S - T_\infty) \tag{3-22}$$

where h, T_S, and T_∞ denote the convective heat transfer coefficient, the surface temperature, and ambient temperature, respectively.

3.1.6   Model simplifications

Terminal voltage of a micro cell is given as a difference between electrode potentials and equilibrium potential. The electrode potentials are a function of concentration given by the Nernst equation. The equilibrium potential of a cell is called open circuit voltage (OCV) when no current flows. The OCV is the difference between the two standard potentials of the positive and negative electrode and is measured experimentally. Separation of individual equilibrium potentials for positive and negative electrodes from the measured OCV are carried out using an empirical equation for the equilibrium potential in negative electrode given in [24].

$$\begin{aligned}U_-(x) &= 8.00229 + 5.0647x - 12.578x^{1/2} - 8.6322e - 4x^{-1} + 2.1765e - 5x^{3/2} \\ &- 0.46016\exp(15(0.06 - x)) - 0.55364\exp(-2.4326(x - 0.92))\end{aligned} \tag{3-23}$$

Currents produced during chemical reactions are a function of overpotentials governed by the Butler-Volmer equation that consists of two exponential functions. In fact, the overpotentials usually vary within a linear range under normal battery operating conditions, Therefore, the exponential function can be linearized by Taylor expansion as shown in equation (3-24), which

definitely works at low current. However, this simplification may cause some error at a large enough current whose magnitude depends on both the load current and exchange current density.

$$j_N^{Li} = a_{S,N} \cdot i_{0,N} \frac{n \cdot F}{R \cdot T} (\eta_N - \eta_{SEI}) + O(\eta_N^3)$$
$$j_P^{Li} = a_{S,P} \cdot i_{0,P} \frac{n \cdot F}{R \cdot T} \eta_P + O(\eta_P^3)$$

(3-24)

Take the constants into equation and we can get a rough estimation of error caused by linearization. Actually, there is almost no way we can directly measure the activation overpotential because it is indistinguishable overlapped with concentration overpotential and ohmic overpotential, but the current is easy to know.
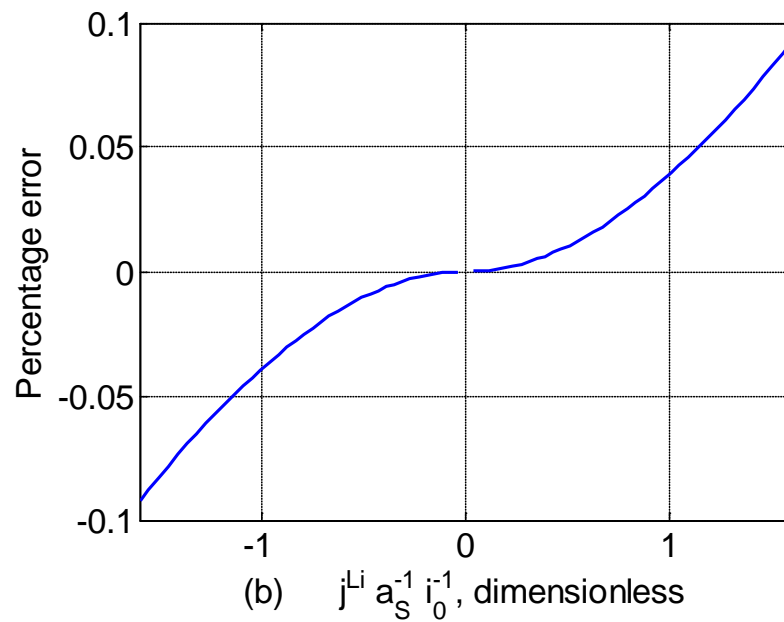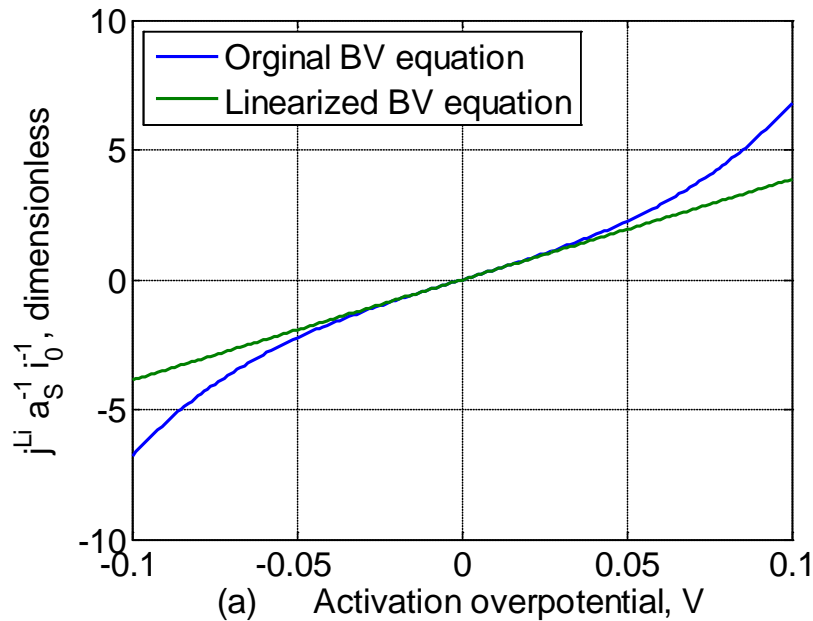
Figure 3-6 Error caused by linearization

The specific area a_s in our battery is about 1.5e4 $cm^2 \cdot cm^{-3}$, and the volume for each of electrode is about *15*20*2*0.5=300cm³*. So there is about 4.5e6 cm^2 particle surface for each electrode. Different researchers use different values of exchange current density listed in Table 3-

1. If we just take the average value, $i_{0-} = 1.136\ mA \cdot cm^{-2}$ and $i_{0+}=0.842\ mA \cdot cm^{-2}$. When apply $I=100A$ current to the battery, current density $j^{Li} \cdot a_s^{-1} \cdot i_0^{-1} \approx 0.02 << 1.2$, which indicates the error is much less than 5%. So the linearized Butler-Volmer equation is precise enough, there is no need for high order expression. Particularly, the use of this linear equation in the charge conservation equation eases convergences of all calculations and reduces computational time.

Table 3-1 exchange current density used by different researcher

i_0 (mA·cm^{-2}) for Li$_x$C$_6$		i_0 (mA·cm^{-2}) for Li$_y$Mn$_2$O$_4$ based compound	
0.041	[2]	0.289	[2]
		1.26	[5] [11]
0.215	[12]	0.489	[12]
3.6	[13]	2.6	[13]
0.688	[25]	0.416	[25]

As matter of fact, the time constant of ion concentration is larger than that that for electrons, it is assumed that the second term in the conservation of charge equation (3-5) is regarded as constant. Therefore, concentration and temperature at a given time can be used to calculate κ^{eff} and κ_D^{eff}. Hence, the only unknown variables are the phase potentials, so that the equations are linearized and the number of equations to be solved simultaneously is reduced.

3.2 Numerical calculation

3.2.1 Initial and boundary conditions

Numerical calculation requires initial and boundary conditions to initiate and finalize simulations. The three variables calculated from dynamic equations are lithium ion concentration in solid and electrolyte, and cell temperature, while others are obtained from static equations using these three variables.

The boundary condition for the potential of an electrode is:

$$-\sigma_-^{eff} \left. \frac{\partial \phi_s}{\partial l} \right|_{l=0} = -\sigma_+^{eff} \left. \frac{\partial \phi_s}{\partial l} \right|_{l=L} = \frac{I}{A}$$

$$\left. \frac{\partial \phi_s}{\partial l} \right|_{l=\delta_-} = \left. \frac{\partial \phi_s}{\partial l} \right|_{l=\delta_+} = 0$$

(3-25)

where the σ^{eff} is the conductivity, ϕ_s is the solid phase potential, $l=0$, L represents the interface between the electrode and current collector at negative and positive sides, respectively, and $l=\delta_-$, δ_+ represents the interface between the separator and electrode at negative and positive sides, respectively. For a given current density, the potentials outside of the electrolyte boundary are zero as follows:

$$\left. \frac{\partial \phi_e}{\partial l} \right|_{l=0} = \left. \frac{\partial \phi_e}{\partial l} \right|_{l=L} = 0$$

(3-26)

The initial conditions of various variables are determined from the initial lithium ion concentration in the electrodes. The concentration is expressed as a function of SOC, as follows:

$$c_{s-} = (stoi_0^- + (stoi_{100}^- - stoi_0^-) \times SOC) \cdot c_{s-,max}$$

(3-27)

$$c_{s+} = (stoi_0^+ + (stoi_{100}^+ - stoi_0^+) \times SOC) \cdot c_{s+,max}$$

The concentration of lithium ions inside the particles is spherically symmetric with no generation within, so the gradient of lithium ion concentration at the inner boundary is zero. The outer boundary of electrode particles is determined by the rate of the reaction taking place.

$$r^2 \frac{\partial c_s}{\partial r}\bigg|_{r=0} = 0$$

$$-D_s \frac{\partial c_s}{\partial r}\bigg|_{r=R_s} = \frac{j^{Li}}{a_s F}$$

(3-28)

Since there is no electrolyte flow prior to current flow through the battery, the change in electrolyte concentration at the boundaries is shown below to equal zero.

$$\frac{\partial c_e}{\partial l}\bigg|_{l=0} = \frac{\partial c_e}{\partial l}\bigg|_{l=L} = 0$$

(3-29)

The initial cell temperature is set to an ambient temperature. At a low current, heat transfer between the environment and the cell is regarded as negligible. At the boundary,

$$-k \frac{\partial T}{\partial l} = h \cdot (T - T_a)$$

(3-30)

where k is the thermal conductivity of the outer casing, h is the overall convective heat transfer coefficient, T_a is the ambient temperature, and T is the temperature in the cell.

3.2.2 Numerical method for micro cell

The micro cell is discretized into 25 grids through the plane. The negative and positive electrodes are meshed with 11 and 8 grids, respectively, because of different thickness of the electrodes. As a result, 44 discrete equations are obtained for the equations (3-5) and (3-6) in order to calculate potentials. As potentials and concentrations near both interfaces between electrode areas and separator change drastically, the size of grids at the interfaces should be small enough to minimize the numerical errors. In addition, the small grid is generated at the outer boundary of spheres.

All of equations are converted into discrete forms, coded using MATLAB and solved for the solid phase potentials at the electrodes and the electrolyte phase potential across the cell. For calculations, a finite differential method with an implicit scheme is employed to get converged fast.

The resulting phase and equilibrium potentials are used to calculate overpotential at each section across the cell, which allows for calculation the reaction rate, j^{Li}, using the Butler-Volmer equation. The reaction rate will be inputted to mass balance equations (3-8) and (3-9) to determine the change in concentration at each time step. Similar to the method used for the calculation of the reaction rate, an equation for each segment or grid of the battery cell is derived. While the initial values are known, the lithium ion concentration as a function of the change in time provides the variables for the equation.

In fact, electric field in both of electrodes and electrolyte responses faster than that of ion transports when charged and discharged. Therefore, it is assumed that the potentials, ϕ_s and ϕ_e are constant during each time step and calculated just in one subroutine. Conversely, ion transport is

dynamically calculated in another subroutine using the mass balance equations for ion concentrations c_s and c_e. The discretized equations can be numerically solved by implicit or explicit method. The major drawback of the implicit method is the difficulty in coding in compared with the explicit one that is less accurate and stable. The code developed is based on the implicit method. The dynamic equation above has a general form $\dfrac{dc}{dt} = f(c, \phi)$, where

$c = \begin{pmatrix} c_e \\ c_s \end{pmatrix}$ and $\phi = \begin{pmatrix} \phi_e \\ \phi_s \end{pmatrix}$. The potential can be solved from the static equations (3-5) , (3-6). Even though both explicit and implicit method assume that the function, f, during two time steps is constant, the explicit method explicitly calculates the function using c and ϕ from the previous time step, while the implicit method considers c and ϕ to be the values of potentials and concentrations in the following time step and calculate them by solving a matrix about c. For calculation of the potential, ϕ, at the following time step, change of concentration for the time step, Δc, instead of c is calculated at a c_0 at the previous time point, which results in the potential ϕ as follows:

$$\phi = \phi_0 + A \cdot \Delta c_e + B \cdot \Delta c_{s,e} \tag{3-31}$$

where the ϕ_0 is the potential at previous time step, and A and B are coefficient matrices that include the linearized relationship between ϕ and Δc.

3.2.3   Numerical method for two dimensional single cell

Compare to one dimensional mesh in micro cell model, the two dimensional mesh in single cell model has much more grids. In addition, each of the grids is a micro cell and coupled with

the whole system. It will take too long to calculate the matrix if list everything as the vector to be solved. The way to reduce the complexity is to decouple the single cell model and micro cell model by linearizing micro cell model at the operating point that estimated
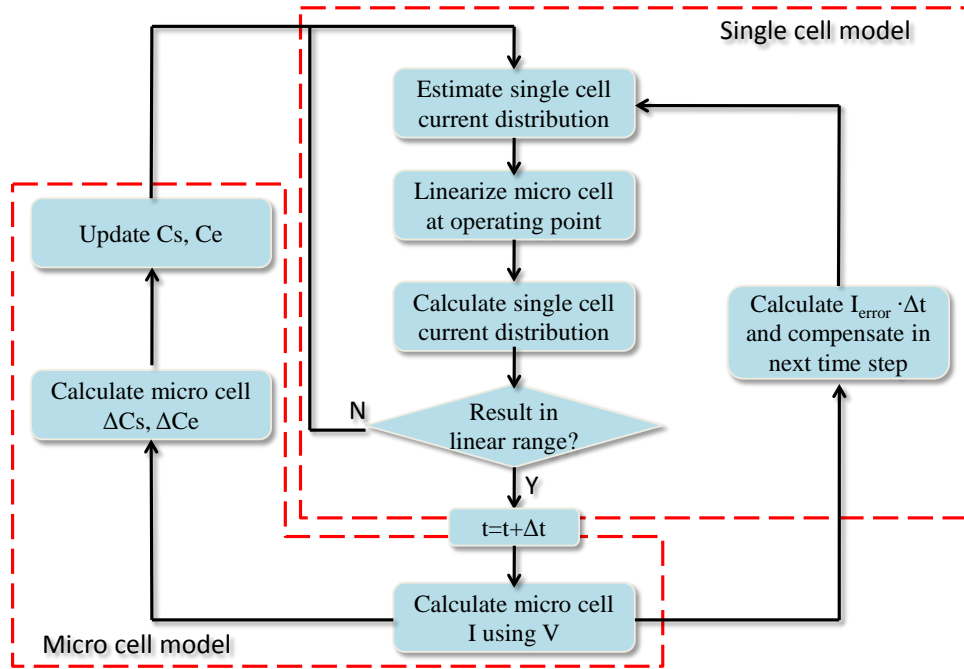

Figure 3-7 Flow chart to solve 2D single cell

Another effort to reduce the calculation time is to sort the thousands of micro cells into syndromes according to the current density of the micro cells because the micro cells with same load condition and initial state must have identical Lithium ion concentration in both electrolyte and electrodes during the whole process. And each syndrome only needs to be calculated once at the step of micro cell linearization or the step of updating concentrations. The I_{error} feed-back is used to reduce the error caused by micro cell linearization. In order to better estimate single cell current distribution and increase the stability of the code, especially when step load is applied to the model, the vector B in the stiff differential equation $A \cdot \phi_{cc} = B$ is split as $B = C + D \cdot I$ as

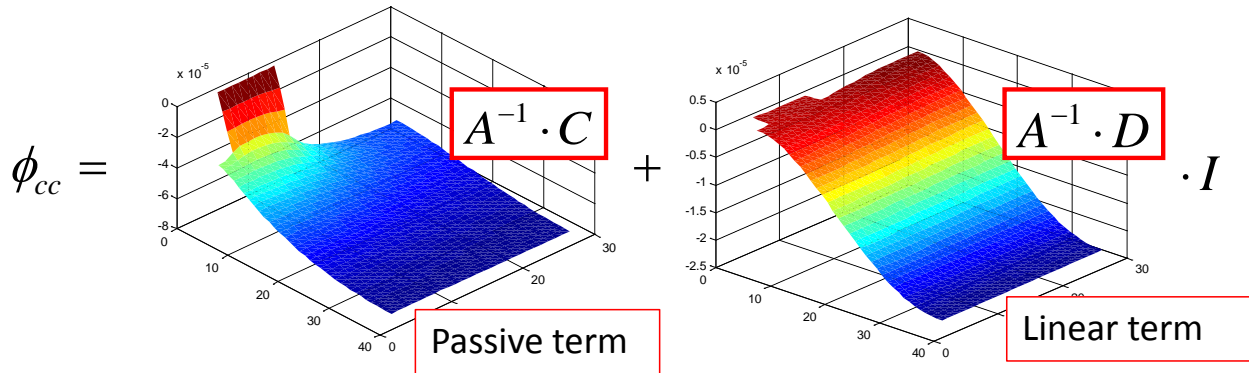shown in Figure 3-8. Where C is load-independent term, D is load-dependent term and I is the load current.

$$\phi_{cc} = \boxed{A^{-1} \cdot C} + \boxed{A^{-1} \cdot D} \cdot I$$

Passive term

Linear term

Figure 3-8 Improved code for estimating linear range in single cell

3.3 Static and dynamic analysis of a micro cell

3.3.1 Potential and overpotential

Standard potentials are determined by the type of chemical compounds used for the electrodes and are a function of the stoichiometric numbers of the chemical compound and SOC. The terminal voltage for a given electrode can be calculated based on the standard potentials. When a battery is charged and discharged, two reversible half reactions occur that cause the potential losses (Overpotentials). The overpotentials of a cell at two different SOCs (50% and 80%) are shown in Figure 3-9 under assumption that the OCV at a specified SOC is constant. The concentration overpotential, $\Delta\phi_e$, is the potential difference in the electrolyte phase caused by the concentration of the reactants. In addition, the ohmic and the concentration overpotential are depedent upon the geometry and tend to increase when the film layers become thicker. Conversely, the activation overpotential was not "cumulative" through the plane of the battery

38

film, so that the value is relatively small. The idea cell voltage in each figure is constant, but varies as a function of SOC.
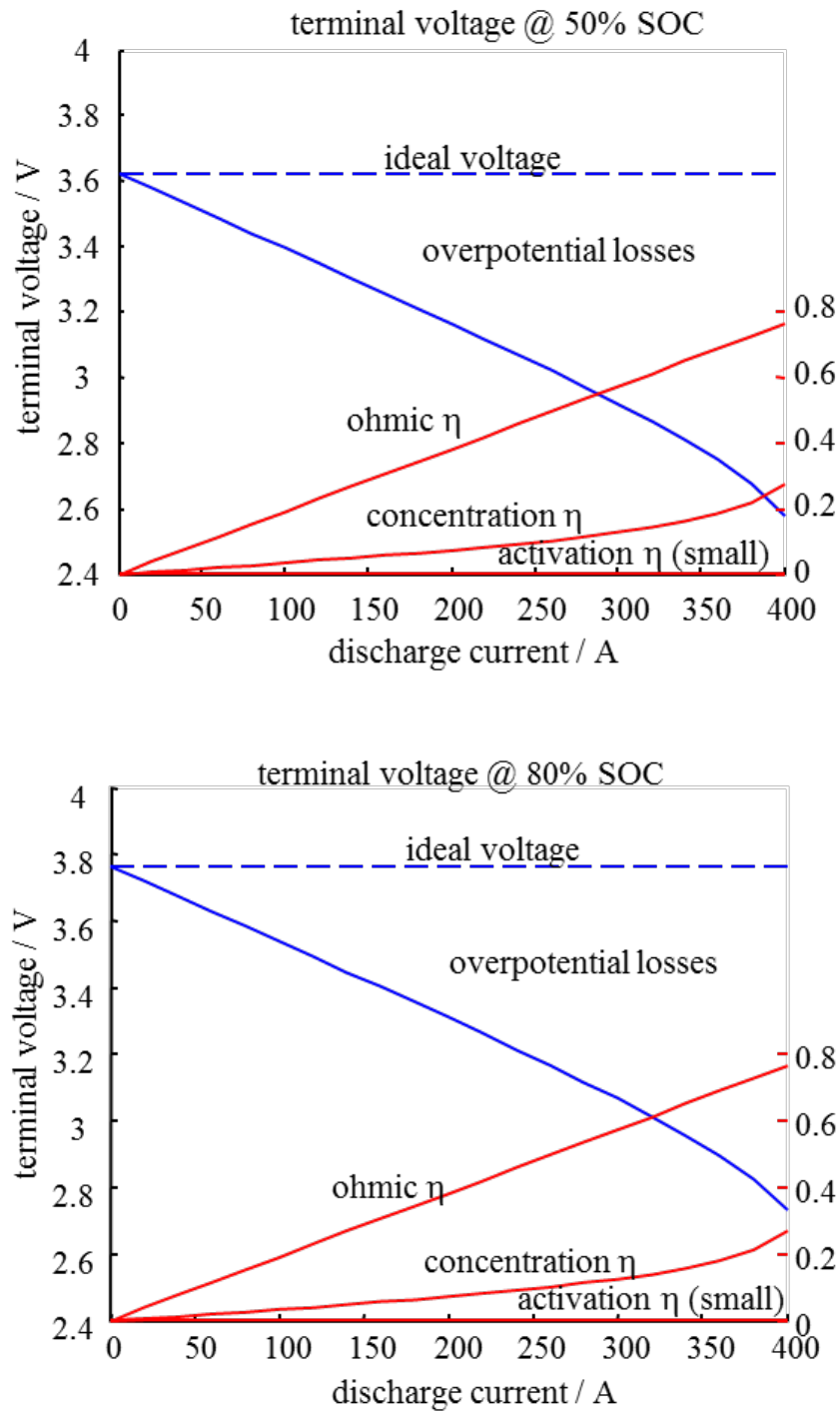

Figure 3-9 Overpotentials of micro cell as a function of discharging current at different SOC

The Figure 3-10 (a) shows the potential of a micro cell, where the l coordinate is a dimensionless number of meshed grids along through-the-plane. The range of the grid for $0<l<0.45$, $0.46<l<0.67$, $0.68<l<1$ corresponds to the anode, the separator, and the cathode, respectively. We assumed that the potential of the electrolyte at $l=0$ is the ground potential, so that the potential of the anode and the cathode is about $0.1V$ and $3.6V$, respectively. The zoomed-in potentials in the anode are shown in Figure 3-10 (b). The difference between the equilibrium potential, U, and the solid potential is relatively small and varies from $l=0$ to $l=L$. In fact, the activation overpotential is the difference between the potential in solid, electrolyte, and equilibrium potentials, as shown in equation (3-23).

Figure 3-10 (c) shows the cathode and corresponding equilibrium potential and overpotential. The overpotential at the cathode always has an opposite sign when compared to the anode, and in each electrode it can be either positive or negative depending on whether the cell is charging or discharging. In this case, the cell is obviously discharging because the overpotential at the anode is positive, which means the current is flowing from the negative electrode to the electrolyte then to the positive electrode. Figure 3-10 (d) shows the corresponding overpotential.
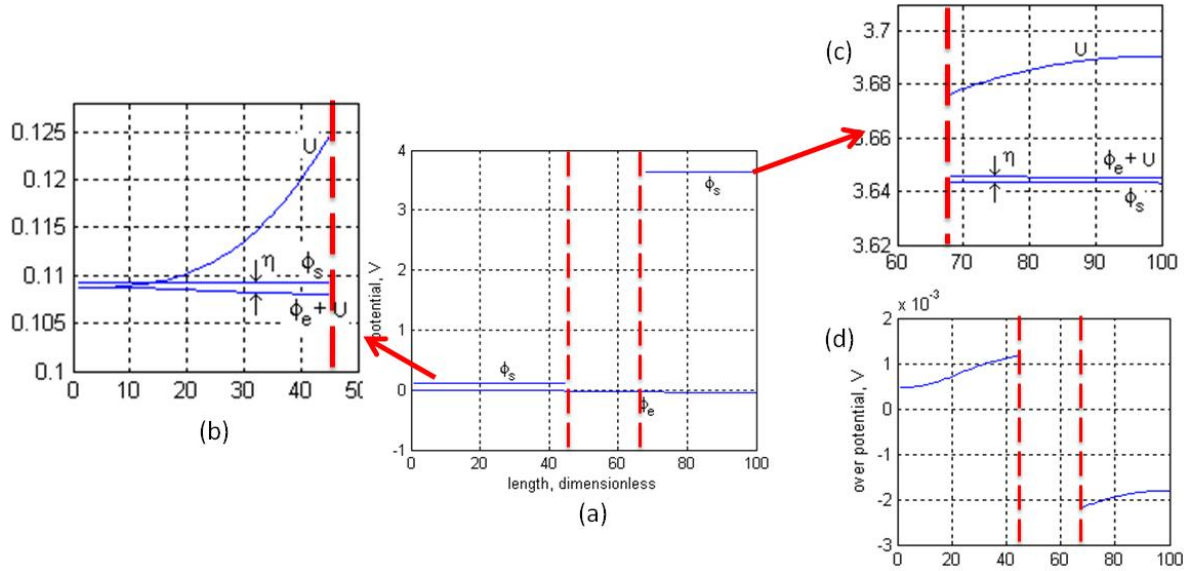
Figure 3-10 potential and overpotential in a micro cell

3.3.2 Current distribution

When a battery is charged or discharged, chemical reactions take place at the interface between the electrodes and electrolyte. As a result, electrons and ions are separated at the cathode. The electrons and ions are transported through an external circuit and the electrolyte, respectively, to anode and combine again there to complete the total reaction. The current in the electrodes is composed of electron current and ion current because of the porosity, while only ion current can go through the separator. The gradient of ion currents is the current density, j^{Li}, whose slope indicates the direction of the current (i.e. positive slope implies that the current flows from solid to electrolyte).
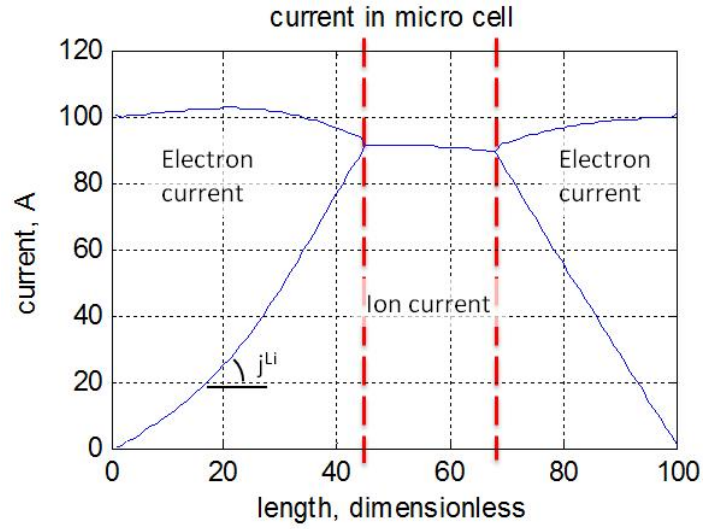
Figure 3-11 current distribution of micro cell

3.3.3　Concentration of lithium ions

Concentration of lithium ions in solids and electrolyte is the key factor that affects physical variables and states of the battery like SOC, conductivities, and exchange current density. Since the concentration in the solid is not uniformly distributed, only the lithium ion concentration in the electrodes at the outer boundary is shown in Figure 3-12, which determines the maximum discharge or charge rate at a moment.
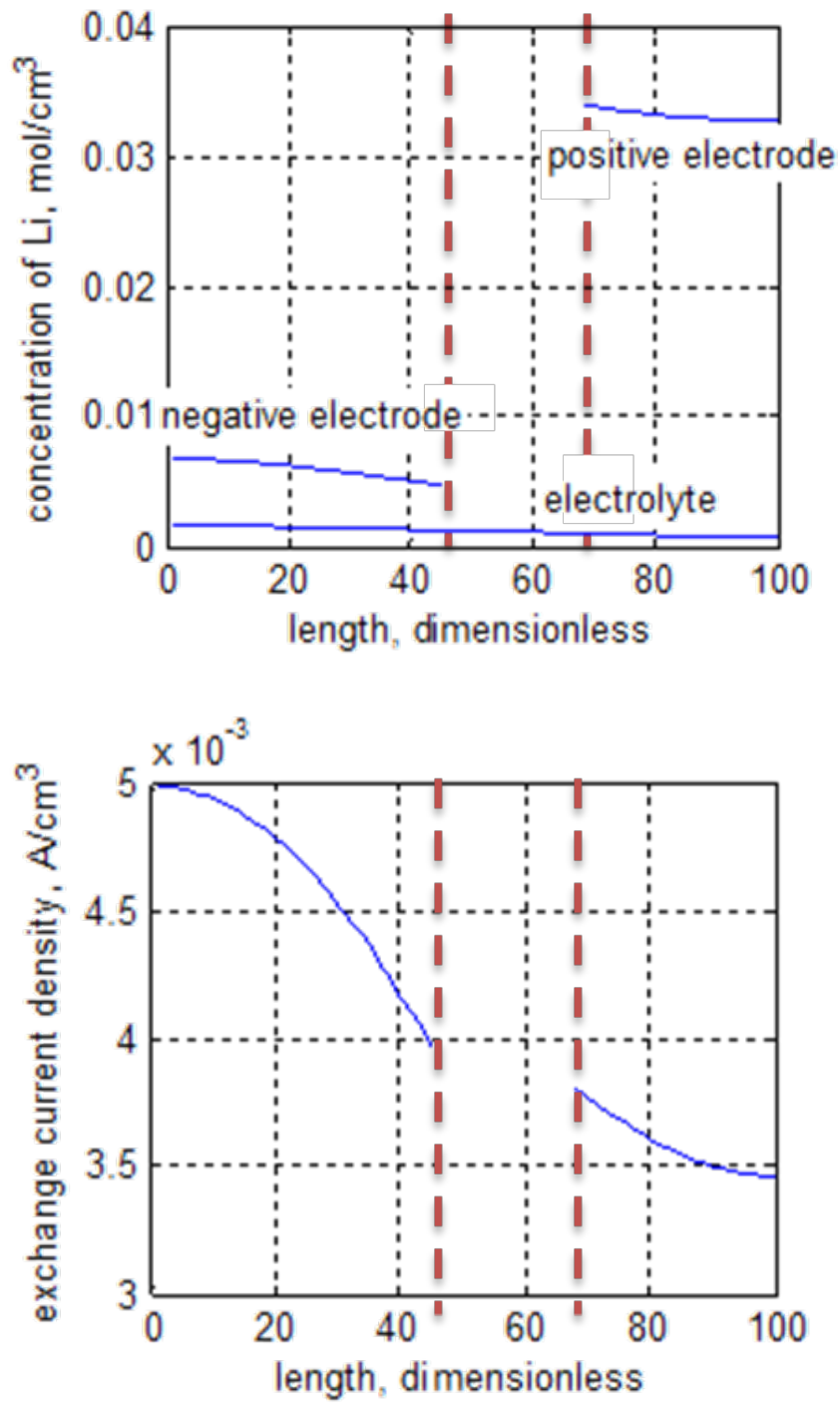
Figure 3-12 lithium ion concentrations and exchange current density in micro cell

Responses of a high discharging current rate (10C rate) on concentration and current density

are shown in Figure 3-13. The current density shows a highest value in the electrode at the point

of contact with the separator. It decays with time because the migration of ions in both the electrolyte and the electrodes mitigates the difference of reaction rates. It takes several minutes for ion concentration to be uniformly distributed.
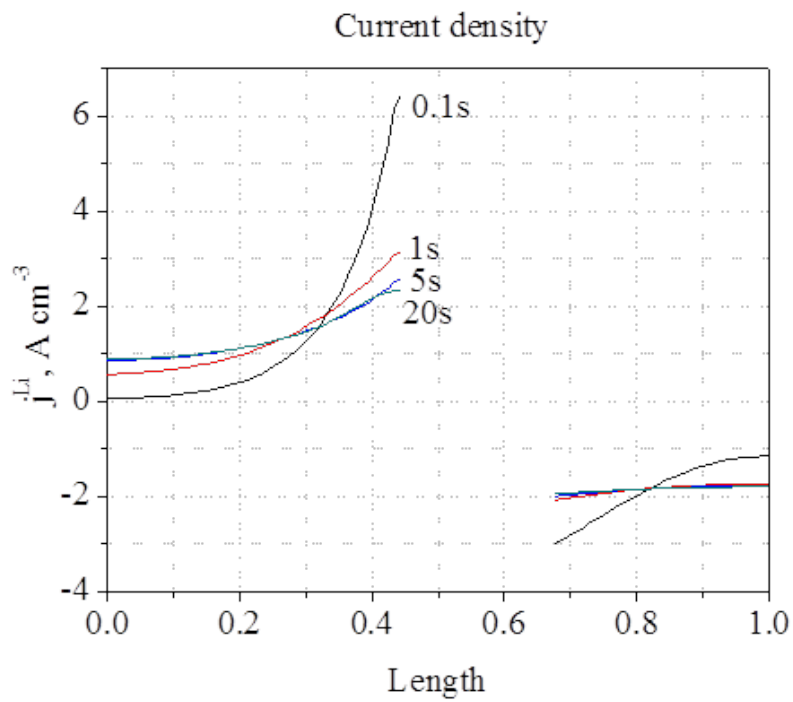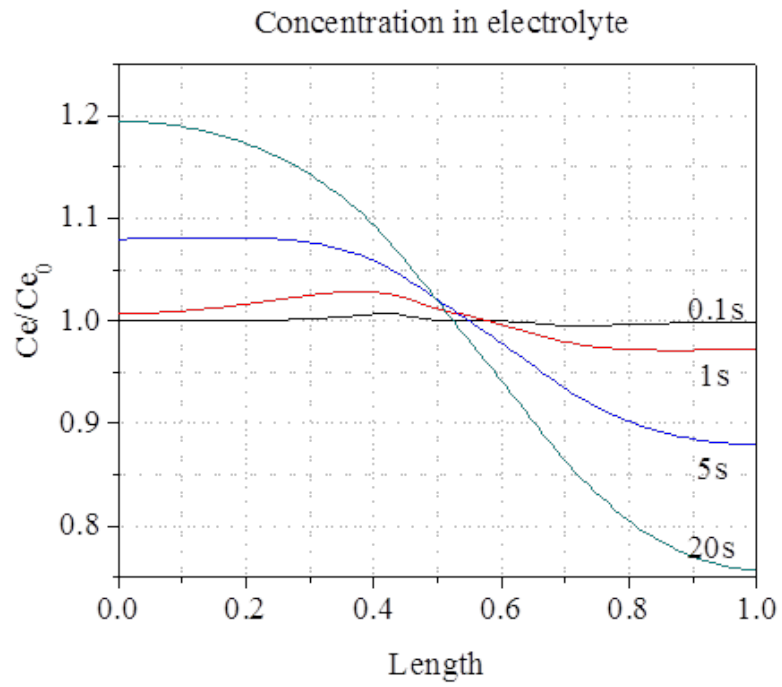
Figure 3-13 Unsteady behaviors of concentration and current at 10C discharging

In Figure 3-14, *r=0* represents the center of the electrode particles, while *r=1* is the outer boundary of the electrode particles. The geometry of electrodes along with material properties like thickness and porosity result in different concentrations, for example at *l=0* and *l=1*. The magnitudes of concentrations at the boundaries of the separators on the negative electrode are different from that on the positive electrode because of the high conductivity.
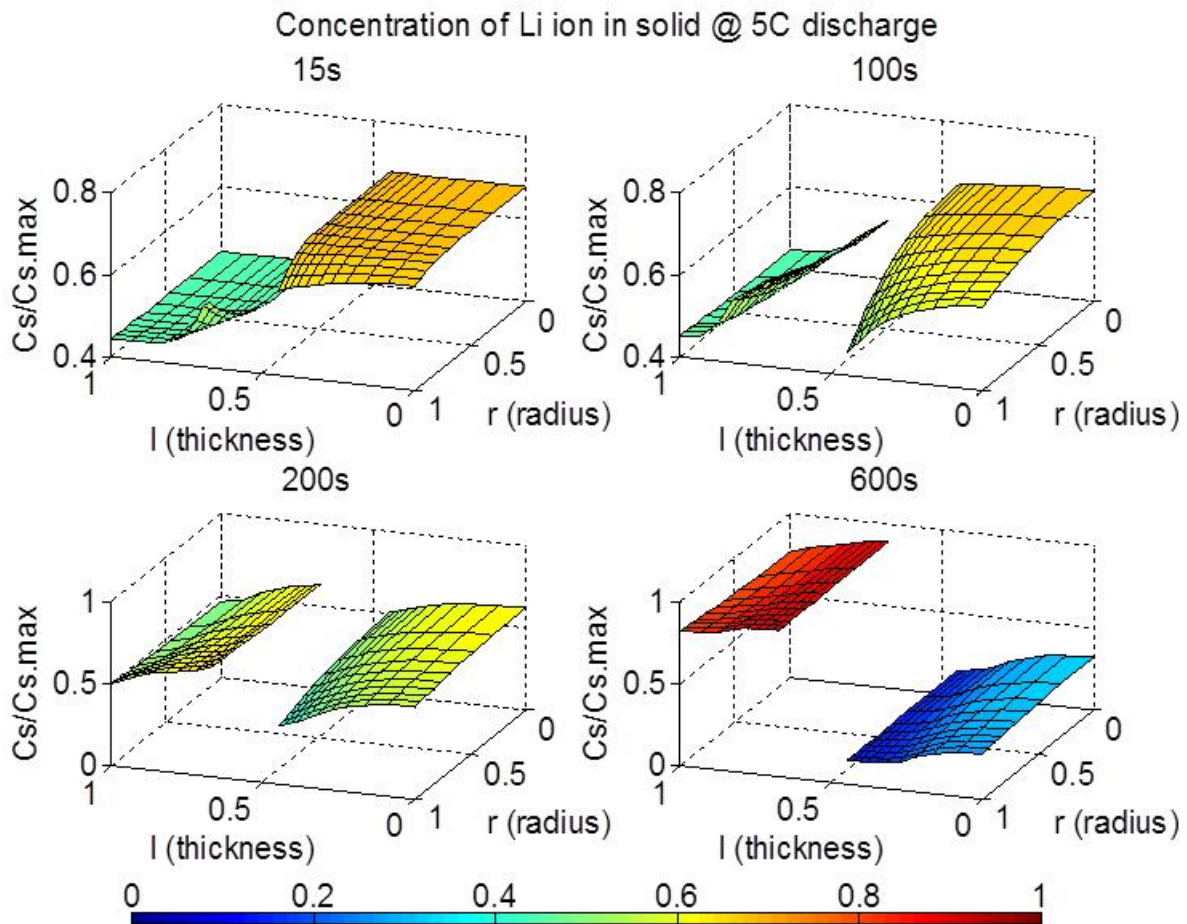
Figure 3-14 Response of ion concentration in electrodes

3.3.4 Constant current (CC) and Constant voltage (CV) mode

Generally, charging a cell is carried out by two modes, a constant current mode (CC mode) and a constant voltage mode (CV mode). Transition from one mode to another is simply implemented by changing the boundary condition of the solid conductive equation (3-6). The boundary conditions for the two modes are as follows:

$$\begin{cases} \sum j^{Li} = 0 \\ \phi_{s+} - \phi_{s-} - R_{cc} \cdot \sum \Delta L \cdot j_{-}^{Li} = V_{micro} \end{cases} \tag{3-32}$$

$$\begin{cases} \sum j^{Li} = 0 \\ \sum j_{-}^{Li} = I_{micro} / \Delta L \end{cases} \tag{3-33}$$

The simulation result of CC+CV charging is shown in Figure 3-15. The current in CV mode decay as an exponential function, the time constant is proportional to the inner resistance of battery
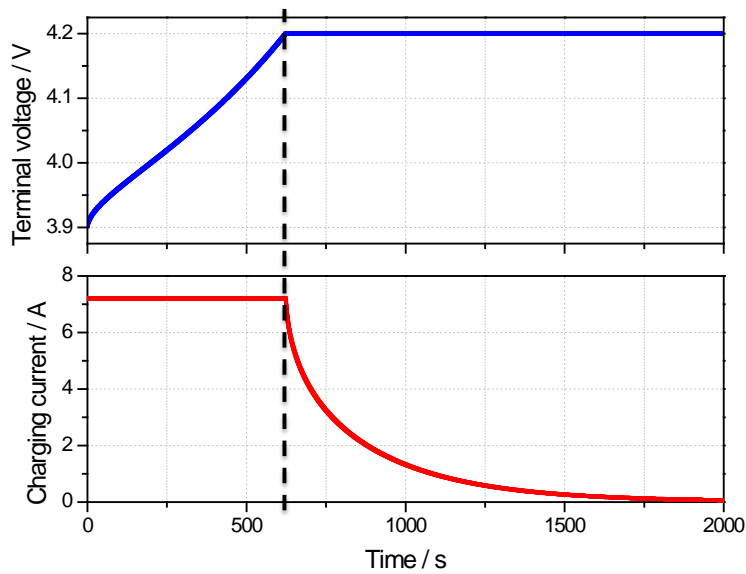
Figure 3-15 CC and CV charging

3.3.5 Numerical error dependency on number of mesh grids and time interval

The number of mesh grids has little effects on the calculation result. We can see the simulated 1C discharging terminal voltage with grids number is 10, 25, and 50 overlap to each other in Figure 3-16 (a). In order to show the numerical error dependency on the number of mesh grids, the standard deviation of 18 sets of simulation with grids number from 4 to 200 is calculated and shown in Figure 3-16 (b). The numerical error is relatively large when the grid number is very small, while the error is small enough without any obvious trend when the grid number is greater than 15.
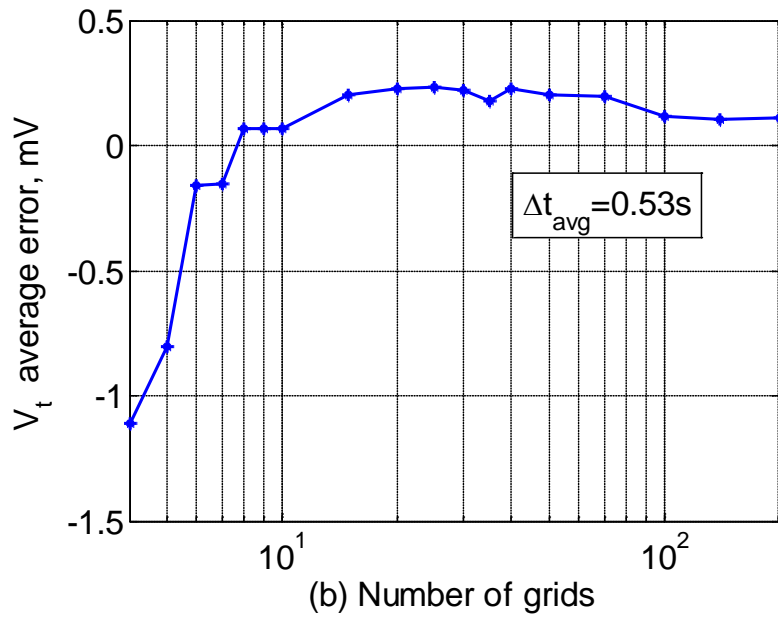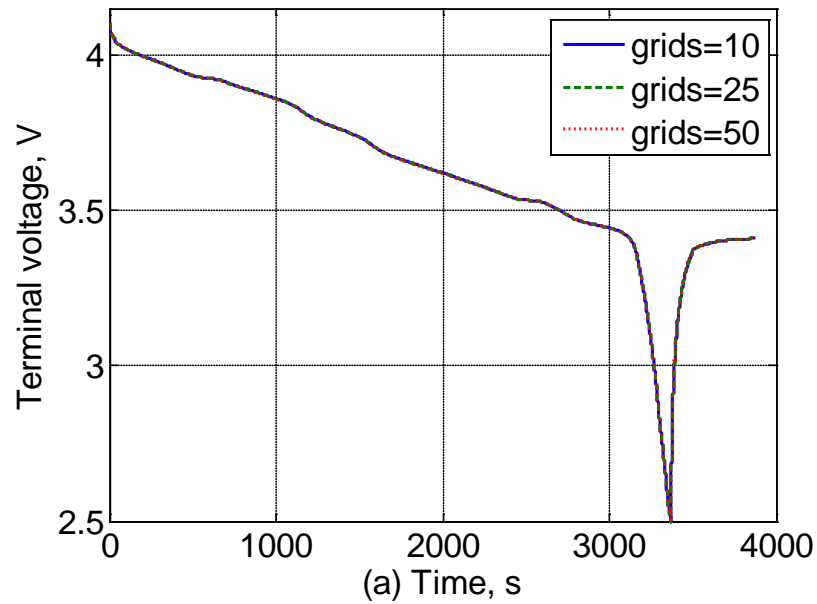
Figure 3-16 Effect of mesh grids

Similar way, the effects of time intervals of calculation steps in the range of 0.04s to 0.6s are

shown in Figure 3-17. Even though the error increases when the time interval is greater than

0.2s, the total error between 0.6s and 0.04s is only 0.35mV which is the same order of experimental error, so it is acceptable.
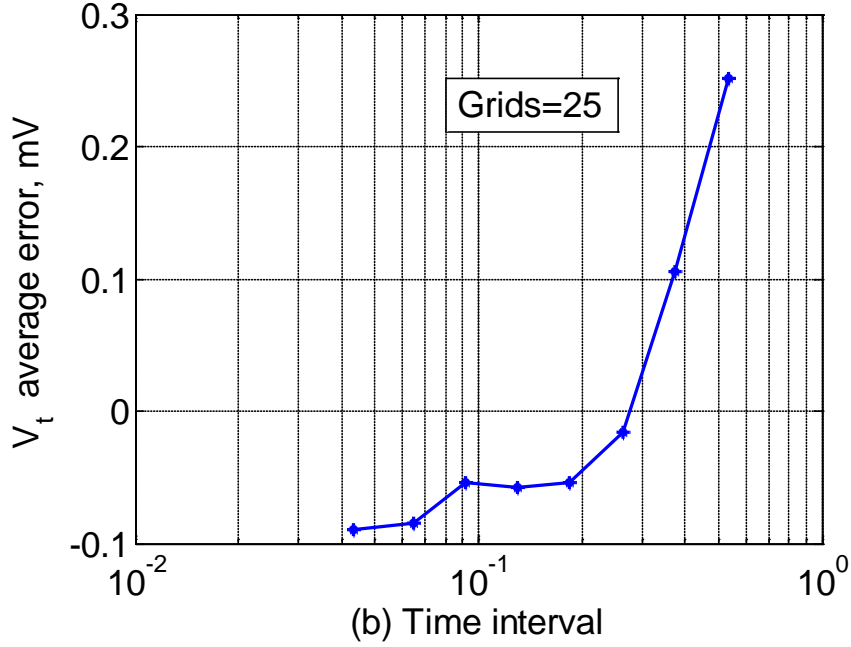
Figure 3-17 Effect of time interval

3.4 Modeling of a pouch type single cell

Micro cells are connected in parallel by the current collectors that provide a current pathway to the terminal tabs. For each of the current collectors, the potential field is described using Ohm's law:

$$
\begin{aligned}
\sigma_{cc-}\left(\frac{\partial^2 \phi_{cc-}}{\partial x^2} + \frac{\partial^2 \phi_{cc-}}{\partial y^2}\right) - \frac{I_{micro}}{l_{cc-}} = 0 \\
\sigma_{cc+}\left(\frac{\partial^2 \phi_{cc+}}{\partial x^2} + \frac{\partial^2 \phi_{cc+}}{\partial y^2}\right) + \frac{I_{micro}}{l_{cc+}} = 0
\end{aligned}
\tag{3-34}
$$

where σ_- and σ_+ are the conductivity of aluminum and copper, respectively, ϕ_{cc-} and ϕ_{cc+} are the potentials on two current collectors, I_{micro} is the current for the micro cells with units of A·cm^{-2}, and l_{cc-} and l_{cc+} are the thickness of the current collectors.

Since the cell is made of identical multiple layers of current collectors, it is assumed that the collectors have the same boundary conditions as the load profile at the terminal tabs. I_{micro} that is given by derivatives of the potential field ϕ_{cc} on both current collectors, as described in Equation (3-34) . On the other hand, the relationship between I_{micro} and the voltage of the corresponding micro cell, $V_{micro} = \phi_{cc+} - \phi_{cc-}$, should satisfy the nonlinear dynamic micro cell equations, so that all of the micro cells can be coupled to each other.

The simulation results reveal that the I_{micro} is asymmetrically distributed because of the different conductivity of the two current collectors, even though the terminal tabs are symmetrically located. Responses are calculated at 1 sec after a 100A discharging current is applied where the initial temperature is 300K and the initial SOC is 50%.

The potential distributions on both current collectors are shown in Figure 3-18 and Figure 3-19. At the positive current collector, the potential near the current tab decreases when the battery is discharging and increases when charging. For each grid, the potential difference between the two current collectors is the potential of micro cell, so the micro cells near the two current tabs show highest overpotential than other locations because of a high reaction rate near the tabs.

Potential on positive current collector
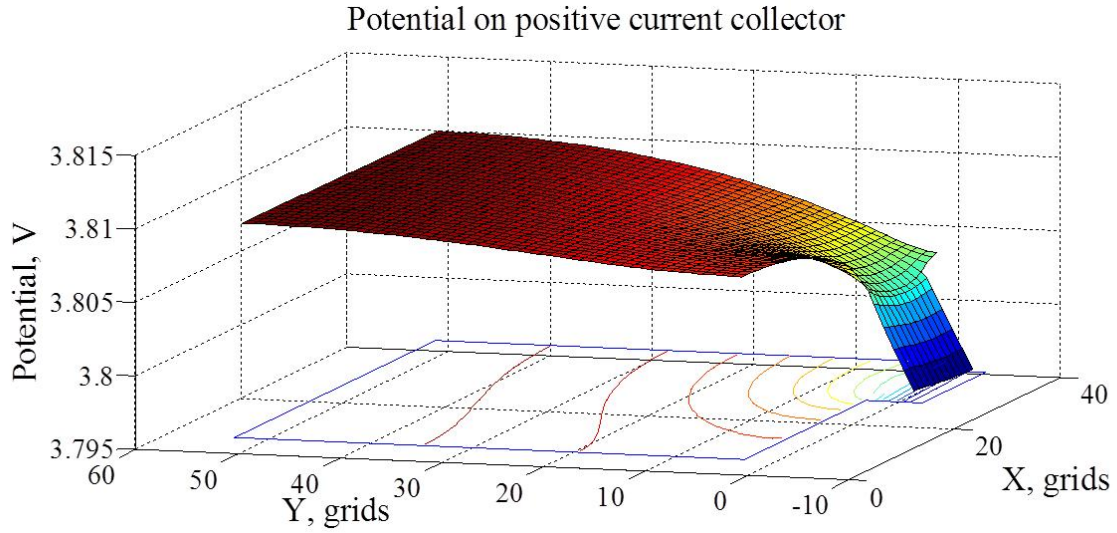
Figure 3-18 Potential distributions on positive current collector when discharged

Potential on negative current collector
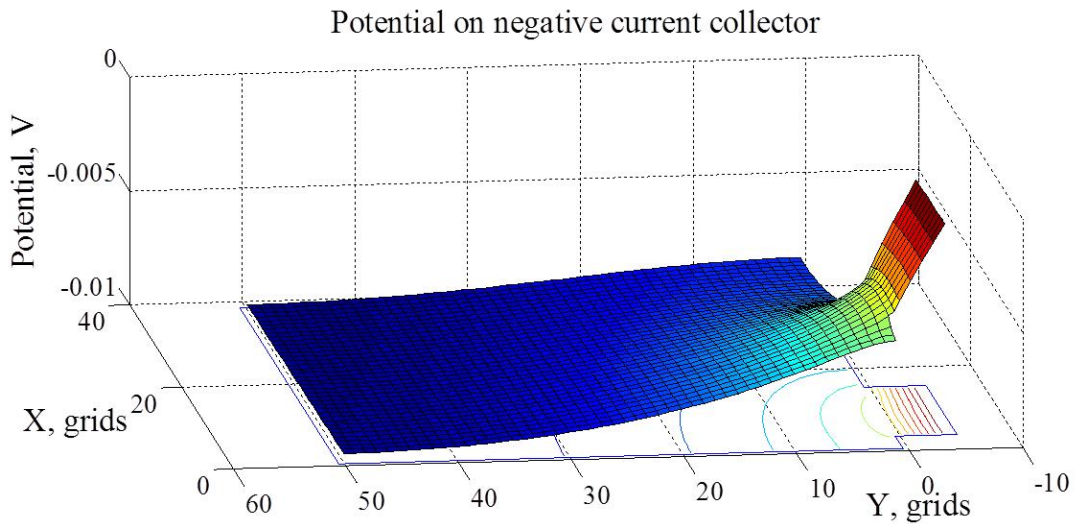
Figure 3-19 Potential distributions on negative current collector when discharged

Due to the non-uniform potential distribution on both current collectors, the voltages of micro cells are not identical and consequently the reaction rates of micro cells are different from each other. The reaction rate of micro cells determined by the current flow through the micro cells per unit area with an *X-Y* cross-section is shown in Figure 3-20. The reaction rate near terminal tab is higher than that in other area at the beginning. As a result, the SOC of the region

is low for a period of time. Since the low SOC leads to a low equilibrium potential, the overpotential decreases if the terminal voltage remains the same as before and consequently the reaction rate get decreased. The results show that the reaction rate near the positive tab is the highest, 20% greater than the lowest grid at the given operating condition.
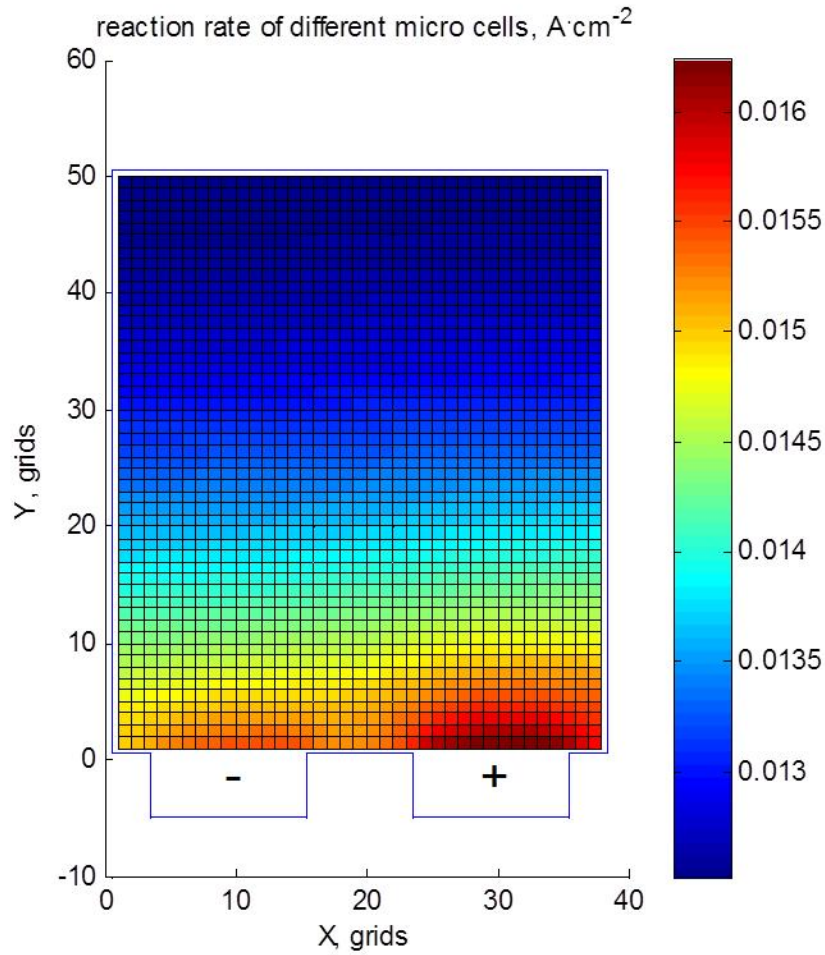
Figure 3-20 Initial reaction rates of different micro cells

3.5 Model validation

In the electrochemical-thermal model, there are some parameters and equations which should be validate by the experiment. The validation should be going in three aspects: CC/CV terminal behavior; CC/CV cell temperature and heat generation; EIS behavior.

3.5.1 Experiment Setup Design
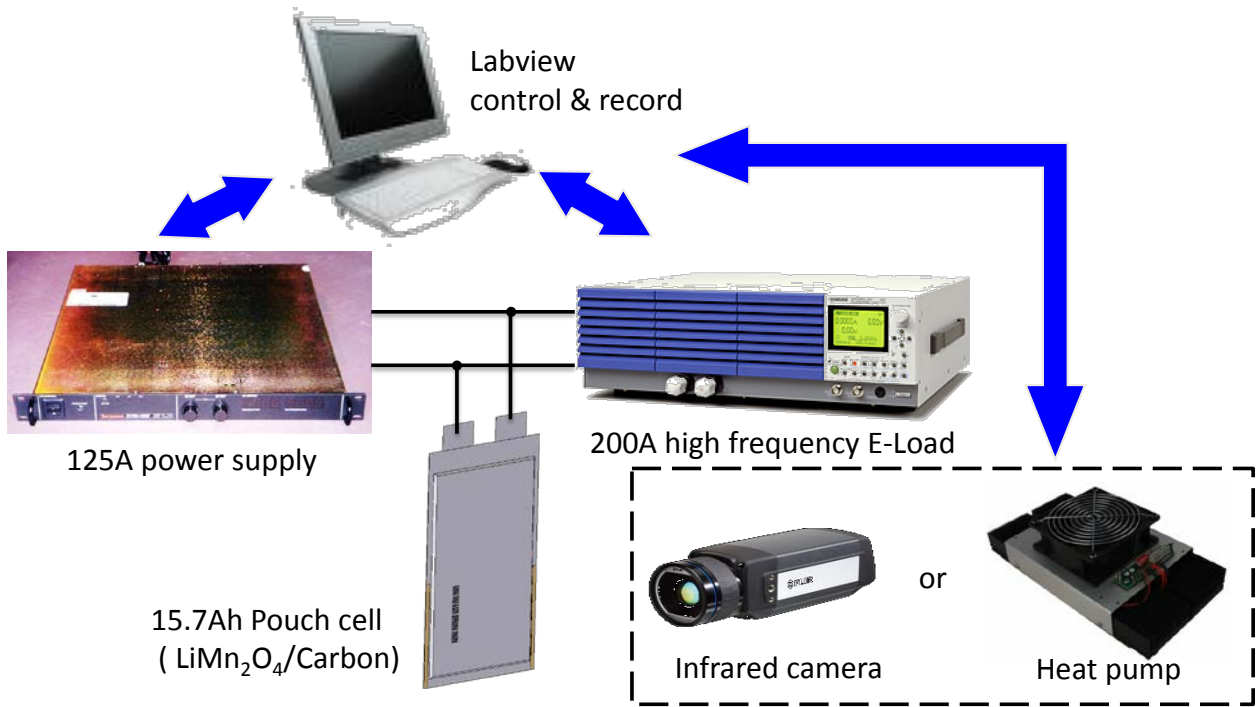
Figure 3-21 Test setup

The experiment setup should be designed to implement following functions.

1. Monitor and control the voltage, current and temperature of the battery.
2. Power supply and E-load be able to work simultaneously in order to create adjustable current ripple whose amplitude, frequency and duration can be arbitrarily changed
3. Overcharge & over-discharge protection circuit

4. Fast response heat pumps and fixture that precisely control heat flow

The Labview code should have following functions

1. Have constant current (CC) mode, constant voltage (CV) mode for both charging and discharging
2. Have current ripple mode
3. Be able to filter and record data at independent sample frequency with control loop
4. Overcharge and over-discharge protection code
5. Script-driven

3.5.2 Discharging and charging behavior

Simulation and experiment results of discharging characteristics of a pouch cell are compared in Figure 3-22, where the terminal voltages at different current rates are plotted as a function of time. The pouch cell used for the experiments has a capacity of 15.7Ah and its dimensions of the active area are 149.2mm by 197 mm. When a discharging current is applied, the terminal voltage drops instantaneously because of ohmic resistances present in the cell. Then, the voltage drops linearly because of the change of the OCV induced by the change of SOC. At the end of each discharge, the experimental shows that the change of the OCV becomes large and as a result the voltage drops drastically. In addition, it should be noted that all of the charges discharged is a function of the current rate. For example, when discharged at 1C, 93% of the maximum capacity is released, while 85% of capacity is released when discharged at 10C.
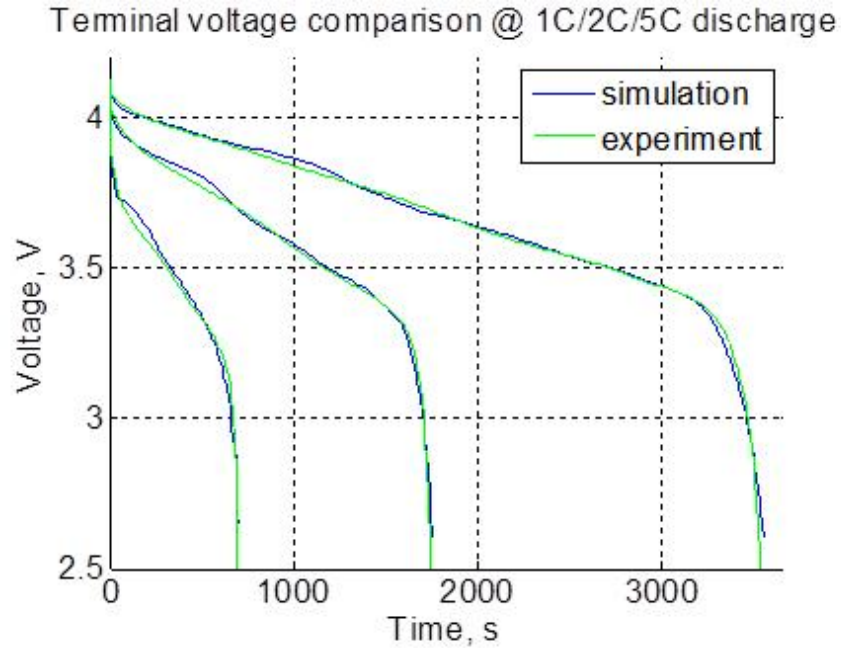
Figure 3-22 Discharge characteristics at different current rates

(Ambient Temperature=294K and SOC=100%)

The cell is firstly charged with the CC mode until the terminal voltage reaches 4.2V and then a constant terminal voltage is applied until the cell is completely charged. While CV charging, the current decays slowly. Simulation and experiment results are compared in Figure 3-23, where four different current rates of 20A, 40A, 60A and 80A are applied.
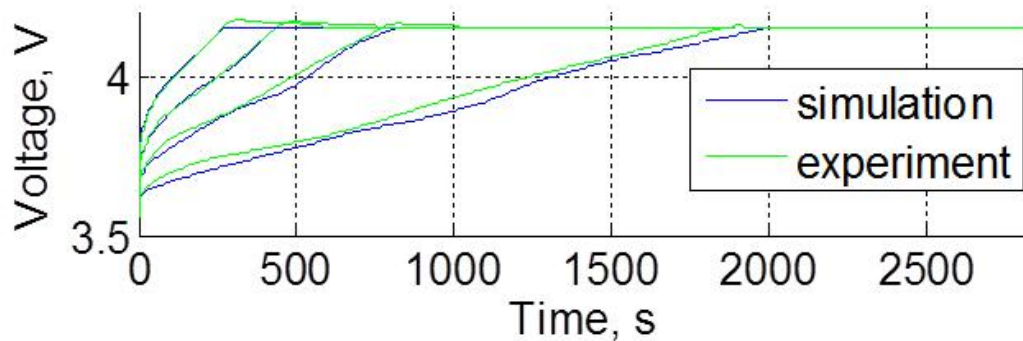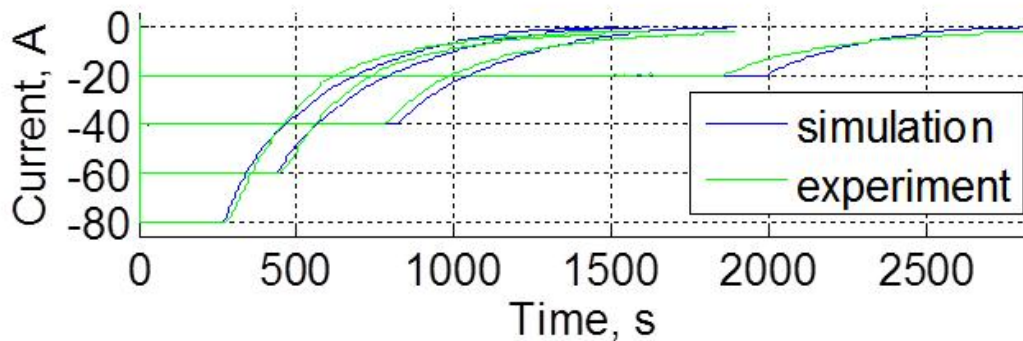
Figure 3-23 Charge characteristics at different rates in CC and CV mode

Comparison of discharging and charging characteristics at the different C rates shows that the model developed can predicts the performances.

3.5.3 Dynamic analysis

In order to assess dynamic responses of the model, an operating condition for a single cycle is defined with initial SOC of 41% and discharge current rate is 5C for 200 seconds, rest 200 seconds, charge at 5C current for 200 seconds then rest 200 seconds. Comparison of simulation and experiment voltage response is shown in Figure 3-24.
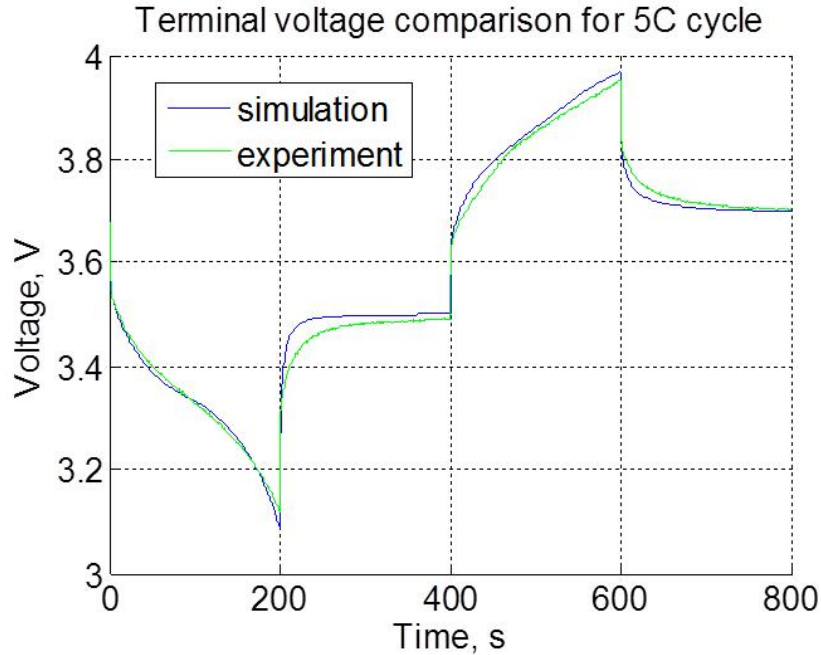
Figure 3-24 Voltage response at a single cycle with 5C charging and discharging rate.

In addition, temperature distribution between experiment and simulation is compared in Figure 3-25, where the temperature of the cell is captured using IR camera. The temperature distribution in the cell is asymmetric because of the different conductivities of two current collectors. Temperature rise around the positive tab is higher than that that in the negative tab. In addition, more heat is generated during discharge process because of exothermic reactions. The temperature increase during discharging is always greater than that of charging at a given current rate. The calculation for individual heat source terms shows a distribution of Joule heating in electrolyte (38%), heat of mixing (24%), heat caused by activation losses (16%), change of entropy (10%), Joule heating at SEI(8%), Joule heating at the current collectors (4%) and others.
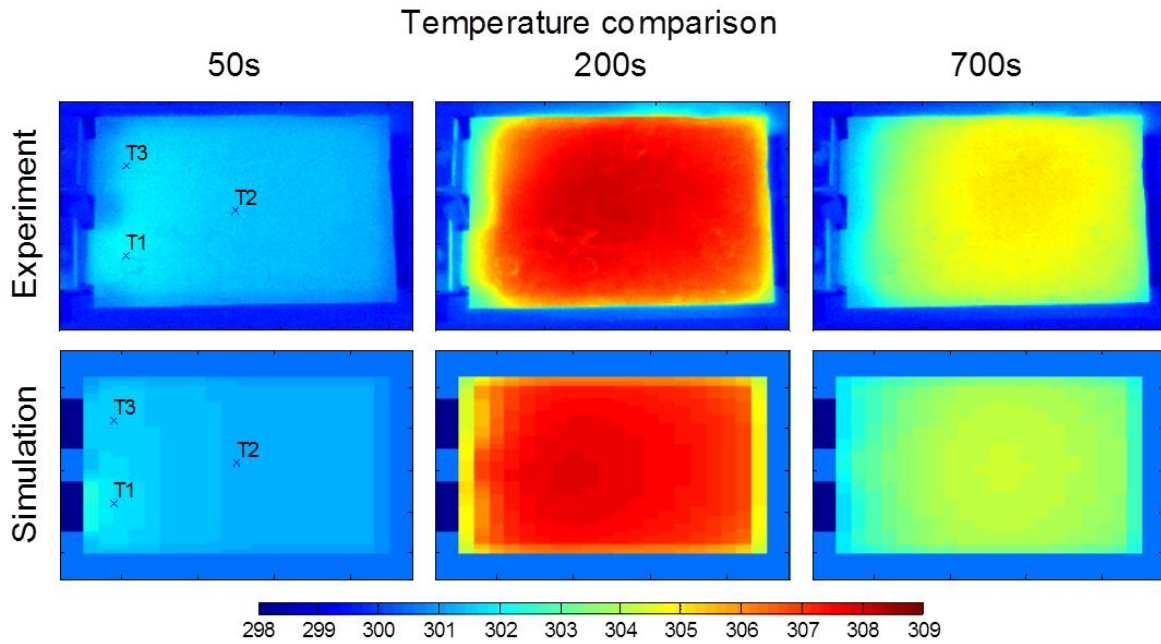
Figure 3-25 Temperature distribution of the cell

Temperature of three locations of the cell are measured and compared with that of the simulation as shown in Figure 3-26. The simulation results follow the experiment results with some time delay and errors that are possibly affected by the heat transfer between the cell and air flow in a thermal chamber.
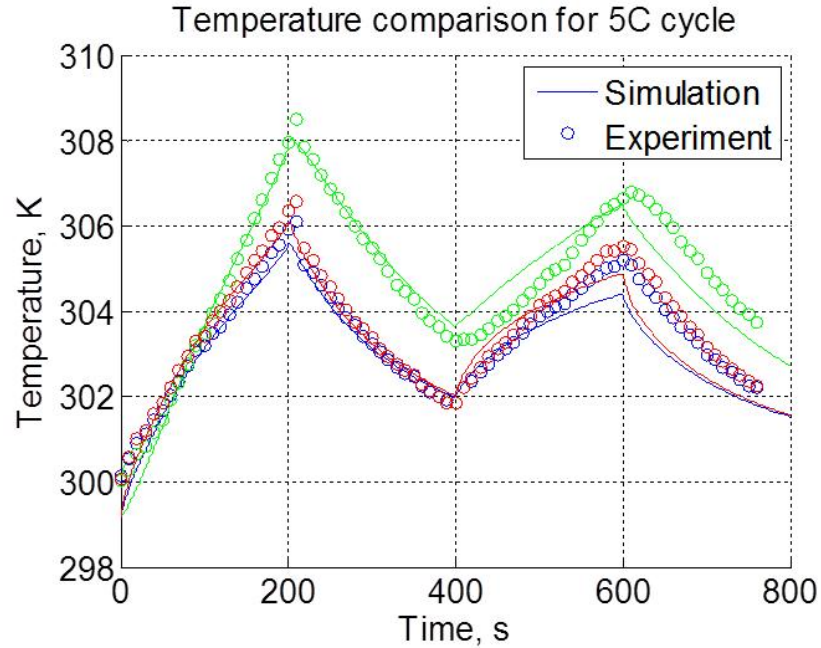
Figure 3-26 Temperature comparison at three locations.

3.6   Summary

We developed a high resolution quasi-three dimensional model for a pouch type of lithium polymer cell with a chemistry of LiMn$_2$O4 /Carbon for electrodes. The model is constructed using a one dimensional microcell based on electrochemical and thermal principles and experimentally validated against static and dynamic performance of a cell.

Analysis shows following interesting findings:

1. Due to different conductivities of the two current collectors, asymmetrical distribution of the current and voltage field is observed. The asymmetric current field causes non-uniform heat generation rates on the current collectors. Particularly, more heat is generated on the current collector located near the terminal tabs. Similarly, the

asymmetric voltage field affects the reaction rates of micro cells, so heat generation rates and the associated DOD are different dependent upon location.

2. Contribution of individual heat source terms are analyzed, where the heat caused by Joule heating in electrolyte and heat of mixing are the major parts at the 5 C rate.

The model developed is capable of representing not only current and voltage at the terminal tabs of a single cell but also distribution of ion concentrations, potentials, internal currents, and temperature when a battery is charged or discharged. Future work includes measurement of the individual heat source terms and validation of the model for other ambient temperature ranges.

4   Thermal analysis

4.1   Introduction

Lithium ion batteries are widely used in transportation and grid applications because of their higher energy and power density compared to other rechargeable batteries. These applications require a long lifespan with low degradation. When a battery is charged and discharged, ions are transported from cathode to anode and vice versa, while electrons flow through an external circuit from one electrode to the other. The charge transport, reduction, and oxidation processes continuously generate heat that can affect these processes and the degradation. Operation of a battery in an elevated temperature accelerates electrolyte and binder decompositions that lead to a capacity fade. In addition, the reaction products can reduce the accessible surface area of the electrode particles, which leads to a power fade [31]. A comparison at elevated operating temperatures from 278K to 318K shows that the capacity fade and the power fade rate at 318K were eight and two times, respectively, higher than those at 278K [32]. Therefore, battery manufacturers put enormous effort into optimizing the design for the high thermal stability of the materials and less degradation [33]. In addition, temperature affects other parameters like diffusion coefficients, conductivities and reversible heat generation [34]. Moreover, the large amount of heat generated in modules or a pack should be properly rejected to prevent a thermal runaway and minimize the temperature effects on cell performances and degradation [35]. Therefore, accurate estimation of the heat generation rate is crucial not only for the design of the battery, but also for allowing safe operations.

Heat of a battery is described by two source terms, the reversible and irreversible heat. The reversible heat is produced by the change of entropy at an operating cell temperature, which is expressed by a product between the change of entropy and the working temperature. On the other hand, the change of the entropy can be expressed using the open circuit voltage (OCV), so the reversible heat can be determined by measuring the open circuit voltage (OCV) when the cell temperature varies and a function of state-of-charge (SOC).

The profile of reversible heat is inherent and depends upon not only materials used for design of electrodes but also their manufacturing processes [36]. Conversely, the irreversible heat sources are a function of the overpotentials with discharging or charging current [37][38][39][40]. For the first time, Rao calculated that the irreversible heat is continuously generated even though the current applied to the cell goes to zero. He calculated the enthalpy change in the electrode bulk and found heat generation due to changing rate of ion concentration gradient. This portion is called the heat of mixing is not negligible only when the OCV curve changes rapidly [41]. However, the author did not consider the heat generated in the particles of electrodes along the radial direction. This effect was included by Thomas [42]. In addition, the change of entropy in $LiNi_{0.8}Co_{0.2}O_2$/carbon coin cells at different SOC was measured for the temperature range from 294K to 302K using a water bath. However, the results did not show effects of the heat of mixing because the current applied was too low to generate any observable heat of mixing. The principle for this measurement was based on the energy balance, where the heat source was obtained from the difference between the heat exchanged with environment and the heat accumulated that is proportional to battery temperature changing rate. Batteries left in environment of the open air [43][44] can be thermally affected by the surrounding air flow or turbulences and might have a

changed convection coefficient that deteriorates the accuracy of the measurement of heat exchange with environment.

Forgeza used two thermal couples. One was inserted into a cylindrical LiFePO$_4$/carbon battery and others was placed at a surface to measure both inside and outside temperatures and to calculate a heat transfer [45]. Seemingly, this method is accurate since the convection coefficient affected by air flows is not used for the measurement, but only works for the cylindrical batteries that allows for placement of a sensor inside of a cell.

Other researchers have used commercial isothermal calorimeters to measure the heat generation rate [38][46]. However, to accommodate the battery geometry the calorimeter cavities must be filled with some materials, which results in a relatively large thermal time constant, so that the measurement of a quick heat generation is not possible. In addition, most commercially available calorimeters are designed for testing thermal stability of materials, so the installed power is not large enough to match the high power battery cell.

Therefore, we have designed a special calorimeter using two thermoelectric devices that allows for dynamic characterization of the heat source terms of a high power cell. The designed calorimeter is firstly calibrated for the LiMn$_2$O$_4$/carbon pouch type power cell and then used to estimate the heat of mixing dynamically. The electrochemical thermal model developed previously is used to calculate the heat generation and compare with the experimental data [47].

4.2 Electrochemical and thermal model

4.2.1 Electrochemical model

The electrochemical model used for this research was first proposed by Doyle [48]. The model assumes that a cell has five layers that are sandwiched: anode current collector, anode, separator, cathode and cathode current collector, as shown in Figure 4-1. The electrodes are composed of uniformly distributed spherical particles with electrolyte filling in the gaps between particles as well as the pores in the separator. Chemical reactions take place only at interface between electrodes particles and electrolyte. When charged and discharged, lithium ions generated may be present in both electrolyte and electrodes and diffuse in different directions, while free electrons exist only in the electrode particles. When one electrode releases a given number of lithium ions to the electrolyte the number of free electrons is generated inside the electrode particles, so charge is conserved. The released ions in the electrolyte are transported through the separator and finally end to the other electrode, while the electrons go through outer circuit to the other electrode, and they combine at the interface between the electrolyte and particles of that electrode.
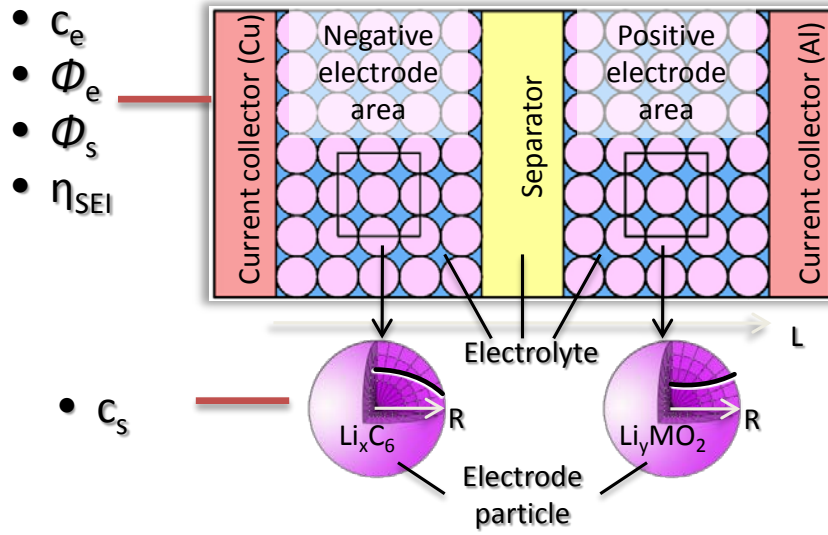
Figure 4-1 Set-up for modeling of Lithium ion battery.

The equations used for the electrochemical model are summarized below and are discretized in the radial direction (*R* direction) of particles with 10 and through-the-plane direction (*L* direction) with 25. The discretized equation is solved with an implicit method and details can be found in a previously published paper [47].

Reaction kinetics	
$$j^{Li} = a_S \cdot i_0 \left(\exp\left(\frac{\alpha_a \cdot n \cdot F}{R \cdot T}(\eta - \eta_{SEI}) \right) - \exp\left(-\frac{\alpha_c \cdot n \cdot F}{R \cdot T}(\eta - \eta_{SEI}) \right) \right)$$	(4-1)
Electrolyte conductive	
$$\frac{\partial}{\partial l}(\kappa_e^{eff} \cdot \frac{\partial}{\partial l}\phi_e) + \frac{\partial}{\partial l}(\kappa_{D,e}^{eff} \cdot \frac{\partial}{\partial l}(\ln c_e)) + j^{Li} = 0$$	(4-2)
Solid conductive	

$$\frac{\partial}{\partial l}(\sigma^{eff} \cdot \frac{\partial}{\partial l}\phi_s) = j^{Li} \qquad (4\text{-}3)$$

Electrolyte ion transport

$$\frac{\partial(\varepsilon_e c_e)}{\partial t} = \frac{\partial}{\partial l}(D_e^{eff} \cdot \frac{\partial}{\partial l}c_e) + \frac{1-t_+^0}{F}j^{Li} \qquad (4\text{-}4)$$

Solid ion transport

$$\frac{\partial c_s}{\partial t} = \frac{D_s}{r^2}\frac{\partial}{\partial r}\left(r^2\frac{\partial c_s}{\partial r}\right) \qquad (4\text{-}5)$$

4.2.2 Heat generation review

The total heat generation in a lithium ion battery (Q_{sum}) is divided into two terms, reversible heat, $Q_{rev,}$ and irreversible heat, Q_{irr}.

$$Q_{sum} = Q_{rev} + Q_{irr} \qquad (4\text{-}6)$$

The reversible heat generation is given by equation (4-7),

$$Q_{rev} = -I \cdot T \cdot \frac{\partial U_{OCV}}{\partial T} \qquad (4\text{-}7)$$

where I is the terminal current, which sign is defined as positive when discharged. T is the temperature in the battery and U_{OCV} is the open circuit voltage.

The irreversible heat generation can be expressed by two ways as shown in equation (4-8) and equation (4-9).

Equation (4-8) assumes that the voltage difference between the U_{OCV} and terminal voltage includes a sum of all of voltage drops caused by electron and ion transport and chemical reactions, as shown below. Multiplication with the current results in the irreversible heat,

$$Q_{irr} = I \cdot (U_{OCV} - V_t) \tag{4-8}$$

where the open circuit voltage, U_{OCV}, is the function of SOC.

The heat source can be estimated when the U_{OCV} and V_t are known. This equation is simple to understand, but the term becomes zero when the current becomes zero, so that the heat of mixing is not considered.

The other formulation for the irreversible heat generation as shown in equation (4-9) is also widely used [44][49][50][51][52][53][54]. The equation includes two terms, the reaction term and Ohmic heating that are derived from the electrochemical formulation,

$$\begin{aligned} Q_{irr} &= Q_{reaction} + Q_{ohm} \\ Q_{reaction} &= \int j^{Li} \cdot (\phi_s - \phi_e - U_{equ}) \cdot dV \\ Q_{ohm} &= \int [\sigma^{eff} (\nabla \phi_s)^2 + \cdot (\kappa^{eff} \cdot \nabla \phi_e + \kappa_D^{eff} \nabla \ln c_e) \cdot \nabla \phi_e] \cdot dV \end{aligned} \tag{4-9}$$

where j^{Li} is the current density and defined to be positive for the current from electrode to electrolyte, ϕ_s is the electrode potential, ϕ_e is the electrolyte potential, σ^{eff} and κ^{eff} are the effective conductivities in electrode and electrolyte and κ_D^{eff} is the effective diffusion conductivity in electrolyte.

Equation (4-9) does not consider the heat generation by solid phase lithium diffusion that is defined as enthalpy heating [41]. In order to explain the enthalpy heating, chemical energy is introduced, which is defined as the energy stored in a battery by means of chemical reactions.

If the charging and discharging current are low, it can be assumed that the terminal voltage always equals to the OCV and the battery is in quasi-steady state, so no irreversible heat is generated. Then, the chemical energy at a given SOC is defined as the total electrical energy input from 0% SOC to the given SOC,

$$E_{chem}(SOC) = \int_0^{SOC} Q_{max} \cdot U_{OCV} \cdot dSOC \tag{4-10}$$

where Q_{max} is the maximum capacity of the battery that is constant. It should be noted that the chemical energy is only a function of SOC.

On the other hand, the enthalpy heating for a particle can be expressed based on the decreasing rate of the chemical energy of the particle and the electric power that the particle produces. The decreasing rate of the chemical energy is a product of the local reaction rate of the particle, j^{Li}, with the average equilibrium potential inside of the particle, U_{avg}, while the electric power is equal to the product of the local reaction rate of the particle, j^{Li}, with the equilibrium potential at the surface of the particle, $U_{s,e}$. As a result, the enthalpy heating becomes $j^{Li} \cdot (U_{avg} - U_{s,e})$. Transient behavior of enthalpy heating (Blue line) as function of reaction rate (Green line), average equilibrium potential (colorful line), and equilibrium potential at the interface (Black line) in the radial direction are shown in Figure 4-2 using the electrochemical model. It is assumed that the battery is discharged with 7C at t=0, where the initial equilibrium potential is 4.95V. The reaction rate increases, but not linearly because of the change of ion concentration in L direction, while the equilibrium potential at the interface decreases because of the increased surface concentration until a sudden voltage drop given by OCV. When the discharging current is interrupted, the cell becomes relaxed and gets recovered. Accordingly, the enthalpy heating calculated by multiplication of the reaction rate and potential difference

increases relatively slowly at the beginning, drastically and finally returns to zero. The amount of the enthalpy heating can be more than half of total irreversible heat generation.
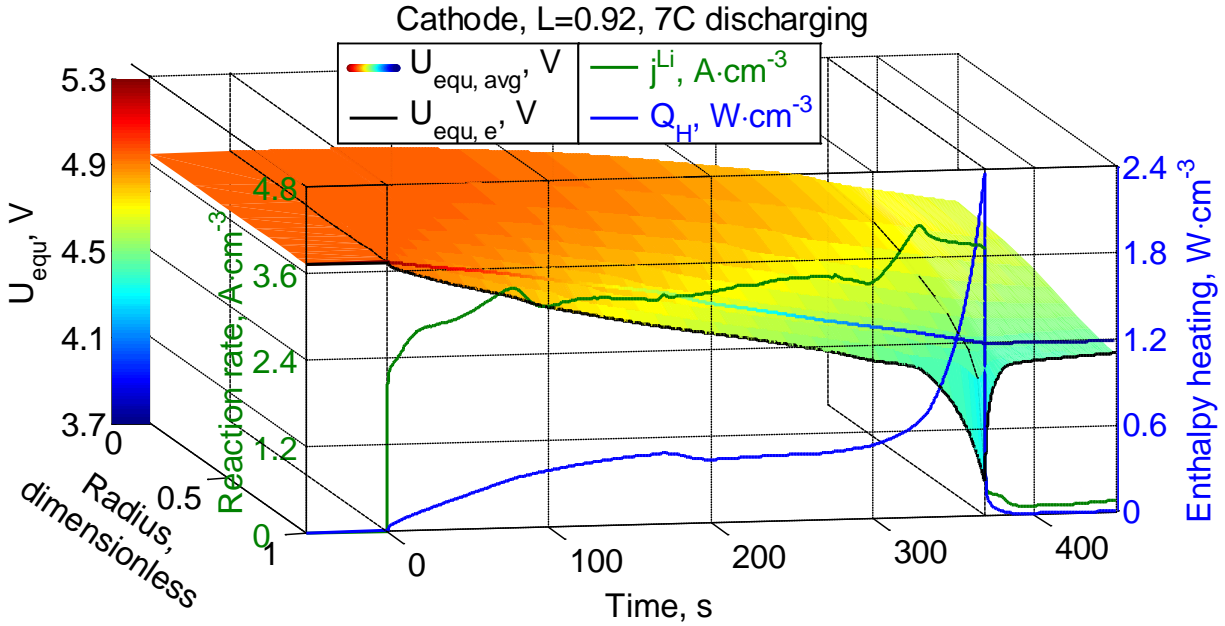
Figure 4-2 Transient behavior of enthalpy heating as function of reaction rate and equilibrium potential in the radial direction.

The heat of mixing is a new source term that is caused by the transient behavior of ion concentrations and the nonlinearity of the equilibrium potentials of electrodes. When the battery is charged and discharged, there is a period of time that the ion concentrations in the particles are not uniformly distributed, so the SOC at every location is different than the given average SOC. As a result, the equilibrium potentials at the every location are different than the equilibrium potential at the average SOC.

$$(\overline{U(SOC)} - U(\overline{SOC})) \cdot Q_{\max} \qquad (4\text{-}11)$$

It is assumed that there are two adjacent control volumes in a particle with concentrations, c_{s1} and c_{s2}, the equilibrium potentials, U_1 and U_2, the average potential, U_{avg}, can be obtained by

70

averaging both U values. After the cell is relaxed, the final potential which is called the mix potential, U_{mix}, might be higher or lower than before because the equilibrium potentials are not linear. The enclosed area between the two different potentials at the given range of concentrations presents the heat of mixing as shown in Figure 4-3.
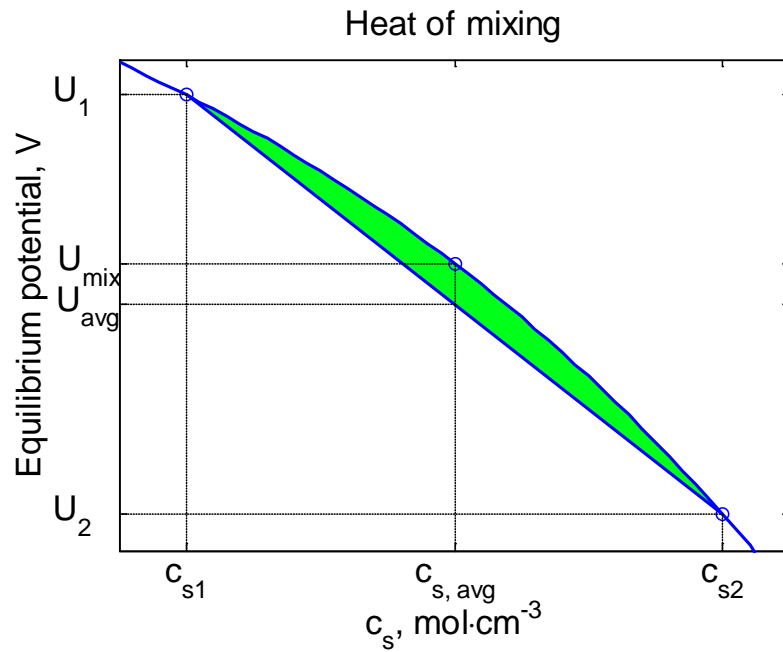
Figure 4-3 Heat of mixing.

In order to evaluate the equation (4-9), the heat generation in a battery for a capacity of 10Ah is calculated using the parameters given in the reference [51], where the effect of the reversible heat generation is removed by discharging the battery at 2C for 360 seconds, and then charging at 2C for 360 seconds.

After the battery has rested long enough, the state is the same as the initial state. The total reversible heat generation is zero, while the total irreversible heat generation is equal to the enclosed area by the terminal voltage for charging and discharging, as shown in Figure 4-4(a).

The OCV curve separates the hysteresis area into two areas that are exactly the same as that of the irreversible heat generations at the discharging and charging calculated from equation (4-8). The amount of the heat generated is 875J. Conversely, the irreversible heat generation calculated from equation (4-9) is a much smaller amount of 390J that is much less than the previous one, as shown in Figure 4-4(b), which is presumably because the calculation using equation (4-9) does not include the enthalpy heating. It should be noted that the difference is not negligible.
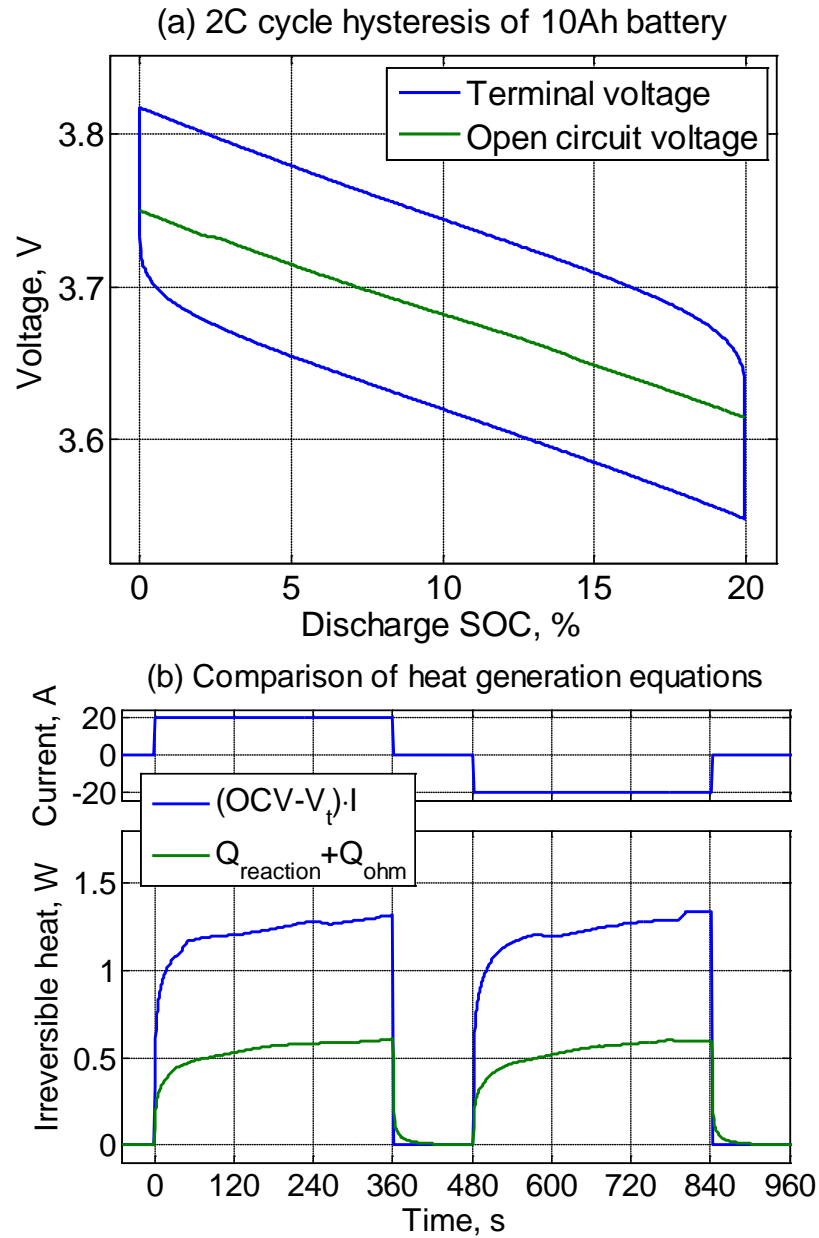
Figure 4-4 Simulation of a battery at 2C charging and discharging.

4.2.3 New formulation for irreversible heat generation

The proposed irreversible heat generation considers both the enthalpy heating and the heat of mixing, which is derived from the chemical energy of the battery.

Charging and discharging a battery can be described using energy balances. When a battery is charged, electric energy is transferred from the source to the battery and increases the chemical energy. However, part of the electric energy is dissipated as an irreversible heat. Conversely, when a battery is discharged, the chemical energy of the battery is transferred to the electric energy, while the part of chemical energy is dissipated as a heat, too. When the discharging current is defined to be positive, the irreversible heat generation rate can be expressed using the electric power input and the chemical energy increase rate, as shown in equation (4-12),

$$Q_{irr} = -I \cdot V_t - \frac{dE_{chem}}{dt} \tag{4-12}$$

The chemical energy can be expressed as follows,

$$\frac{dE_{chem}}{dt} = Q_{max} \cdot U_{OCV}(SOC) \cdot \frac{dSOC}{dt} \tag{4-13}$$

where SOC denotes the average SOC that can be calculated from the ion concentration in the solid phase of both electrodes,

$$
\begin{aligned}
SOC_- &= SOC = \frac{\overline{c_{s-}} - c_{s-,0\%}}{c_{s-,100\%} - c_{s-,0\%}} \\
SOC_+ &= 1 - SOC = 1 - \frac{\overline{c_{s+}} - c_{s+,0\%}}{c_{s+,100\%} - c_{s+,0\%}} \\
\frac{dSOC_-}{dt} &= \frac{1}{c_{s-,100\%} - c_{s-,0\%}} \frac{dc_{s-}}{dt} \\
\frac{dSOC_+}{dt} &= -\frac{1}{c_{s+,100\%} - c_{s+,0\%}} \frac{dc_{s+}}{dt}
\end{aligned}
\tag{4-14}
$$

where the c_s is the solid phase ion concentration distribution in the L and R direction in electrodes shown in Figure 4-1, $c_{s,100\%}$ and $c_{s,0\%}$ are the solid phase lithium concentration when SOC is 100% and 0%, respectively, and V is the volumes of two electrodes.

Similarly, the maximum capacity, Q_{max}, can be expressed using the solid phase ion concentration,

$$
\begin{aligned}
Q_{\max} &= Q_{\max-} = Q_{\max+} \\
Q_{\max-} &= \varepsilon_{s-} \cdot F \cdot V_- (c_{s-,100} - c_{s-,0}) \\
Q_{\max+} &= \varepsilon_{s+} \cdot F \cdot V_+ (c_{s+,0} - c_{s+,100})
\end{aligned}
\tag{4-15}
$$

where ε_s is the active material volume fraction and F is the Faraday constant.

It should be noted that when SOC increases, the lithium ion concentration in the anode increases, while the ion concentration in the cathode decreases, so that they have an opposite sign. On the other hand, the OCV is the difference between the two electrodes equilibrium potentials as follows:

$$
U_{OCV}(SOC) = U_{equ+}(c_{s,+}) - U_{equ-}(c_{s,-})
\tag{4-16}
$$

Substituting equation (4-12) by (4-13)(4-14)(4-15)(4-16) and taking into account the non-uniform distribution of solid phase lithium concentration, a new formulation is found for calculation of the irreversible heat generation as follows:

$$
Q_{irr} = -I \cdot V_t + F \cdot \varepsilon_{s_+} \cdot \int_{V_+} U_{equ+} \cdot \frac{dc_{s+}}{dt} \cdot dV + F \cdot \varepsilon_{s-} \cdot \int_{V_-} U_{equ-} \cdot \frac{dc_{s-}}{dt} \cdot dV
\tag{4-17}
$$

Hence, the variables of both U_{equ} and c_s are a function of the R and L coordinate. Since the equation is derived from the energy balance and considering the chemical energy that is only a

function of SOC, the energy is conserved. In addition, the concentrations that might be present after the terminal current becomes zero represent dynamic behavior of the heat source.

4.3   Characterization of heat sources

4.3.1   Design of a calorimeter and test station

Calorimeters are widely used to measure heat generation rates of batteries, but do not provide the dynamics needed for step charging and discharging of cells because of limited heat transfer capability given by cavities and the power needed for cells. A new calorimeter was designed using two thermoelectric devices (TEM) and used to validate the proposing heat generation rate. When comparing the proposed irreversible heat generation equation (4-17) with the conventional equation (4-8), the most obvious difference between these two equations is the transient behavior when the load current becomes zero. The first term of equation (4-17) disappears, but the other two terms, which represent the heat of mixing, are still present. The heat generated after the interruption is dependent upon the instantaneous concentrations in both electrodes that are functions of the amplitude of the current before the interruption. Therefore, the calorimeter should respond very rapidly and reject a large amount of heat, so that high power heat pumps are required.

The battery used for the experiments is a pouch type power cell with dimension of active materials about 20cm×15cm×5mm and made of $LiMn_2O_4$ and carbon. Its capacity is 15.7Ah and the operating voltage is from 2.5V to 4.15V. The test station was constructed using a DC power supply and an electronic load. LabVIEW embedded in a PC was used to control the power supply, the e-load and the TEMs, as depicted in Figure 4-5. A high resolution current transformer

and four thermocouples were employed to accurately measure the current and the surface temperatures. Two thermocouples were located near the terminal tabs and others were on the both sides of the battery center.
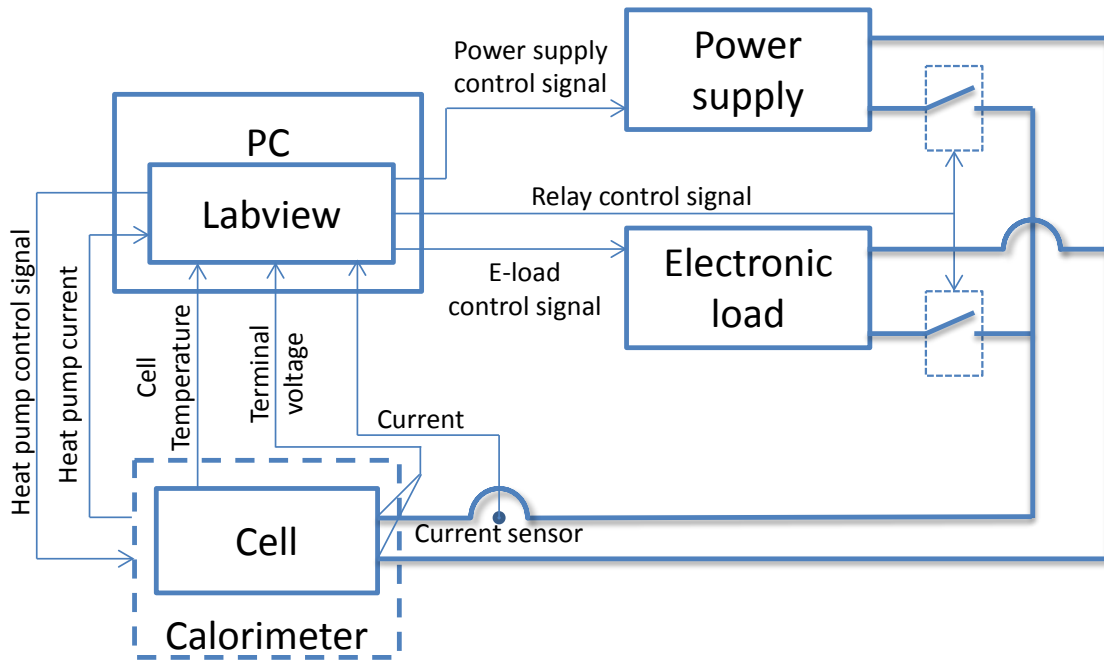
Figure 4-5 Experimental setup.

The calorimeter was designed using two TEMs as heat pumps, where the battery is placed between the two TEMs, for which the maximum cooling power is 160W. Carbon based thermal sheets were used to improve heat conduction between the battery and the TEMs as shown in Figure 4-6. The TEMs are connected in series and powered by a 20A high frequency bipolar power supply that is controlled by the PC via LabVIEW.
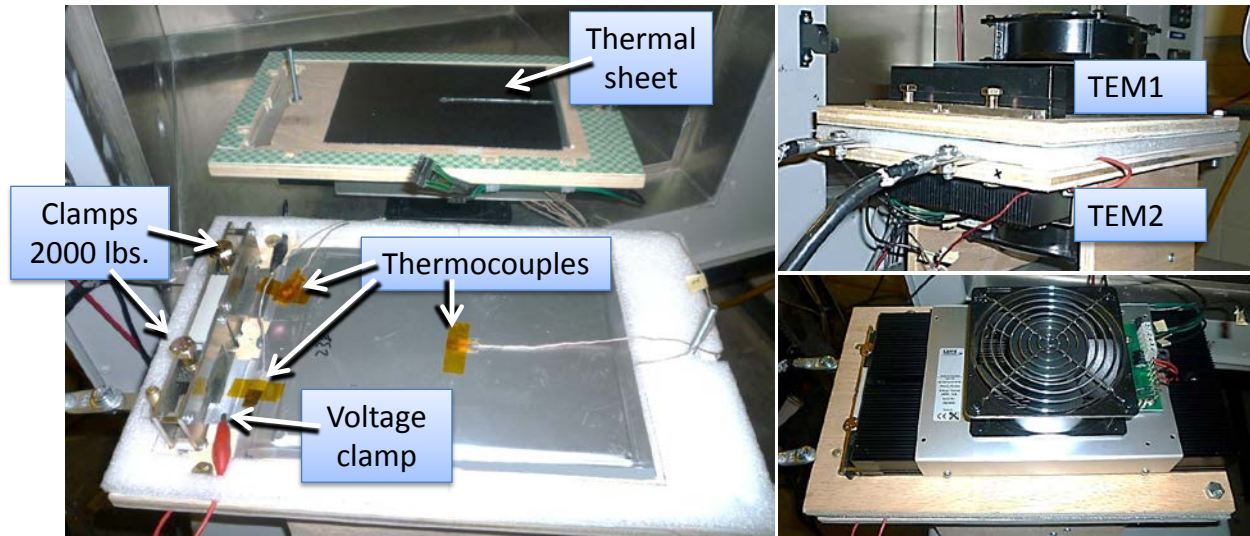
Figure 4-6 Calorimeter setup.

The contacts between the terminal tabs and clamps may have a high resistance and the associated high voltage drop can cause relatively high heat generation, so special attention should be paid to design of the clamps. Experimental tests of the effects of clamping force on contact resistance showed that the forces more than 2000 lbs on each tab produce a minimum contact resistance. In addition, the mechanical stress and heat capacity of the clamp are optimized using ANSYS. The terminal voltage is measured between tabs, so that effects of the contact resistance are excluded.

4.3.2 Static calibration

Before using the calorimeter for characterization of heat sources, calibrations have been conducted with respect to static and dynamic responses.

According to the manufacturer's manual, the heat pump rate of TEM is given as follows,

$$Q_{pump} = k_1 \cdot I_{TEM} - k_2 \cdot I_{TEM}^2 + k_3 \cdot (T_{cool} - T_{hot})$$ (4-18)

where Q_{pump} is the heat pump rate, I_{TEM} is the input current for the TEM, and T_{cool} and T_{hot} are the temperatures on the both sides of TEM. k_1, k_2 and k_3 are the constants that should be determined.

The first, second and third terms represent the heat pump rate, the heat generation, and the heat conduction, respectively. Under the assumption that the operating temperature of the calorimeter is the same as the ambient temperature, the third term becomes zero.

In order to characterize the TEM with respect to the heat generation, an AC input current without an offset is first applied and then the average temperature at the location between the TEMs and battery increases. Since a constant average temperature is desirable for any AC input currents, different DC offset (Green) are added to the input current. The average temperature at the location between the TEMs and battery follows the input currents with a transition behavior caused by cooling and heating behavior of the TEM that compensates the offset, as shown in Figure 4-7, while no current is applied to the battery. Based on the experiment data, an empirical equation, Offset=0.0474 (TEM current)^2, is derived.
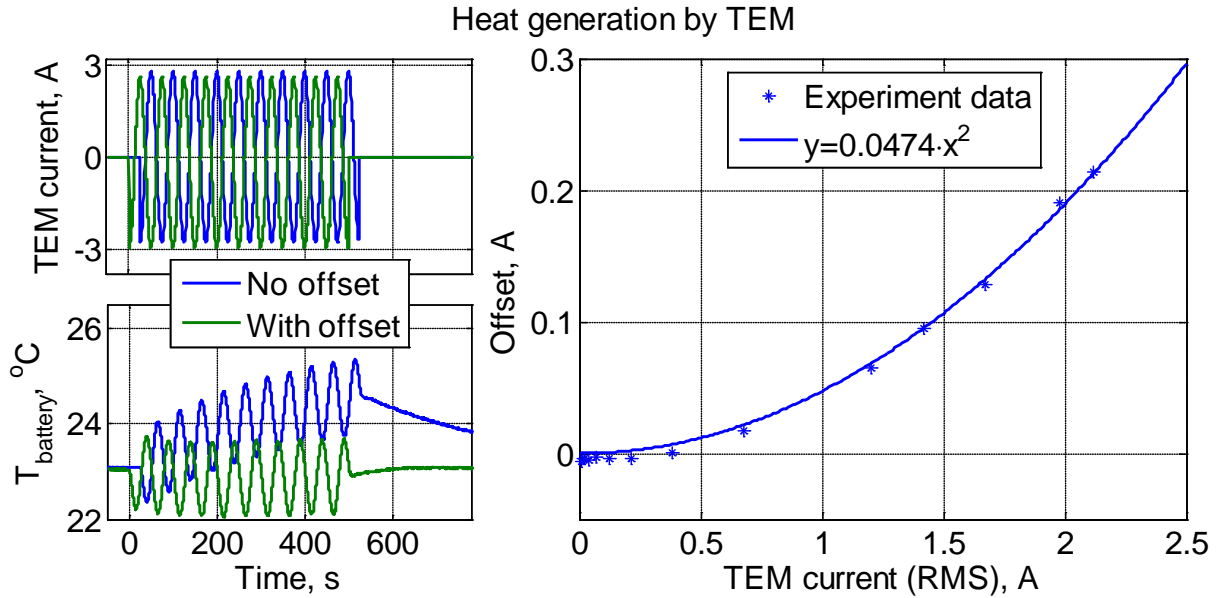
Figure 4-7 Heat generation by the TEM.

The heat pump rate constant can be determined when heat sources and the TEM input current are known. When the battery acts like a pure resistance, the heat generated in the battery can be simply calculated and used to determine the constant.

Impedance of the battery using the electrochemical impedance spectroscopy (EIS) and terminal voltage versus currents are shown in Figure 4-8. When the frequency of the current applied is 1Hz, the imaginary part of the impedance of the battery becomes zero, the battery acts purely resistively with a resistance of 1.9mΩ. When the amplitude of the current varies for charging and discharging, the terminal voltage follows the amplitude proportionally and the slope is the same as the resistance measured by the EIS.
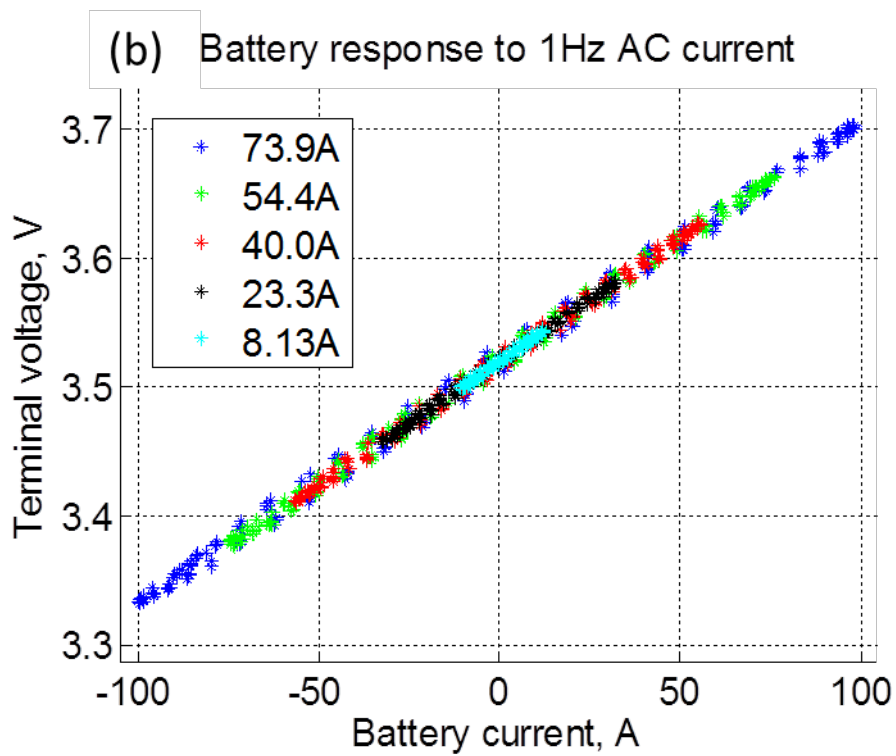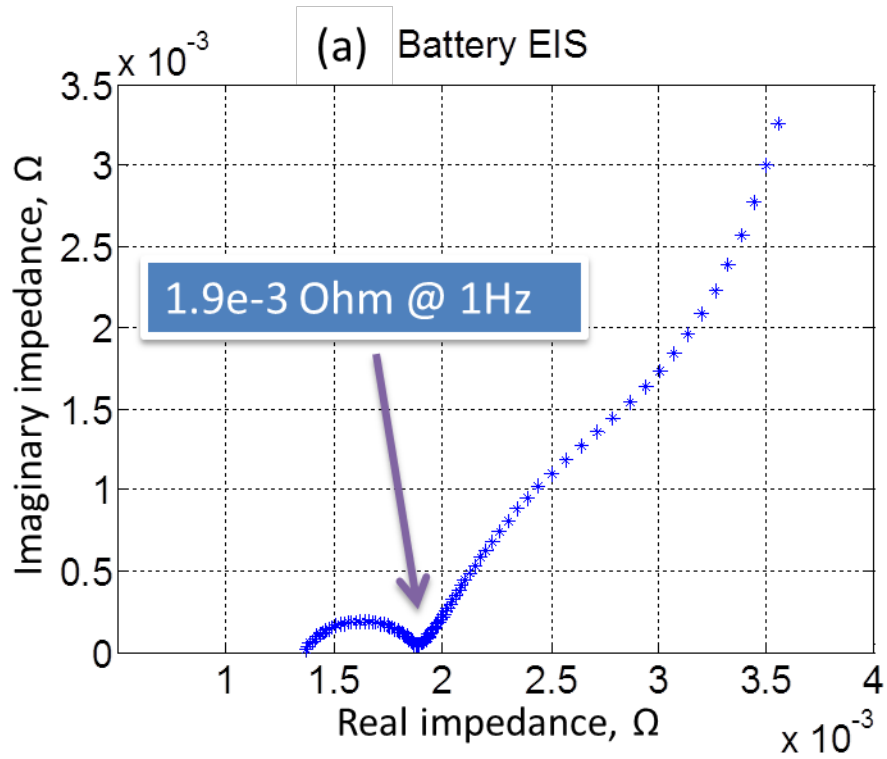
Figure 4-8 a) EIS characteristic of the battery b) Terminal voltage versus current.

In addition, heat generation of the clamps, which is regarded as an extra heat transfer from the clamps to the battery, is considered. The amount of the heat transfer is given from the product of temperature difference and the heat transfer coefficient derived from the experimental data, where the temperature difference is the average value of both clamps minus the temperature at the center of the battery. After compensating for the heat generation by the TEM and the effects of the clamps by means of the heat transfer through terminal tabs at a constant heat generation of the battery, a relationship between the input current for the TEM and the heat pump rate that rejects the heat generation is plotted in Figure 4-9. The results show that the cooling power produced by the heat pump is proportional to the input currents for the TEM, so that the TEM can be used as an actuator that produces rejecting heat. The heat pump constant is 50.1W/A.
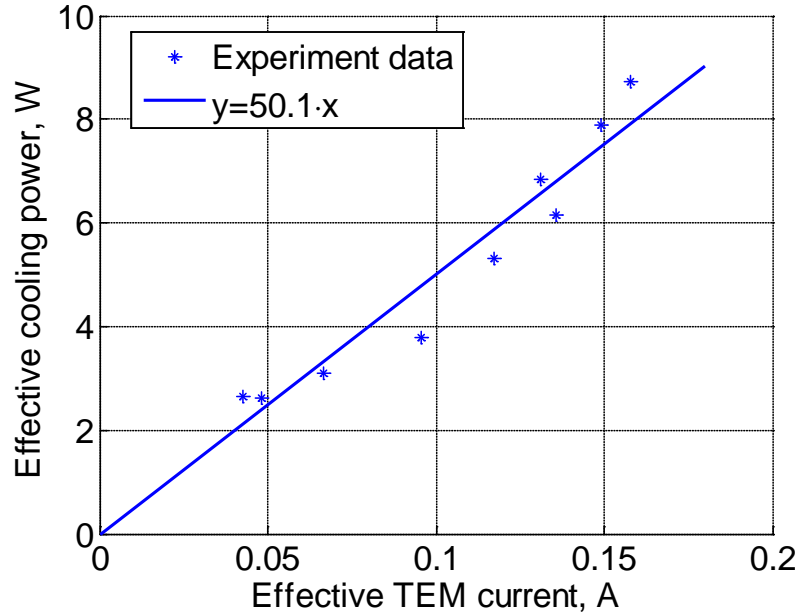
Figure 4-9 TEM heat pump constant

4.3.3   Dynamic calibration

When a battery is charged and discharged with currents steps, heat generation rates follow the abrupt changes of the current. In order to estimate the heat generation accurately, the calorimeter is calibrated for a better dynamic response. One phenomenon in the TEM is the delay between the input currents for the TEM and the associated heat pump rate. The TEM is made of P- and N-type semiconductors alternately connected in series and arranged such that the direction of the heat carried is the same as that of carriers moving. The semiconductors are four millimeters thick and cause a delay in a range of several milliseconds when a current is applied to the TEM [55]. However, this delay is not significant. On the other hand, a metal plate and a heat sink are mounted to the PN semiconductors of the TEM as shown in Figure 4-10, where the metal plate is in contact with the battery.
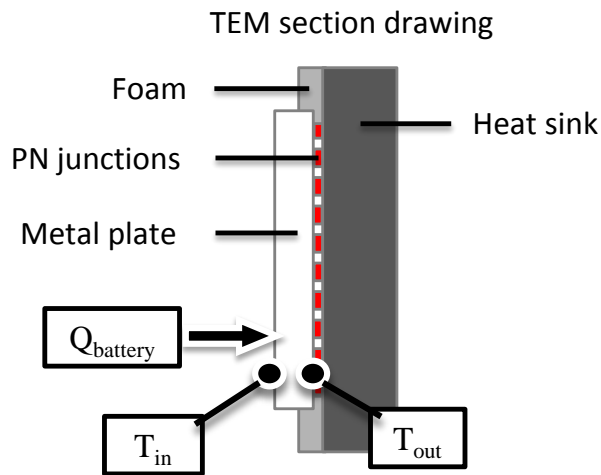
Figure 4-10 Structure of TEM

The limited thermal conductivity and capacitance of the plate cause a time delay that is dominant in the response. In order to improve the dynamic response of the calorimeter, the

temperature delay is measured and compensated for using a Kalman filter that requires a dynamic heat transfer model for the plate. The heat transfer model used for estimations is as follows,

$$\frac{d}{dt}\begin{pmatrix} T_{in} \\ T_{out} \\ Q_{battery} \end{pmatrix} = A \cdot \begin{pmatrix} T_{in} \\ T_{out} \\ Q_{battery} \end{pmatrix} + B \begin{pmatrix} T_{terminal} \\ I_{TEM} \end{pmatrix} \tag{4-19}$$

where the temperature of the plate on battery side and the semiconductor is T_{in} and T_{out}, respectively, and $Q_{battery}$ is the total heat generated in the battery. $T_{Terminal}$ and I_{TEM} denote the temperature at the terminal and the current for TEM, respectively.

Since the T_{in} is the only state variable that can be measured, the other two state variables are estimated using the Kalman filter. Particularly, the Kalman filter is employed to suppress white noise present in the temperature measurements. The diagonal values of the covariance matrix for the filter selected are 10^{-6}, 10^{-6} and 1. The value of the measurement covariance selected is 10^{-4}. A proportional controller is used to avoid overshoot. The schematic diagram for estimation of the variables and controls is shown in Figure 4-11.
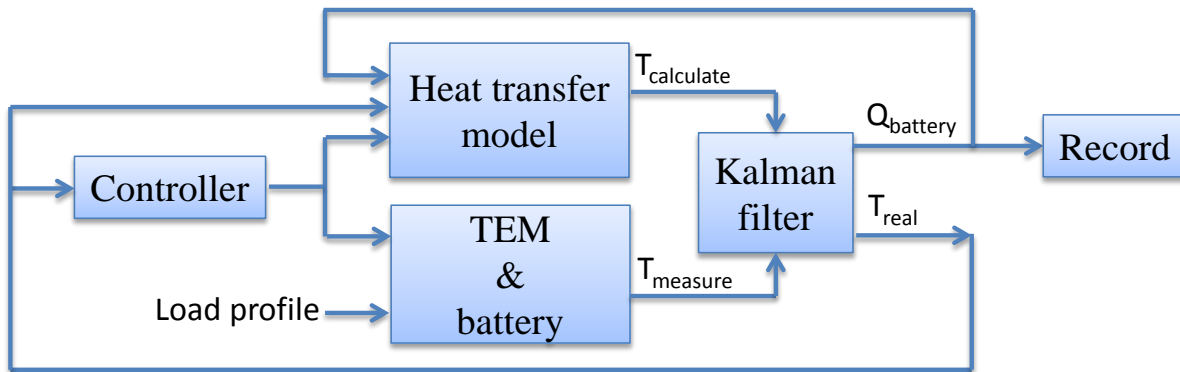
Figure 4-11 Kalman filter used to improve dynamic response

The calibration results are shown in Figure 4-12, where the AC current is applied to the battery and heat generations are plotted. The frequency of the current was 1Hz and the peak-to-peak amplitude was 200 amps. Two heat generation plots are presented, the one from OCV and terminal voltage (green line) and other from the calorimeter (blue line). The former one is calculated for each point as the average overpotential heating in the past cycle (one second). The plots on the right side show expanded views of the transient behaviors. It takes approximately seven seconds for the blue to catch up.
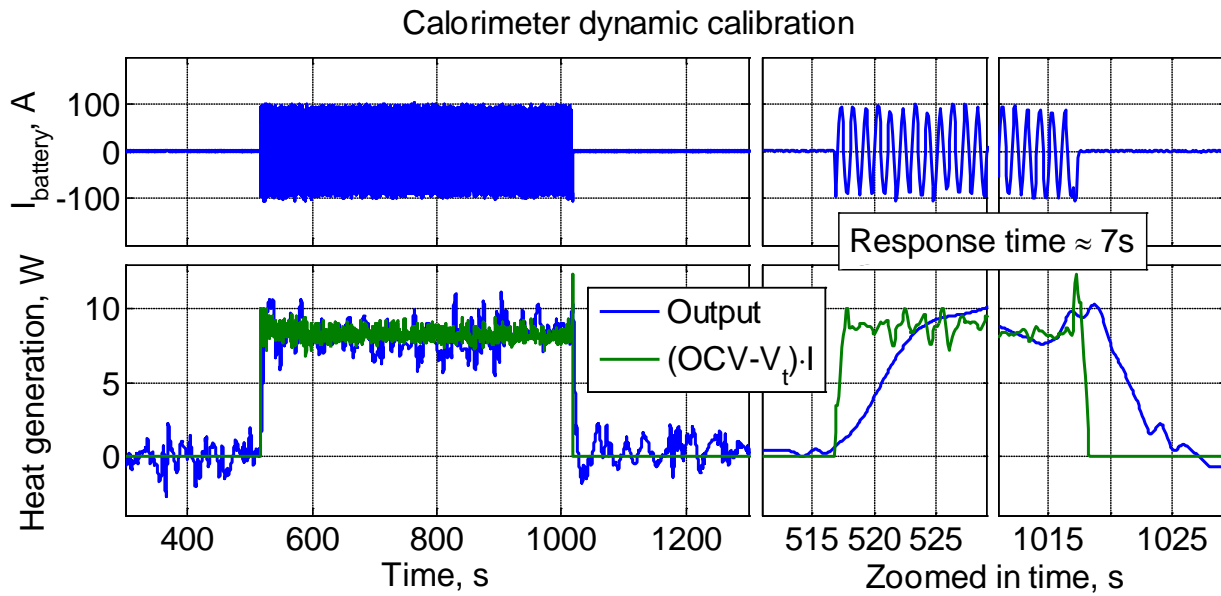
Figure 4-12 Dynamic calibration of calorimeter

4.4 Model validation and analysis

The total heat generation is measured when the battery is charged and discharged at different currents in the constant current (CC) mode. The ambient temperature is set to be 295K and the maximum temperature rise at the end of 110A discharge is set to 2.1K according to the heat capacity and heat conductivity obtained from the dynamic calibration.

Simulated and measured results at different current rates from 4.1C to 7C are shown in Figure 4-13, where the broken and solid lines represent the calculated data from traditional heat generation equation(4-8) under the assumption that the reversible heat generation is constant and the measured data, respectively.
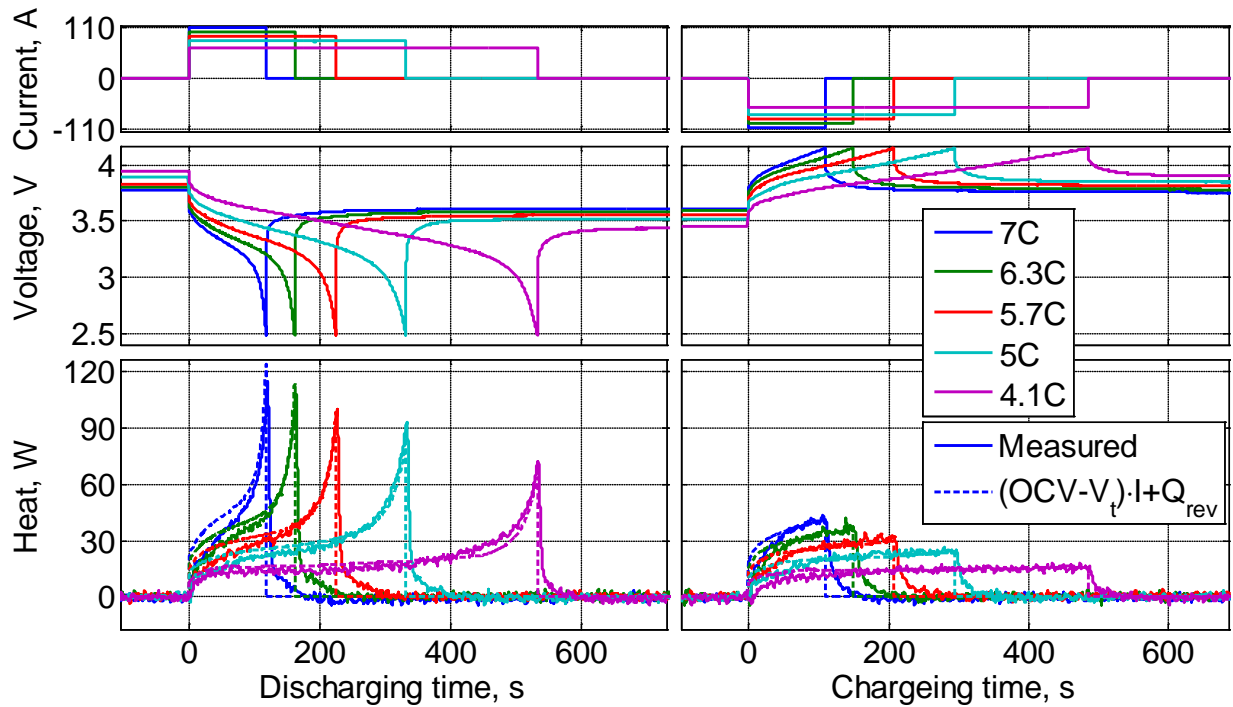
Figure 4-13 Heat generation measurements during cycles

The heat generation rate of the battery at the beginning of charging or discharging is less than those predicted by the calculation. And heat is continuously generated even though the current is equal to zero. The time span of the heat, presumably the heat of mixing, depends on the C rates. A high current results in a long time span. The heat of mixing decays to zero in one minute when 7C rate of discharging current is applied even though it only takes twenty seconds at the 4.1C charging.

In addition, the total amount of heat generation during charging or discharging is almost the same as that from the beginning to half of the charging and discharging time at the same C rate. By contrast, the heat generation at the end of discharging rises more rapidly than that at the end of charging because the open circuit voltage drops drastically at low SOCs. As a result, the solid phase concentration gradient at the end of discharging is much higher than that at the end of charging. The large concentration gradient leads to a large amount of enthalpy heating.

The current, voltage, and heat generation at the 5C rate charging and discharging are plotted in Figure 4-14, where the simulation results based on the electrochemical model including the proposed heat generation equation (4-17) is also added. It should be noted that the heat of mixing that explains the difference between total heat generation and overpotential heating is comparatively small during the constant current charging and discharging, but is not negligible after the current is interrupted.
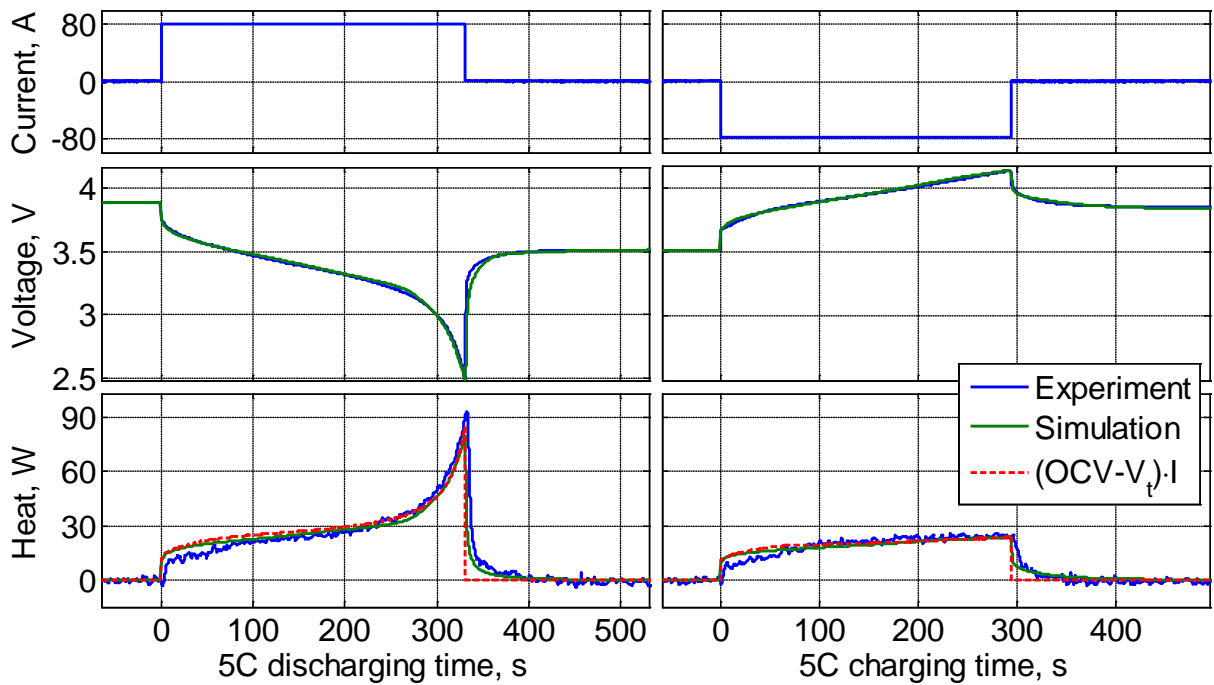
Figure 4-14 Comparison between measurement result and model calculation

The separated heat source terms are plotted in Figure 4-15, which includes the enthalpy heating, Joule heating and heat of entropy. The heat of entropy is the reversible heat that is negligible at this current. The Joule heating shows a similar generation rate as the time elapses. At the beginning of charging and discharging, local conductivities might be different, so that the current flows at spots that have high conductivities. As time elapses, conductivities decrease because of the increased activation overpotential and the current flow is evenly distributed. As a result the Joule heating increases. However, the exchange current density at the low SOC range is smaller than that at high SOC, so the Joule heating at the end of discharging is higher than that at the end of charging. Finally, the enthalpy heating is responsible for the peak at the end of discharge.
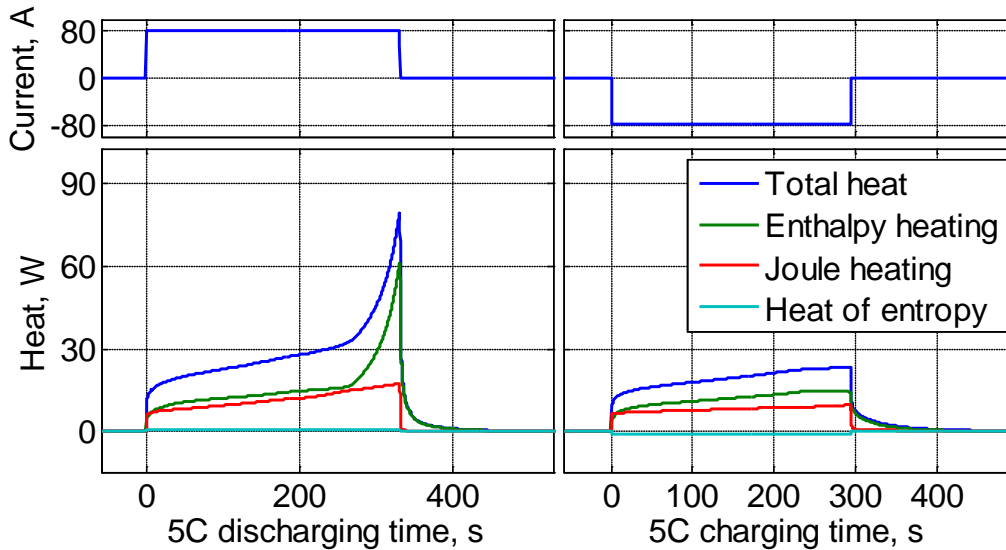
Figure 4-15 Simulation of heat source terms

The model validated above is used to calculate the individual heat source terms, where the battery is discharged from 4.1V to 2.5V and charged from 3.0V to 4.15V at different constant C rates. Average actual heat generation and the percentage of the heat over the total heat generation versus the currents is plotted with the black line, as shown in Figure 4-16, where the individual terms are also included. Since the average values of heat of mixing are zero, the integration of the absolute value is used for the calculation.
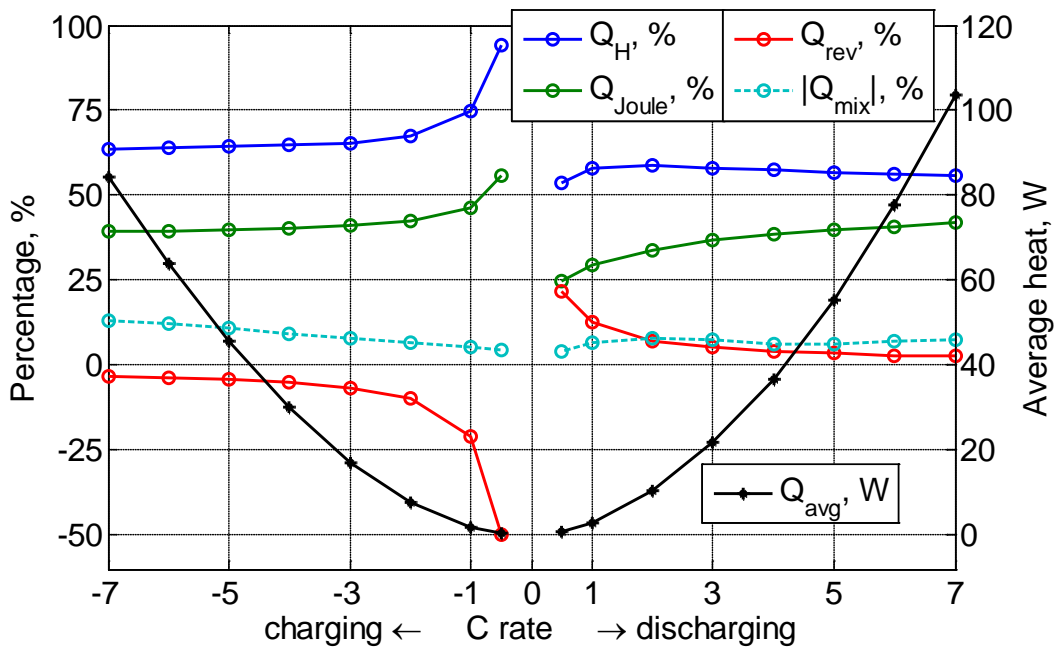
Figure 4-16 Analysis of heat source terms at different current rates

Since reaction and Ohmic heating have a shorter time constant than that of the designed calorimeter, both of them can be measured only as a sum (Joule heating), while the enthalpy heating can be measured alone.

4.5   Summary

Accurate estimation of heat source terms is one of crucial factors in not only optimizing a battery cell, but also modules and packs. In this paper, a new formulation for the heat generation is proposed that includes the enthalpy heating and heat of mixing. The formulation is incorporated into an electrochemical thermal model and used to analyze heat generation rates. In order to measure the heat generation dynamically, a new calorimeter was designed using two thermoelectric devices. The calorimeter was statically and dynamically calibrated using EIS and a dynamic error compensator designed based on Kalman filter. Finally, the calorimeter was used to measure the heat generation of a 15.7Ah $LiMn_2O_4$/carbon pouch type power cell.

Analysis using the model and experimental data shows several findings as follows:

- The reversible heat releases at discharging and absorbs at charging. The amount of the heat is significant at low current, but relatively small at high current;

- Theoretical and experimental analysis shows that the irreversible heat sources in general do not consider either enthalpy heating or heat of mixing. According to simulations, the major contributions to the irreversible heat source are enthalpy heating (55%~70%) and Joule (30%~45%).

- The heat of mixing is zero in average if both of two arbitrary states are steady, but the absolute value of the heat of mixing in average goes up to 13% of the irreversible heat generation. The heat of mixing continuously generates heat and decays to zero in about one minute after the current is interrupted.

There has been a discrepancy between the simulation and the experimental data within the first 100 seconds, which might result from the assumption that the transference number is constant. Future work will include effects of transference number on the heat generation. In addition, design of the calorimeter can be optimized for high resolution measurements even at low current ranges.

Parameters

	Parameter	Negative electrode	Separator	Positive electrode	unit	Ref.
Design specifications (geometry and volume fractions)	Thickness, δ	$50*10^{-4}$	$25.4*10^{-4}$	$36.4*10^{-4}$	cm	[51]
	Particle radius, R_s	$1*10^{-4}$		$1*10^{-4}$	cm	[51]
	Active material volume fraction, ε_s	0.58		0.5		[56]
	Polymer phase volume fraction, ε_p	0.048	0.5	0.11		[56]
	Conductive filler volume fraction, ε_f	0.04		0.06		[56]
	Porosity, ε_e	0.332	0.5	0.33		[56]
Solid and electrolyte phase Li^+ concentration	Maximum solid phase concentration, $c_{s,\,max}$	$40.6*10^{-3}$		$70.5*10^{-3}$	$mol \cdot cm^{-3}$	a
	Stoichiometry at 0% SOC: $x_{0\%}$, $y_{0\%}$	0.126		0.936		b
	Stoichiometry at 100% SOC: $x_{100\%}$, $y_{100\%}$	0.676		0.442		b
	Average electrolyte concentration, c_e	$1.2*10^{-3}$	$1.2*10^{-3}$	$1.2*10^{-3}$	$mol \cdot cm^{-3}$	[56]
Kinetic and transport properties	Exchange current density coefficient, k_{i0}	12.9		6.28	$A \cdot cm^{2.5} \cdot mol^{-1.5}$	[56]
	Charge-transfer coefficient, α_a, α_c	0.5, 0.5		0.5, 0.5		[48]
	Solid phase Li diffusion coefficient, D_s	$1.0*10^{-11}$		$5.40*10^{-12}$	$cm^2\,s^{-1}$	c
	Solid phase conductivity, σ	1		0.1	$S\,cm^{-1}$	[56]
	Electrolyte phase Li^+ diffusion coefficient, D_e	$2.6*10^{-6}$	$2.6*10^{-6}$	$2.6*10^{-6}$	$cm^2\,s^{-1}$	[56]
	Bruggeman's porosity exponent, p	1.5	1.5	1.5		[57]
	Electrolyte phase ionic conductivity, κ	$2.37c_e \exp(-8983c_e^{1.4})$		$2.37c_e \exp(-8983c_e^{1.4})$	$S\,cm^{-1}$	d
	Li^+ transference number, t_+^0	0.363	0.363	0.363		[58]

a. Calculated from capacity, stoichiometry numbers, and battery geometry.

b. Fitted from initial potential drops at different SOC during charging and discharging.

c. Fitted from discharge durations measured at different C rates.

d. Equation is from the reference [56] and its coefficients are fitted from overpotentials at different C rates during discharging.

5   High frequency electrochemical model

5.1   Introduction

Electrochemical Impedance Spectroscopy (EIS) is the technique that has widely used to study performance of electrochemical devices including lithium batteries. In 1986, Laman studied the effects of the geometry of a winding cylindrical Li-ion battery using EIS [59], where the equivalent circuit model was used to describe the impedances that represent electrochemical behaviors. The model was constructed by connecting resistors with capacitors that result in different magnitude and phase relationships at different exciting frequencies. In 1998, Munichandraiah could find out three semicircles by analyzing the lithium ion batteries using the EIS. The high frequency one is caused by film resistance and its capacitance, and the middle frequency one is from charge-transfer resistance and double-layer capacitance, while the low frequency one is due to diffusional impedance [60]. However, this paper has not studied effects of degradation of Li-batteries. Ning took the EIS technique and extracted parameters using the model mentioned above for 18650 Li-ion and investigated the parameter changes that represent capacity fades cells at different testing conditions [61] [63]. The low frequency semicircle obtained from EIS was found enlarged when cycled, because of the increased interfacial resistance of both electrodes [63]. In order to discriminate the EIS parameter changes on each electrode, symmetric coin cells were built where two electrodes have a same material, either anode or cathode material. It was found out that the increased charge-transfer resistance is the main reason for degradation, where the charge-transfer resistance in cathode is larger than in anode [64][65]. The interfacial behaviors for different solvents and salts in different

concentrations were also studied using the EIS [66]. For improvements of the accuracy of the equivalent circuit model, several authors replaced the capacitors with constant phase elements (CPE) that are combined resistors and capacitors and attempted to estimate SOC [67]. Some other people integrated Kalman filter to the model [68][69] so that the SOC estimation error can be reduced.

All of the studies using EIS are based on the equivalent circuit model. There are two obvious shortcomings. The first one is that the parameters in the electric equivalent circuit model (EECM) do not consider change of SOC or aging effects and represent specific physical quantities, which make it difficult to understand internal mechanisms. The second one that the data obtained is only valid for an operating point, where a small AC signal is applied. When the AC signal is superposed with a DC, the results are different because of the nonlinearity of cells characteristics. On the other hand, the electrochemical model proposed by Doyle [1] is based on physics and electrochemistry and was not able to present the high frequency response. In 1999, Ong realized importance of the high frequency response and proposed a model that consists of a resistor and a capacitor that mimics double-layer behavior. Accordingly, the Butler-Volmer equation in the electrochemical model was modified, which was validated at constant current discharge [70]. In the following year, Doyle added an empirical equation as function of overpotential for the double-layer charge that was incorporated into the Butler-Volmer equation. The resulting model is transformed to frequency domain model that is only a function of frequency [71]. Two approaches above use the electrochemical model to represent the frequency behavior of the li-batteries, but are lacking clear correlations between the parameters of the EECM and physical operating and material properties. In addition, they mismatch with experimental data when DC components are present at the exciting signal.

94

The double-layer effect responsible for the high frequency part of EIS was firstly observed in the charged mercury drop experiment [72]. A model for the double layer was proposed in 1908 by Gouy and improved by Chapman and Stern, which is called Gouy-Chapman-Stern model, for which an analytical solution exists. However, this model is only for no reaction and static boundary conditions. Recent progress in finite element methods enables to find a solution for complex boundary conditions, so that the double layer can be solved numerically. Most of the calculations for the double layer behavior published produce equivalent capacitance and ion concentration distribution for metal/ionic liquid interface under assumption that no reaction takes place [73]. Other researcher experimentally measured properties of the double layer for carbon aerogel/NaF solution like capacitance and resistance, when changing the average pore size, bulk concentration, and solid potential. The results were used to validate the model [74].

In fact, Gouy-Chapman-Stern model has a potential equation that is called the Poisson-Boltzmann equation. Borukhov modified the entropy term in the Poisson-Boltzmann equation by considering the contribution of unoccupied space in double layer, so that the maximum ion concentration can be limited in double layer even if there is a high potential difference between the solid and electrolyte. As a result, calculation accuracy has been increased at a high potential [75]. Kilic applied the idea above for static [76] and dynamic behavior [77]. Dynamics are reflected by setting the average concentration and the concentration difference between anion and cation as the two state variables. It should be noted that all of these approaches above assume that there is no reaction at interface.

In this work, a dynamic double layer model is proposed that is based on the Gouy-Chapman-Stern principle and considers reaction at interface of li-ion cell porous electrode. The model substitutes the static Butler-Volmer equation appeared in the previous electrochemical model

[47] [78]. In addition, the electrolyte transport equation is modified to represent the behavior for the medium frequency range. Moreover, the transference number is no more constant and is a function of fluxes of cations and anions. As a result, the high frequency response of electrochemical model is possible, so that the model exhibits the complete range the EIS behavior. The electrochemical model becomes capable of representing not only the behaviors in the time domain but also in the frequency domain.

5.2   Model description

The double layer behavior between the electrode and electrolyte is mathematically described and integrated into the electrochemical microcell model. The model is composed of five layers: negative current collector, anode, separator, cathode, and positive current collector. It is assumed that the composite electrodes are porous and composed of mixed electrolyte and particles that have a sphere shape and uniformly distributed, as shown in Figure 5-1. The electrolyte neighboring to particles is divided into two areas, the bulk area and double layer. The bulk area is the one, where the concentration distribution of the anion is equal to that of cation, so the region becomes electrically neutral. On the other hand, the double layer (DL) has a thickness of 1~10nm that is located right outside the electrode particles. The Stern plane is the nearest layer to the solid surface, where the anions can approach and which thickness is about 0.2nm. The distance between the Stern plane and the solid surface is assumed to be equal to the sum of an anion ion and a solvent molecule size [72].

The DL is not electrically neutral because of the abrupt change of the potential. The DL is depicted with cations (brown color) and anions (green color), as shown in Figure 5-1.

96

Transport of each of ions in the DL is affected by their own local chemical potential gradient determined by the electric static potential and the ion concentration gradient. For Lithium battery, lithium ion is regarded as cation, while PF_6^- is the anion resulting from the salt, $LiPF_6$. Lithium ions travel through the DL and participate in chemical reactions at the surface of the solid particles while the anions are blocked outside of the Stern plane.

The Lithium ions entered the electrode particles after chemical reaction and continue diffusing until the gradient of the concentration becomes zero.

On the other hand, the ionic current in the electrolyte is expressed as a derivative of the sum of anions and cations with respect to time. In order to describe ion transport in the electrolyte close to the solid, two regions are defined, a DL and bulk region that use two coordinates of R and *L* direction, respectively. The two coordinates are orthogonal to each other. Ions flux in L coordinate is very high compared to that in R coordinate because the ion flux in *L* direction is the sum of total ion fluxes given in *R* direction of a particle. However, the potential and concentration gradient in *R* direction is much higher than that in *L* direction because of the high potential of the DL. Therefore, it can be assumed that the effective mobility of both ions in the DL is smaller than that in the bulk.
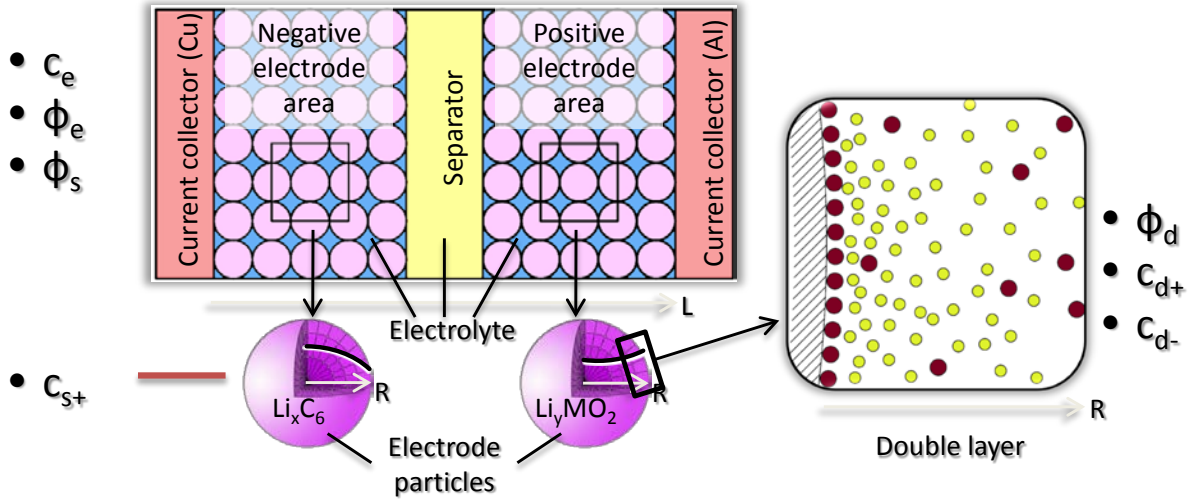
Figure 5-1 Set-up for high frequency Li-ion cell modeling

L is the coordinate for the through-the-plane that includes composite anode, separator, and composite cathode, while R is the coordinate for the radial direction that includes electrode particle and double-layer.

5.2.1 Important concepts in electrolyte

The bulk region and double-layer are part of electrolyte, where ion concentration and the potential distribution are firstly derived using the principle of thermodynamics. The Helmholtz free energy, F, is the useful work given by a difference between the internal energy and the entropy term and tends to take the lowest energy level.

$$F = U - TS \tag{5-1}$$

, where U is the internal energy, T is temperature and S is the entropy.

Since the electrolyte consists of dielectric solvent, cations and anions, the internal energy can be expressed by the three terms, the energy of static electric field, cations, and anions:

$$U = -\frac{\varepsilon}{2}|\nabla\phi|^2 + Fc_+\phi - Fc_-\phi \qquad (5\text{-}2)$$

, where ε is the constant for the permittivity of dielectric solvent, F is the Faraday's constant, c is the concentration of cations and anions, respectively, and ϕ is the potential field.

Since the electrolyte has a constant volume, the entropy can be expressed as a function of the concentration using the lattice gas formulation [75]:

$$S = -R \cdot c_+ \cdot \ln c_+ - R \cdot c_- \cdot \ln c_- - R \cdot (\frac{1}{N_A \cdot a^3} - c_+ - c_-) \cdot \ln(\frac{1}{N_A \cdot a^3} - c_+ - c_-), \qquad (5\text{-}3)$$

, where R is the ideal gas constant. N_A is the Avogadro constant. Anion and cation are assumed to be the same diameter, a.

The last term is the contribution of the free space that is not occupied by both ions. When the ion concentration is as high as the order of the theoretical maximum value $N_A^{-1} \cdot a^{-3}$, then the free space is low and the term becomes larger.

As a result, the Helmholtz free energy is expressed as a function of the potential and ion concentration. In order to calculate the minimum value of the energy, the Helmholtz energy equation is differentiated with respect to the potential and concentration. The first one yields the Poisson-Boltzmann equation:

$$\frac{\partial F}{\partial \phi} = \varepsilon \cdot \nabla^2\phi + F \cdot (c_+ - c_-) = 0 \qquad (5\text{-}4)$$

The equation above is not a function of the time. The second one results in a relationship for a chemical potential that determines transport of the ion species:

$$\mu_\pm = \frac{\partial F}{\partial c_\pm} = \pm F \cdot \phi + R \cdot T \cdot (\ln c_\pm - \ln(\frac{1}{N_A \cdot a^3} - c_+ - c_-))$$

(5-5)

The equation above is used to calculate ion flux in the charge conservation equation.

5.2.2 Ion transport in electrolyte bulk

Ionic current in the bulk can be expressed using ion flux density of cations and anions:

$$i_e = F \cdot (N_{e+} - N_{e-})$$

(5-6)

, where the subscript e denotes the bulk, i is the ionic current density, F is the Faraday constant, N_+ and N_- are the ion flux density of cation and anion, respectively.

In fact, the charges should be conserved in the bulk region. In addition, the bulk is electrically neutral. As a result, the cation and anion have the same concentration distribution. In the through-the plane direction, the charge conservation equation will be:

$$\frac{\partial c_e}{\partial t} = -\frac{\partial N_{e+}}{\partial l} + j_{E+}$$
$$\frac{\partial c_e}{\partial t} = -\frac{\partial N_{e-}}{\partial l} + j_{E-}$$

(5-7)

, where c_e is the concentration of cation and anion, l is the variable for the through-the-plane direction, N_{e+} and N_{e-} are the ion flux density of cation and anion, respectively, j_+ and j_- are the generation rate of cation and anion from the DL that will be discussed later in the section of double-layer boundary.

According to the dilute solution transport theory [72], interactions among a solvent and two ion species can be negligible, and the ion transport is only driven by the gradient of corresponding chemical potential that includes the potential and concentration term:

$$N_{e+} = -\frac{\varepsilon_e^{1.5} \cdot b_{e+}}{F} \cdot c_e \cdot \frac{\partial \mu_{e+}}{\partial l}$$
$$N_{e-} = -\frac{\varepsilon_e^{1.5} \cdot b_{e-}}{F} \cdot c_e \cdot \frac{\partial \mu_{e-}}{\partial l}$$

(5-8)

, where ε_e is the porosity of electrolyte, 1.5 is Bruggeman's porosity exponent [57], b_{e+} and b_{e-} are the mobility of cation and anion respectively, μ_{e+} and μ_{e-} are the chemical potential of cation and anion.

Since the ion concentration in the bulk is relatively low compared to the theoretical maximum concentration, the last term in equation (5-5) can be neglected:

$$\mu_{e+} = F \cdot \phi_e + R \cdot T \cdot \ln c_e$$
$$\mu_{e-} = -F \cdot \phi_e + R \cdot T \cdot \ln c_e$$

(5-9)

5.2.3 Ion transport in Double Layer (DL)

Ion transport in the DL is very similar to that in bulk except the spherical coordinate and some other conditions. Schematic diagram for the DL and bulk is depicted in Figure 5-2. For numerical calculation in the DL, the first grid is placed at the surface of electrode particle, the second one at the Stern plane, and finally the last grid is at the boundary between the DL and bulk. Beyond the boundary, it is assumed that the net charge is zero.
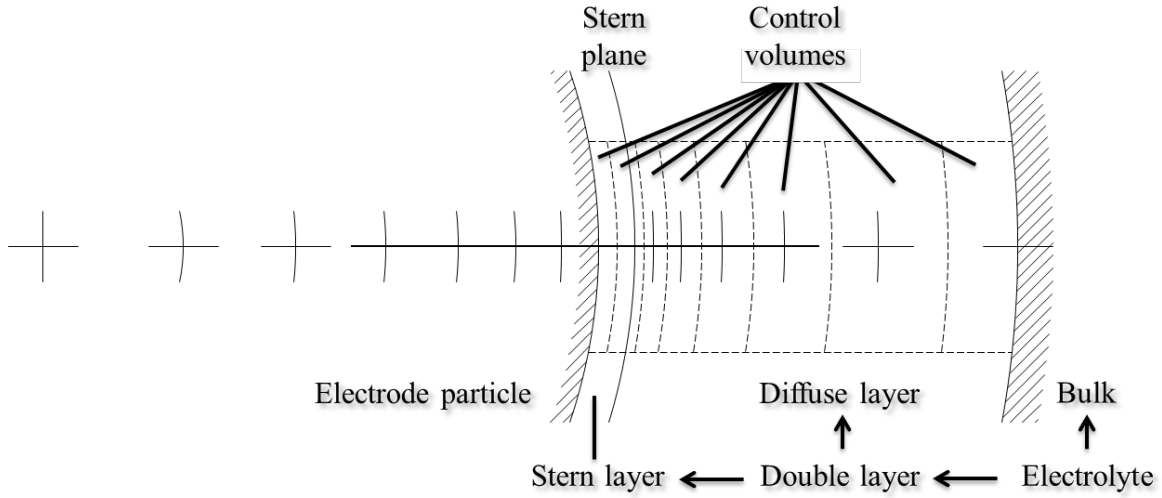
Figure 5-2 Meshing of electrode particle and double-layer

Since no ions are generated in the DL, so the equation for the charge conservation becomes:

$$\frac{\partial c_{d+}}{\partial t} = -\frac{1}{r^2} \cdot \frac{\partial(r^2 \cdot N_{d+})}{\partial r}$$

$$\frac{\partial c_{d-}}{\partial t} = -\frac{1}{r^2} \cdot \frac{\partial(r^2 \cdot N_{d-})}{\partial r}$$

(5-10)

, where r is the variable in the radial coordinate, and the subscript, d, denotes the DL.

Hence, ion flux of the cation and anion in the DL can be obtained from the equation below.

$$N_{d+} = -\frac{b_{d+}}{F} \cdot c_{d+} \cdot \frac{\partial \mu_{d+}}{\partial r}$$

$$N_{d-} = -\frac{b_{d-}}{F} \cdot c_{d-} \cdot \frac{\partial \mu_{d-}}{\partial r}$$

(5-11)

Since the anion concentration near the electrode surface is very high, the chemical potentials in equation above are calculated form equation (5-5). In addition, the Poisson-Boltzmann equation is used for the chemical potential given in equation (5-4) instead of the electrically neutral condition in bulk region.

5.2.4   Boundary conditions for DL

The DL in the spherical coordinate has two boundaries, the outer boundary with bulk and the inner boundary with electrode particles. Even though the outer boundary between the DL and bulk has two different coordinates, the ion flux at the both sides should be the same. The specific surface area is defined as the surface area of boundary per unit volume, a_S and a_E, as shown below. The first one is for the interface between particle and DL and the second one for the interface between the DL and bulk electrolyte, respectively:

$$a_S = \frac{3\varepsilon_S}{R_S}$$
$$a_E = \frac{(R_S + \delta_D)^2}{R_S^2} \cdot a_S$$

(5-12)

, where ε_s is the volume fraction of electrode, R_S is the average radius of electrode particle, δ_D is the thickness of the DL.

The ion flux at the interface between DL and bulk is as follows:

$$j_{E+} = a_E \cdot N_{d+,E}$$
$$j_{E-} = a_E \cdot N_{d-,E}$$

(5-13)

When a chemical reaction takes place, bond energy is needed to enable the reaction, which is a function of SOC. The energy for a reaction of a single ion is defined as $U_{S,equ}$ [eV], called the reaction equilibrium potential that is the difference of the chemical potentials between the solid and the electrolyte. From this relationship, the chemical potential of electrolyte phase lithium ion at the electrode surface is

103

$$\mu_{s+} = F \cdot \phi_s + R \cdot T \cdot \ln c_{s,d}$$
$$F \cdot U_{S,equ} = \mu_{s+} - \mu_{d,s+} \tag{5-14}$$
$$\mu_{d,s+} = F \cdot (\phi_s - U_{S,equ}) + R \cdot T \cdot \ln c_{s,d}$$

, where the subscript d denotes the DL, $c_{s,d}$ is the lithium ion solid phase concentration at the surface, and ϕ_s is the electric static potential of solid.

Since the charges are conserved, the number of electron participating in reactions is the same as that of ions. As electrons are negative charges, so the current generation by electrons in the solid equation (5-17) can be calculated from the lithium ion flux at interface between the electrode and the DL.

$$j_{S+} = a_S \cdot N_{d+, S} \tag{5-15}$$

Since the Stern plane is so close to the surface of the solid, no anion can reside within the plane, so that there is no anion flux from Stern plane to the electrode surface.

$$N_{d-, S} = 0 \tag{5-16}$$

5.2.5   Electrode

The current in electrode is carried by electron in thickness direction which is governed by Ohm's law.

$$\frac{\partial}{\partial l}(\sigma^{eff} \cdot \frac{\partial}{\partial l} \phi_s) = j_{s+} \tag{5-17}$$

, where σ^{eff} is the conductivity of electrode, and j_{s+} is the charge generation term introduced above which defined positive when flow from electrode to double layer.

The lithium ion in electrode particles is assumed only transport only in radius direction driven by concentration gradient.

$$\frac{\partial c_s}{\partial t} = \frac{D_s}{r^2} \frac{\partial}{\partial r}\left(r^2 \frac{\partial c_s}{\partial r}\right)$$

(5-18)

, where c_s is solid phase lithium ion concentration, r is the radius, and D_s is the diffusion coefficient.

5.3 Numerical analysis

5.3.1 DL without electric load

When no current flows through the external circuit, the terminal voltage is the same as the open circuit voltage (OCV) that ranges from three to four volts for Lithium battery depending upon SOC. The OCV is generally determined by the equilibrium potentials between solids and electrolyte, where the potential at the interface governed by Butler-Volmer equation has discontinuity because of the neglected DL. In fact, the potential should be continuous, simply because the first term for the potential in Poisson-Boltzmann goes to infinity when the potential changes with discontinuity. The potential drops dominantly occur at the DL rather than those in electrolyte bulk or electrodes because of the lowest value of the total free Helmholtz energy in the DL. At the equilibrium state where no reaction takes pleace, the chemical potentials of the solid and electrolyte are the same. The reaction equilibrium potential, $U_{s,equ}$, present in the chemical bond attract lithium ions from the electrolyte toward the solid, so that a concentration at the interface becomes low and a concentration gradient is formed across the DL. As a result, the electrostatic potential is changed according to equation (5-5) as well as the concentration of the

anions. Calculated potentials and concentration of ions in the DL is plotted in Figure 5-3. It is to recognize that the potential gradient inside the Stern plane is higher than the outside because the anions are attracted and reduces the gradient of potential. In addition, the calculation shows that the highest potential drop occurs from electrode surface to the Stern plane because no anion can reside inside the Stern plane. At the Stern plane, the net balance of charges reaches at its maximum and becomes zero at the bulk as well as the potential gradient.
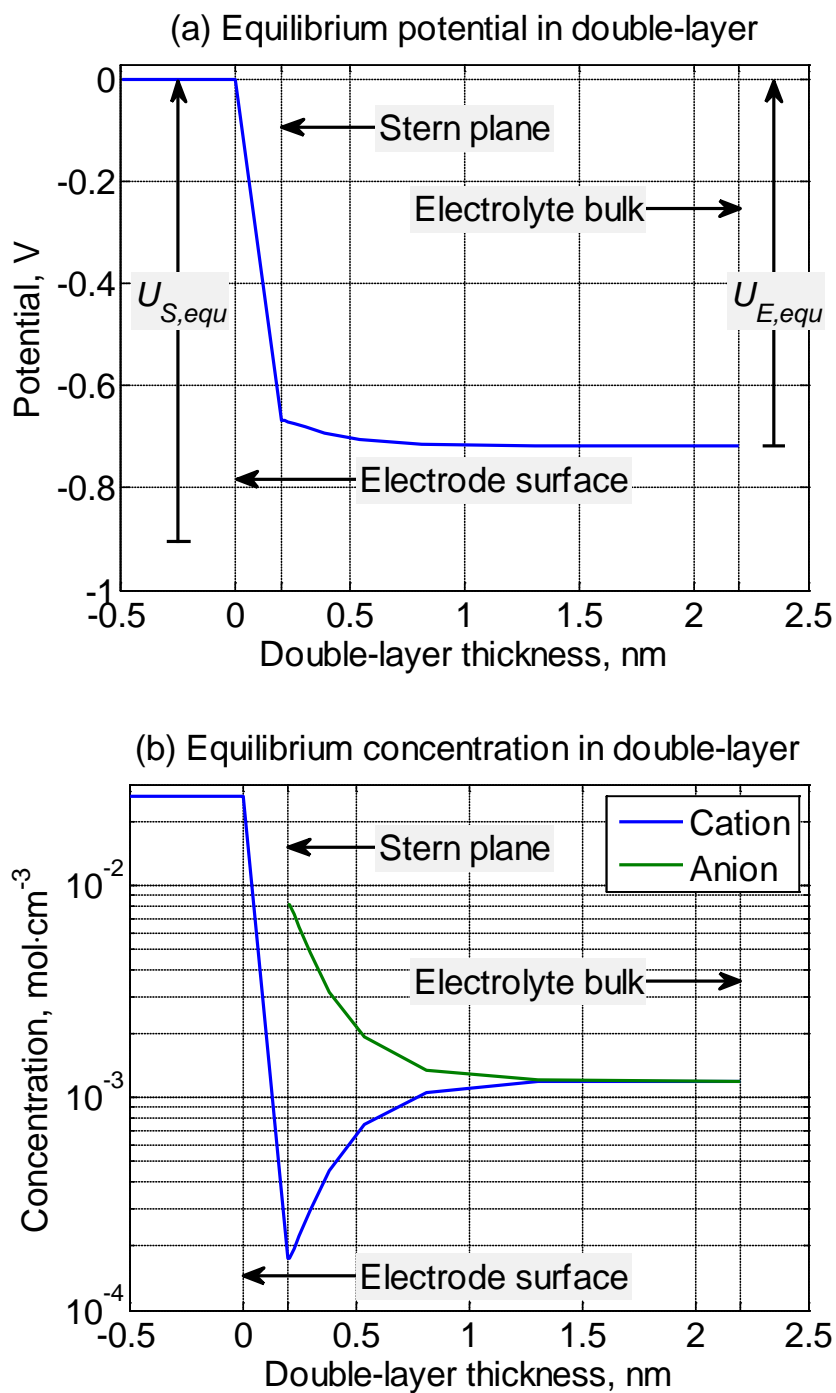
Figure 5-3 Equilibrium potential and ion concentration in the DL at anode side

The reaction equilibrium potential, $U_{S,equ}$, used for calculation is 0.91V, as in Figure 5-3 *(a)*. The difference between the solid potential and bulk, called the double-layer equilibrium potential, $U_{E,equ}$, is 0.72V, which results from variables like the solid phase lithium ion concentration, equilibrium potential, bulk concentration, and electrolyte permittivity. The first two variables are a function of SOC and different at anode and cathode. It should be noted that the equilibrium potential used in Butler-Volmer equation is the double-layer equilibrium potential. The difference between the reaction and the double-layer equilibrium potential for anode and cathode is plotted in Figure 5-4.
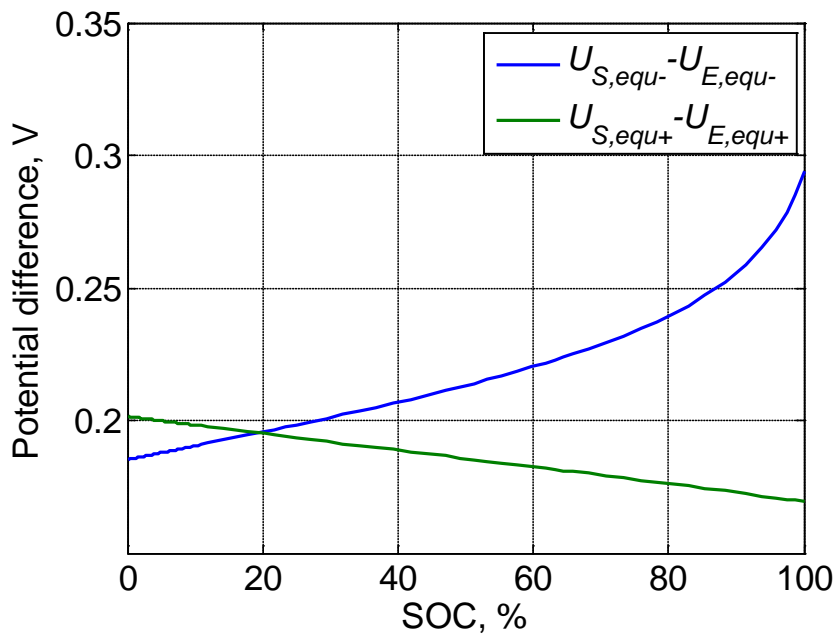

Figure 5-4 Difference between the two equilibrium potentials as a function of SOC

The equilibrium potential difference tends to follow the increase of SOC at anode side, while reversely with SOC at cathode. In order to analyze the effects of the SOC on the concentration in the DL, ion distributions in the DL at the equilibrium state are plotted in Figure 5-5 as function

of SOC. It is to recognize that the anion (PF_6^-) has higher concentration than cation (Li^+) because of the positive equilibrium potential. In addition, the lithium ion concentration becomes lower near the cathode surface, so a high chemical potential gradient is needed to maintain the same rate of ion flux, which leads to a high resistance compared to that in anode. Moreover, the ion concentration at the cathode is not affected by SOC, but the concentration at anode surface is heavily influenced because of the different percentages of changes of potentials at both electrodes. In fact, the ion concentration at 0% SOC and 100% SOC is six and thirty times higher than that at the cathode surface, which might be the cause for the lithium plating particularly built at anode side when at high SOC range.
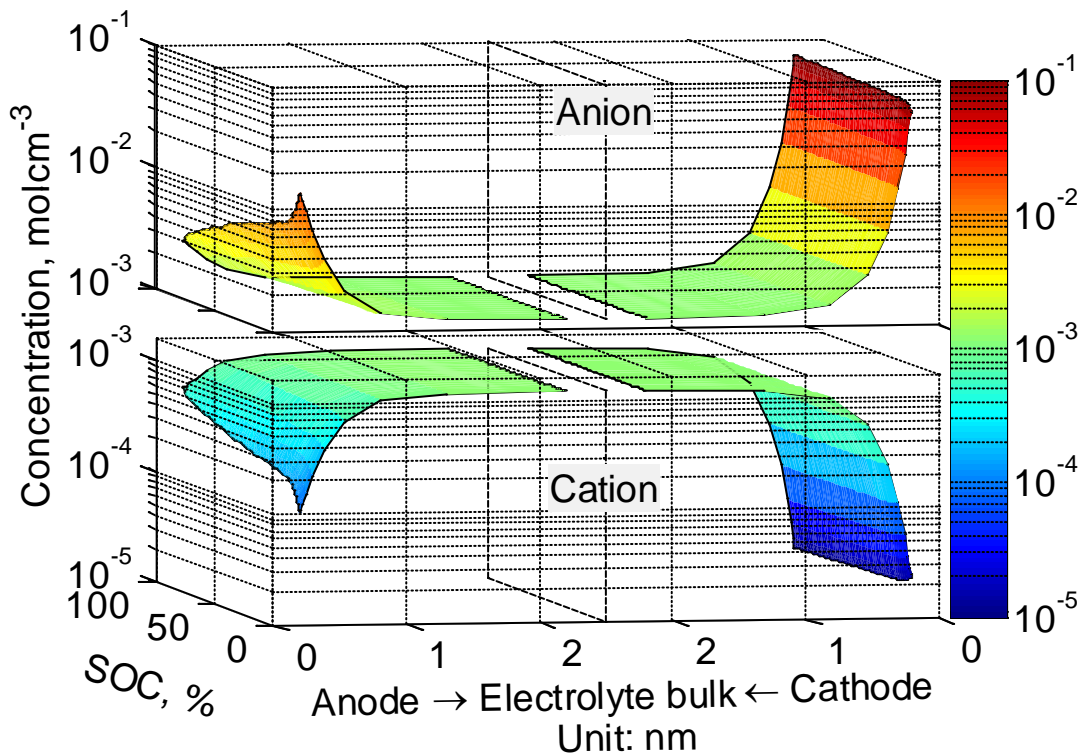

Figure 5-5 Equilibrium ion distributions in DL as function of SOC

5.3.2   DL at constant current loads

Calculated film resistances of the double layer on the anode (blue line) and cathode (green line) as well as the total resistance as a function of current densities are plotted in Figure 5-6. The results of the calculation shows that the film resistance on the anode DL (blue line) decreases with discharging DC current density, while that of cathode DL (green line) increases with discharging DC current density, and the variation of the total resistance is from two or three times larger than that at the lowest value, as plotted in red color.
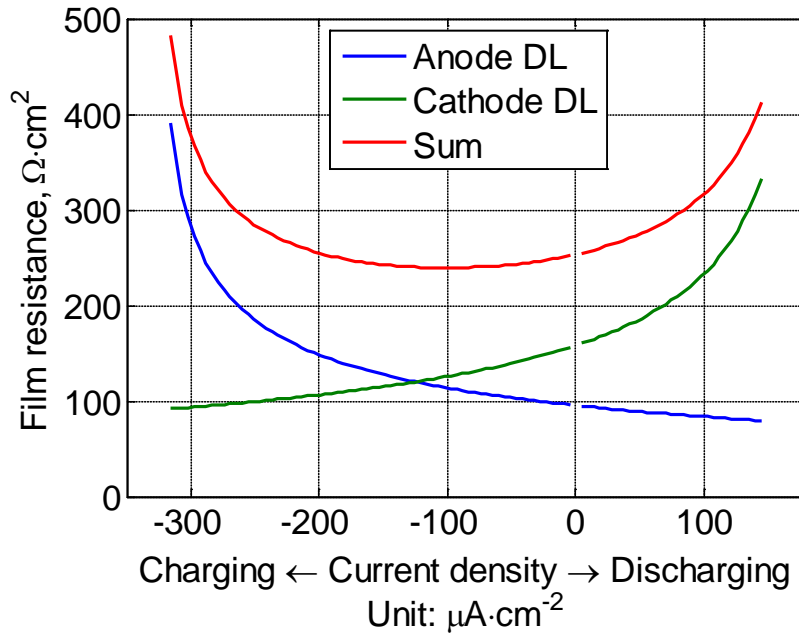
Figure 5-6 Film resistance of DL as function of DC density

The resistance values are different from that calculated using Butler-Volmer equation. The resistance by the Butler-Volmer equation is constant at small currents and increases when charging and discharging the cell with high currents. In addition, the minimum value was at the zero current. Conversely, the minimum value of the resistance considering the DL was not at zero current. The resistance was minimized in the anode DL when discharging with high

currents, but in the cathode when charging with high currents. These are caused from the direction of the current flow from solid to electrolyte and the associated equilibrium potentials that are positive. The sum of the DL resistance for two electrodes has shown its minimum value when charging the battery with $100\mu A \cdot cm^{-2}$. In fact, this current density depends on other parameters like SOC, particle sizes used for two electrodes, and volume of two electrodes. The resistance as a function of current density and the SOC is plotted in Figure 5-7 under assumption that the SOC is about 5%, and particle sizes and volumes of two electrodes are the same. It should be noted that the DL resistance is independent upon SOC when discharging because the resistance is dominantly determined by the cathode DL resistance. In addition, the DL resistance at charging has been always less than that at discharging when the absolute values of currents are the same. The DL resistance at low SOC and charging is much larger than that at high SOC.
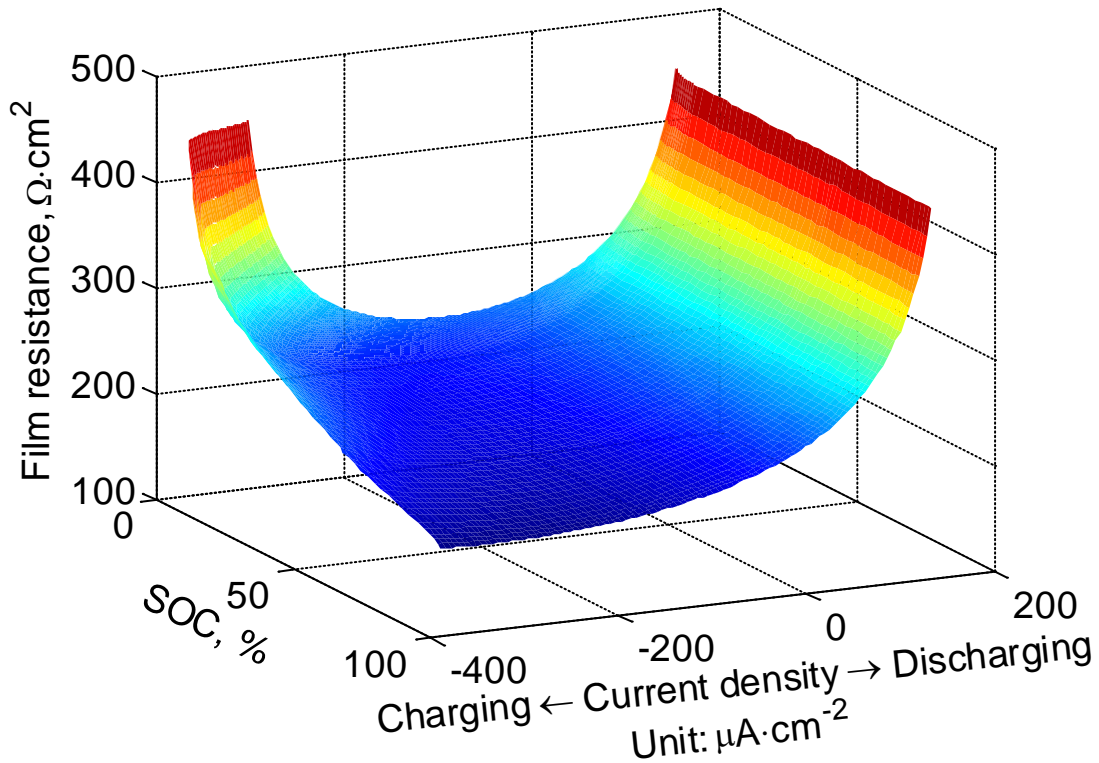
Figure 5-7 DL film resistance as function of SOC and current

5.3.3 DL with varying current loads

Analysis of the DL at equilibrium states shows that cation concentration near the surface of electrodes can be one several thousandth of anion concentration or even smaller dependent upon equilibrium potential and the permittivity of dielectric solvent. On the other hand, the cations move very fast in DL at a given ion flux that is determined by the current density, which implies that cations in a certain control volume will depart within a very short time when charging or discharging currents are not zero. Therefore, cations given in the previous time step completely departed the control volume that will be filled up with the new cations in the current time step. The lithium ion conservation equation (5-10) is replaced by a static equation obtained from the

charge conservation, which improves the numerical accuracy, even ignored dynamics for the cations:

$$\frac{\partial}{\partial r}(r^2 \cdot N_{d+} - r^2 \cdot N_{d-}) = 0$$

$$\frac{\partial c_{d-}}{\partial t} = -\frac{1}{r^2} \cdot \frac{\partial(r^2 \cdot N_{d-})}{\partial r}$$

(5-19)

The potential response of the anode DL at an AC current load with a frequency of 100Hz using equation (5-19) is shown in Figure 5-8, in which the effects of the cations are ignored. After half of the first period, the potential has always taken a steady.

Figure 5-8 Anode DL dynamic response
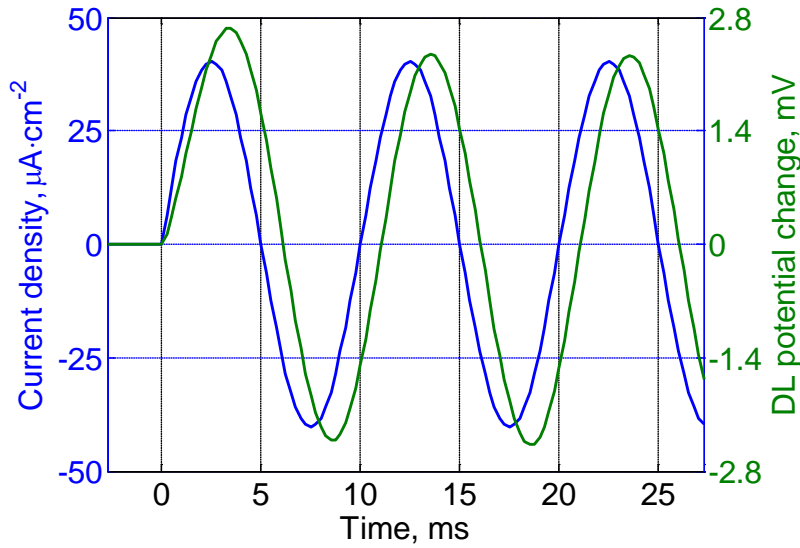
Potential responses of the anode DL at AC current densities with different frequencies are plotted in x-y plane, as shown below in Figure 5-9 , which show different shapes of ellipses. The slope of the major axis of the ellipse is the real part of the DL resistance while the eccentricity represents the phase delay of the system. The calculation shows that the real part of resistance

decreases with increasing frequency, while the phase delay gets small when the frequency goes either low or high, but relatively high for the range of medium frequency.
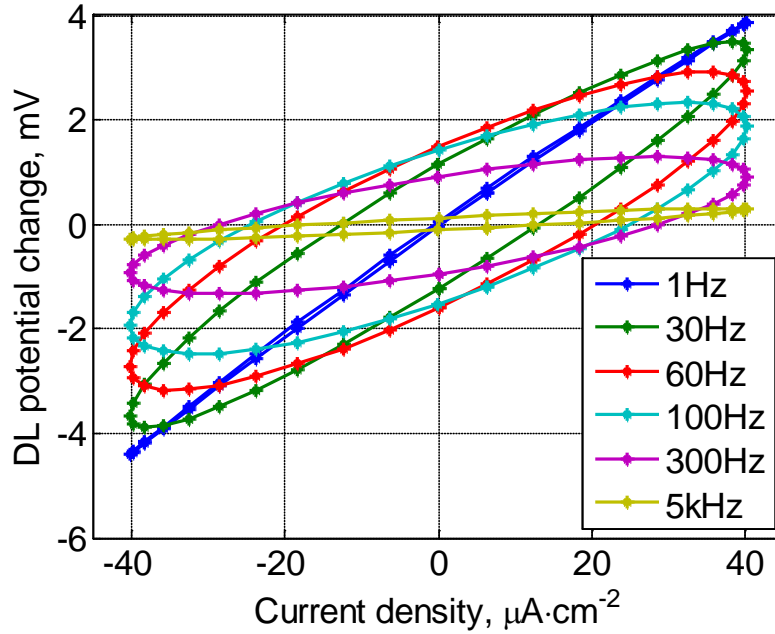

Figure 5-9 AC current with different frequencies versus potential in Anode DL

Based on the relationship between the AC current and potential, the Nyquist plot of impedances of the anode DL is shown in Figure 5-10. The impedance shows a shape of a semicircle when the frequency varies from 1Hz to 10kHz.
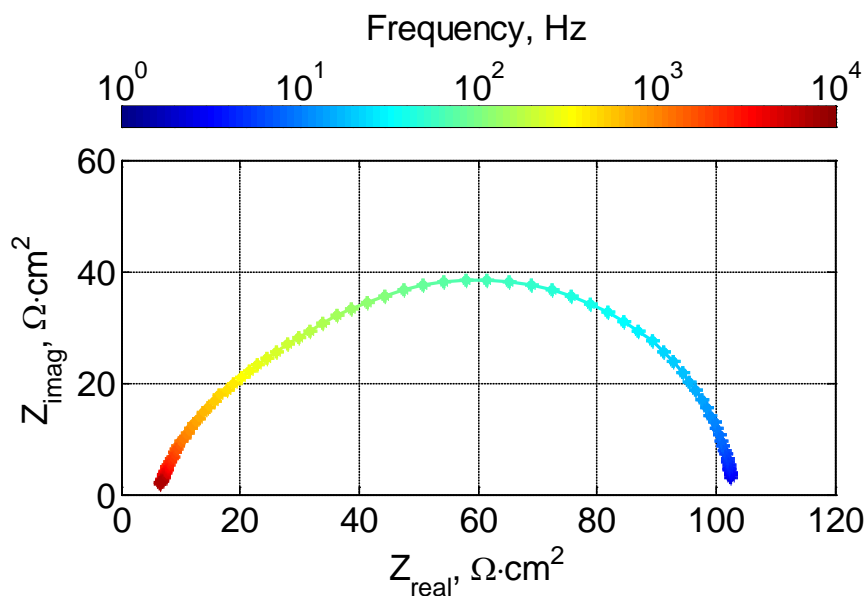
Figure 5-10 Nyquist plot of anode DL impedance

5.3.4   Bulk

Electrolyte bulk is the region where the same number of cations and anions are present in every control volume, so it should be overall electrically neutral. However, both ions are not paired in the region and move separately. Since the cations is more generated or absorbed than anions in the DL, more cations are crossing the boundary between the DL and the bulk or vice versus. Corresponding numbers of anions depart or enters the control volume to keep the neutrality.

Distribution of ion concentration and ion fluxes in electrolyte bulk at 0.1, 4.7 and 62.7sec during discharging and at 102.3sec during resting are calculated and plotted in Figure 5-11, where the direction of ion movements are marked with lines or half arrow, which color and length indicate the magnitude of flux. It is to recognize that the ion concentration (a) at 0.1sec

shortly after discharging is uniformly distributed. Both ions are moving in opposite directions, where anions move toward anode, while cations do toward cathode, which is caused by the electrostatic potential gradient. The magnitude of anions flux is larger than that of cation flux at the beginning of discharge simply because of the high ion mobility of the anion. As the anions do not participate in any reactions taking place in both electrodes, the transported anions are accumulated more in anode and less in cathode. As a result, a concentration gradient is formed. This concentration gradient causes a diffusion force subject to the ions, so that cations are accelerated and the flux gets increased. Conversely, anions are decelerated and the flux becomes less, as shown in (b).

At 62.7sec, the concentration distribution reaches a steady state, where the net flux of anion becomes zero, but the flux of cation becomes the highest, as shown in (c), which implies that the ionic current in the bulk is only determined by cation flux. At 102.3sec during resting, where no load current is applied, a concentration gradient is still present and drives ions until evenly distributed. Thus, both cations and anions move in the same direction, which fluxes have the same magnitude and result in no net current flow in bulk, as shown in (d). In addition, the ion flux is large in separator region but small near current collectors since the ions are generated and accumulated in the composite electrodes.
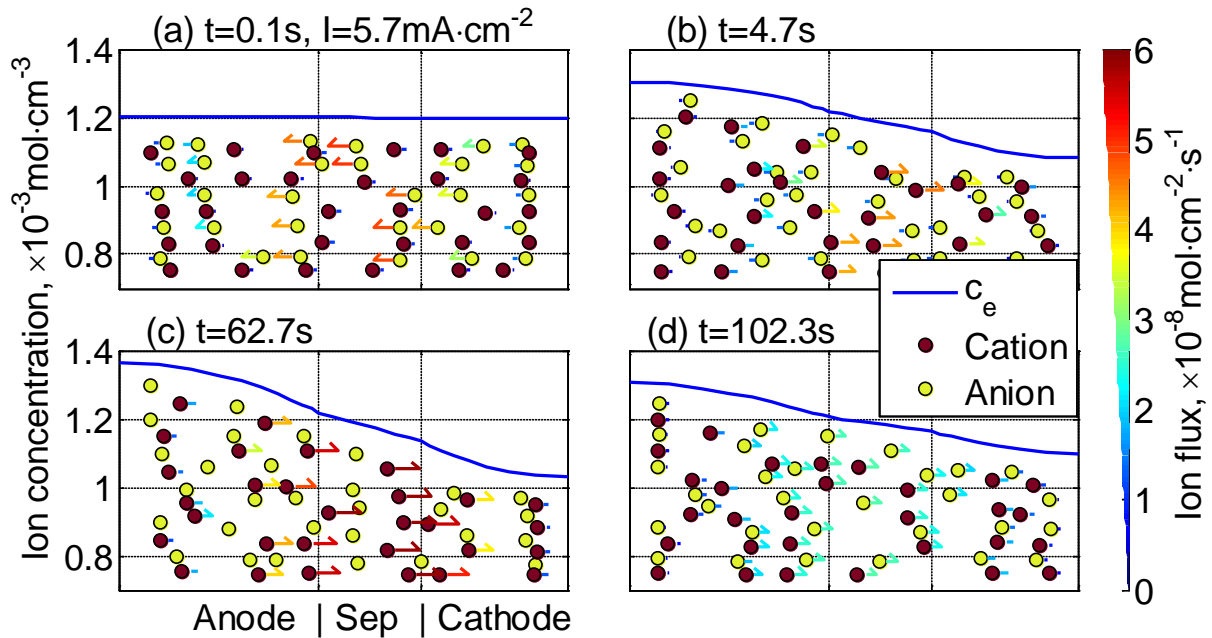
Figure 5-11 Ion concentration and ion fluxes in electrolyte bulk

The transference number is generally defined as a contribution of ion species to a total current flow. Transference number for cations and the associated ion fluxes during discharging and resting are plotted in Figure 5-12 as a function of time, where a step discharge current (the first plot with Blue line) is applied. The transference number is no more constant. At the instant where the discharging current is applied, the transference number increases to 1/7 instantly because the choson mobility of anions is six times higher than that of cations. Accordingly, the anion and the cation flux jumps to one seventh and six seventh of the total flux, respectively. Since the participation of the ions into current flow and resulting effects of the concentration gradients as described above, the anion flux gets decreased as the time is passing by, while the cation flux gets increased until the concentration gradient reaches its maximum.

117

When the current load is disconnected, there are ion fluxes caused by the concentration gradient present in bulk until evenly distributed. At the instant when the abrupt current change occurs, both fluxes have the same magnitude and decay according to the decreasing concentration gradient with a time constant determined by ions mobility. At the same time, transference number becomes infinite.
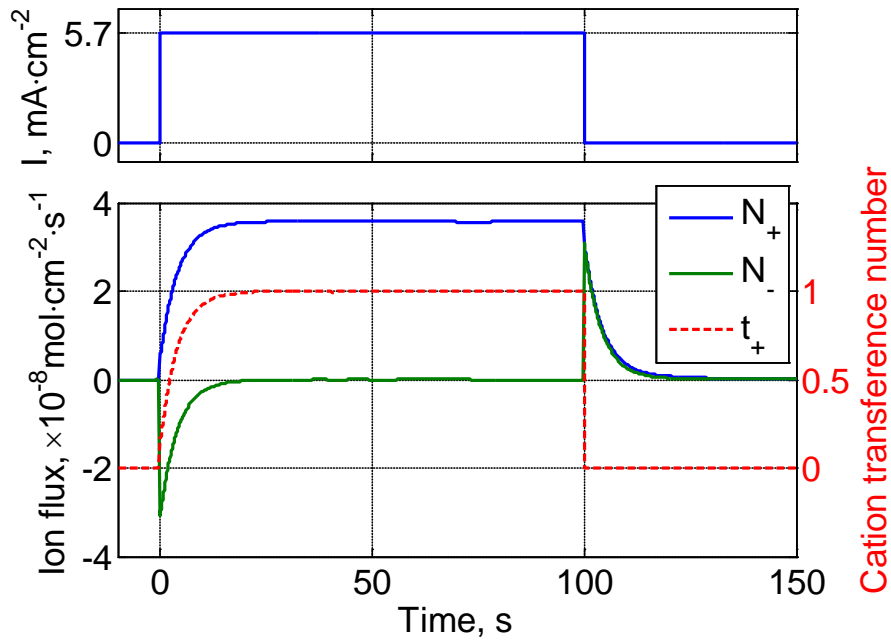
Figure 5-12 Average ion flux and transference number in bulk when discharging

5.4   Integration of the Model for DL and Bulk into Microcell and Validation

The microcell model described in previous chapters is modified to include sub-models for the DL and bulk. In order to analyze the frequency behavior, AC current is applied, which amplitude is 1A and a frequency range from 0.01Hz to 900Hz. SOC was set to 50%. The calculated and experimented responses of the AC current on the integrated model are plotted in the frequency

domain and Nyquist form, as shown in Figure 5-13. The experiments use the same battery used for validations of the microcells.

The calculated and experimented real and imaginary part of impedance is compared in Figure 5-13 (a). Both parts of the impedance tend to decrease when the frequency increases. The analysis shows that the responses can be divided in three frequency ranges: for the high frequency range (10Hz~1000Hz), where the ions mobility in double layer, permittivity and the electrode particle radius play the major role, for the medium frequency range (0.05Hz~10Hz), where ions mobility in bulk and active area are responsible for and for the low frequency (<0.05Hz), where ion diffusion coefficient in solid is responsible for. The associated Nyquist plot for impedance is shown in (b).
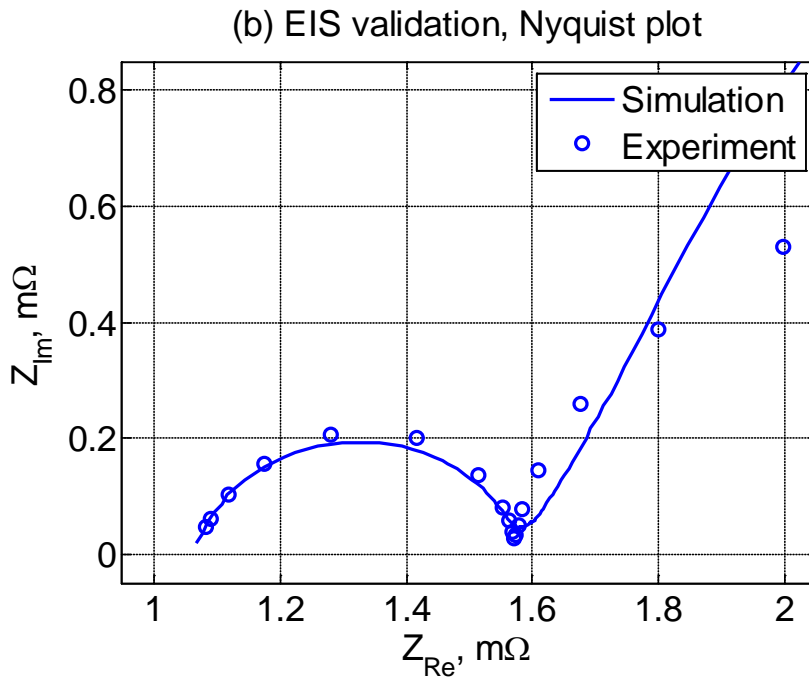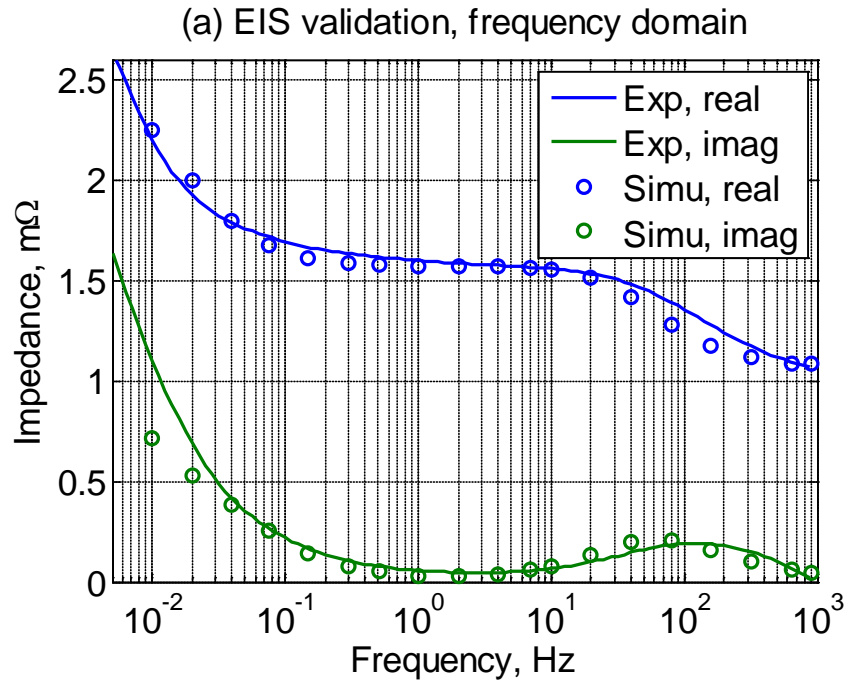
Figure 5-13 EIS validation

Since the low frequency behavior is mainly affected by solid phase diffusion that is a function of SOC, finding a set of parameters needed for validation in frequency domain is very

time consuming because some parameters like equilibrium potentials in both electrodes are immeasurable and inaccurate. Thus, comparisons are performed in time domain, as shown in Figure 5-14, where the cell is discharged with 1C. The results show a fairly good match between the simulation and experiment.
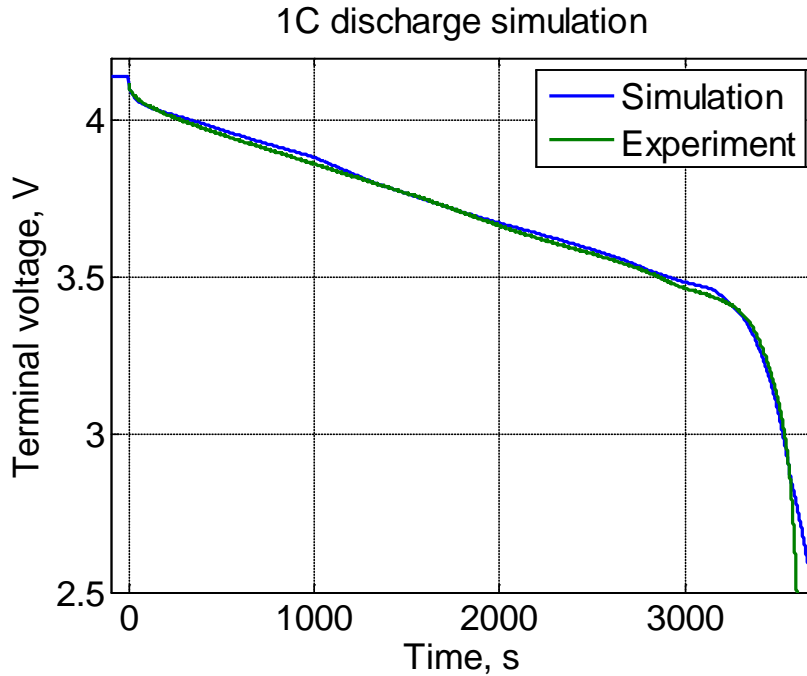
Figure 5-14 Comparison of discharging behaviors at 1C discharge

5.5   Summary

Measurement of impedances of battery is one of well-known methods to experimentally characterize properties of electrochemical devices including Lithium batteries. The measure impedance responses are generally fitted to a model that consists of linear and nonlinear electric components. This electric circuit model cannot represent physical behavior of the battery. On the on other hand, the current electrochemical model can provide internal physical behavior, but the

responses of the model does not consider the high frequency behavior resulting from the double layer. Therefore, a sub-model for the DL and bulk is newly developed and integrated into the electrochemical model for a pouch type LiPB. The integrated model is validated against experimental EIS and time response. The proposing model is capable of representing the responses at charging and discharging not only in time domain, but also in the wide range of frequency domain. The simulation results show several interesting findings as follows:

- The reaction equilibrium potential that represents energy of chemical bonds is not the same as the DL equilibrium potential used in the Butler-Volmer equation. The difference depends upon the equilibrium potential, SOC, and load condition.

- The cation concentration near to the electrode surface is much lower than that in the bulk, while the anion concentration is higher than that in bulk.

- The cations concentration near to the electrode surface on anode side at 0% and 100% SOC is six and thirty times higher than that at the cathode surface, which might be one of the causes for forming the lithium plating, particularly on the anode side when the SOC is high.

- The DL resistance is independent upon SOC when discharging because the DL resistance on the cathode side is dominant. DL resistance during the charging is always smaller than that during discharging if the magnitude of currents is the same.

- The initial transference number in bulk is substituted with new values as the time passes by. The number gradually increases and finally becomes 100% within one minute during charging or discharging, even though the electrolyte is electrically neutral.

122

- DL is responsible for the high frequency response that forms the low semi-circle of Nyquist plot from EIS measurement, while the bulk and diffusion in the electrode determine the medium and the low frequency response respectively that forms the linear increasing part of the Nyquist plot.

The proposing high frequency electrochemical model needs a wide range of experimental validation for charging and discharging at different current rate, SOC, and temperature.

6   Conclusion

Energy efficiency of future power systems can be substantially improved using energy storage that can capture energy and retrieve energy that is otherwise dissipated. Batteries are the most preferred energy storage because of high columbic efficiency, high energy and power density. Among different batteries technologies, Li-polymer battery is mostly preferred because of its highest power and energy density. But the Li-ion battery can be quickly degraded and performances might drop fast and becomes unstable because of high ion transport and gradient of ion concentrations and the associated high heat generation in conjunction with varying environmental operating conditions. The working mechanism of a cell is very complex and hard to understand in details, which presents one of technical barriers that prevents from optimal design of a cell and systems. Terminal behavior of a battery cell can be described in three different ways, using empirical equations, equivalent circuit components, or electrochemical-thermal principles.

This work focused on electrochemical-thermal-DL model since it is a physical based model that can more accurately predict the battery behavior and help to understand the mechanism. Major contribution of my research can be summarized in three parts as follow:

Firstly, a high resolution quasi-three dimensional model is developed for a pouch type of lithium polymer cell with a chemistry of $LiMn_2O_4$/Carbon for electrodes. The model is constructed using a one dimensional microcell based on electrochemical and thermal principles and experimentally validated against static and dynamic performance of a cell. The model

developed is capable of representing not only current and voltage at the terminal tabs of a single cell but also distribution of ion concentrations, potentials, internal currents, and temperature when a battery is charged or discharged.

Secondly, the heat source term is one of crucial factors in not only optimizing a battery cell, but also modules and packs. However, theoretical formulation for the heat source terms has ignored either heat of mixing or enthalpy heating. Therefore, a new formulation is derived based on the energy conservation that includes both terms that are incorporated into electrochemical thermal model. The model is validated against experimental data using a calorimeter that was specially designed. The new calorimeter was designed two thermoelectric devices with a compensator for measurement errors and allows for dynamic measurements of the heat generation. The calorimeter was statically and dynamically calibrated using EIS and the dynamic errors are compensated using Kalman filter.

Finally, measurement of impedances of battery is one of well-known methods to experimentally characterize properties of electrochemical devices including Lithium batteries. The electric circuit model which is generally used in fitting the EIS cannot represent physical behavior of the battery. On the other hand, the current electrochemical model can provide internal physical behavior, but the responses of the model do not consider the high frequency behavior resulting from the DL. Therefore, a sub-model for the DL and bulk is newly developed and integrated into the electrochemical model for a pouch type LiPB. The integrated model is validated against experimental EIS and time response. The proposing model is capable of representing the responses at charging and discharging not only in time domain, but also in the wide range of frequency domain.

Future work will include broad validations of the high frequency model as function of SOC, high C rates, temperature and degradation factors like side reactions. The only differences between this high frequency model and classic electrochemical model are the DL equation and bulk equation, which are also the difficult part to validate. The effect of DL can be amplified in several ways. Firstly, symmetric coin cells having two electrodes of the same material can be used to measure the properties of specific electrode material and avoid the response curves of two electrodes overlapping to each other. Secondly, smaller porosity of composite electrode can reduce the ratio of electrode surface to electrode volume that will increase the current and potential drop in DL compare to that in bulk when studying the DL property. Thirdly, DL response is not linear at large current, which can be utilized to validate the model. Finally, changing the temperature can be used to control the reaction rate of electrodes and further help to validate the model.

Reference

[1]   M. Doyle, T. Fuller, and J. Newman, "Modeling of galvanostatic charge and discharge of the lithium/polymer/insertion cell," J. Electrochem. Soc., 140 (1993), pp. 1526-1533

[2]   T. F. Fuller, M. Doyle, and J. Newman, "Simulation and optimization of the dual lithium ion insertion cell," J. Electrochem. Soc., 141 (1994), pp. 1-10

[3]   V. Srinivasan and J. Newman, "Discharge model for the lithium iron-phosphate electrode," J. Electrochem. Soc., 151 (2004), pp. A1517-A1529

[4]   P. Albertus, J. Christensen, and J. Newman, "Experiments on and modeling of positive electrodes with multiple active materials for lithium-ion batteries," J. Electrochem. Soc., 156 (2009), pp. A606-A618

[5]   M. Doyle, T. Fuller, and J. Newman, "The importance of the lithium ion transference number in lithium/polymer cells," Electrochimica. Acta., 39 (1994), pp. 2073-2081

[6]   S. Stewart and J. Newman, "Measuring the salt activity coefficient in lithium-battery electrolytes," Electrochem. Soc., 155 (2008), pp. A458-A463

[7]   S. Steward and J. Newman, "The use of UV/vis absorption to measure diffusion coefficients in $LiPF_6$ electrolytic solutions," Electrochem. Soc, 155 (2008), pp. F13-F16

[8]   G. Nagarajan, J. Zee, and R. Spotnitz, "A mathematical model for intercalation electrode behavior: I. effect of particle-size distribution on discharge capacity," J. Electrochem. Soc., 145 (1998), pp. 771-779

[9]   L. Song and J. Evans, "Electrochemical-thermal model of lithium polymer batteries," J. Electrochem. Soc., 147 (2000), pp. 2086-2095

[10]   C. Chiasserini and R. Rao, "Energy efficient battery management," IEEE journal on selected areas in communications, 19 (2001), pp. 1235-1245

[11]   R. Darling and J. Newman, "Modeling side reactions in composite $Li_yMn_2O_4$ electrodes," J. Electrochem. Soc., 145 (1998), pp. 990-998

[12] T. Fuller, M. Doyle, and J. Newman, "Relaxation phenomena in lithium-ion-insertion cells," J. Electrochem. Soc., 141 (1994), pp. 982-990

[13] K. Smith and C. Y. Wang, "Solid-state diffusion limitations on pulse operation of a lithium ion cell for hybrid electric vehicles," J. Power sources, 161 (2006), pp. 628-639

[14] D. Rakhmatov, S. Vrudhula, and D. Wallach, "A model for battery lifetime analysis for organizing applications on a pocket computer," IEEE-VLSI, 11 (2003), pp. 1019-1030

[15] Y. Chen and J. Evans, "Heat transfer phenomena in lithium/polymer-electrolyte batteries for electric vehicle application," J. Electrochem. Soc., 140 (1993), pp. 1833-1838

[16] M. Doyle and Y. Fuentes, "Computer simulations of a lithium-ion polymer battery and implications for higher capacity next-generation battery designs," J. Electrochem. Soc., 150 (2003), pp. A706-A713

[17] G. Kim and K. Smith, "Multi-scale multi-dimensional model for better cell design and management," 1st international conference on advanced lithium batteries for automotive applications, Sep. (2008), pp. 15-17

[18] H. Noh, "Electrolyte for a lithium ion battery and a lithium ion battery comprising the same," U.S. Patent No.: US 7306880 B2, Apr, 2007

[19] J. Ying, C. Jiang, and C. Wan, "Preparation and characterization of high-density spherical $LiCoO_2$ cathode material for lithium ion batteries," J. Power Sources, 129 (2004), pp. 264-269

[20] J. Vetter, et al., "Ageing mechanisms in lithium-ion batteries," J. Power Sources, 147 (2005), pp. 269-281

[21] R. Marom, et al., "A review of advanced and practical lithium battery materials," J. Mater. Chem., 21 (2011), pp. 9938-9954

[22] B. Banov, A. Momchilov, and C. Julien, "Positive electrode design for advanced rechargeable lithium batteries," Proceedings of the International Workshop "Portable and Emergency Energy Sources – from Materials to Systems" Sep. (2005), pp. 16-22

[23] K. Kishida, et.al, "Microstructure of the $LiCoO_2$ (cathode)/$La_{2/3-x}Li_{3x}TiO_3$ (electrolyte) interface and its influences on the electrochemical properties," J. Acta Materialia, 55 (2007), pp. 4713-4722

[24] E. Peled, et.al, "The sei model-application to lithium-polymer electrolyte batteries," J. Electrochemica Acta, 40 (1995), pp. 2197-2204

[25] P. Jrora, et.al, "Comparison between computer simulations and experimental data for high-rate discharges of plastic lithium-ion batteries," J. Power Sources, 88 (2000), pp. 219-231

[26] K. Smith and C. Y. Wang, "Power and thermal characterization of a lithium-ion battery pack for hybrid-electric vehicles," J. Power sources, 160 (2006), pp. 662-673

[27] D. Grahame, "The electrical double layer and the theory of electrocapillarity," J. Chemical Reviews, 41 (1947), pp. 441-501

[28] M. Kilic and M. Bazant, "Steric effects in the dynamics of electrolytes at large applied voltages. II. Modified Poisson-Nernst-Planck equations," J. Physical Review E, 75 (2007), 021503

[29] I. Borukhov, D. Andelman, and H. Orland, "Adsorption of large ions from an electrolyte solution: a modified Poisson–Boltzmann equation," Electrochim. Acta, 46 (2000), pp. 221-229

[30] V. Srinivasan and C. Wang, "Analysis of electrochemical and thermal behavior of Li-ion cells," Electrochemical Soc., 150 (2003), pp. A98-A106

[31] J. Vetter, et.al., "Ageing mechanisms in lithium-ion batteries," J. Power Sources, 147 (2005), pp. 269-281

[32] S. Santhanagopalan, et.al, "Parameter estimation and life modeling of lithium-ion cells," J. Electrochem. Soc., 155 (2008), pp. A345-A353

[33] D. MacNeil, Z. Lu, Z. Chen, and J. Dahn, "A comparison of the electrode/electrolyte reaction at elevated temperatures for various Li-ion battery cathodes," J. Power sources, 108 (2002), pp. 8-14

[34] G. Botte, V. Subramanian, and R. White, "Mathematical modeling of secondary lithium batteries," Electrochimica Acta, 45 (2000), pp. 2595-2609

[35] A. Awarke, M. Jaeger, O. Oezdemir and S. Pischinger, "Thermal analysis of a Li-ion battery module under realistic EV operating conditions," Int. J. Energy Res. (2012), DOI: 10.1002/er.2884

[36] V. Viswanathan, et.al., "Effect of entropy change of lithium intercalation in cathodes and anodes on Li-ion battery thermal management," J. Power Sources, 195 (2010), pp. 3720-3729

[37] D. Bernardi, E. Pawlikowski, and J. Newman, "A general energy balance for battery systems," J. Electrochem. Soc., 132 (1985), pp. 5-12

[38] J. Hong, H. Maleki, S. Al Hallaj, L. Redey, and J. Selman, "Electrochemical-calorimetric studies of lithium-ion cells," J. Electrochem. Soc., 145 (1998), 1489-1501

[39] W. Gu and C. Wang, "Thermal-electrochemical modeling of battery systems," J. Electrochem. Soc., 147 (2000), pp. 2910-2922

[40] S. Chacko and Y. Chung, "Thermal modeling of Li-ion polymer battery for electric vehicle drive cycles," J. Power Sources, 213 (2012), pp. 296-303

[41] L. Rao and J. Newman, "Heat-generation rate and general energy balance for insertion battery systems," J. Electrochem. Soc., 144 (1997), pp. 2697-2704

[42] K. Thomas and J. Newman, "Heats of mixing and of entropy in porous insertion electrodes," J. Power Sources, 119-121 (2003), pp. 844-849

[43] T. Hatchard, D. MacNeil, A. Basu, and J. Dahn, "Thermal model of cylindrical and prismatic lithium-ion cells," J. Electrochem. Soc., 148 (2001), pp. A755-A761

[44] Y. Ye, Y. Shi, N. Cai, J. Lee, and X. He, "Electro-thermal modeling and experimental validation for lithium ion battery," J. Power Sources, 199 (2012), pp. 227-238

[45] C. Forgez, D. Do, G. Friedrich, M. Morcrette, and C. Delacourt, "Thermal modeling of a cylindrical LiFePO$_4$/graphite lithium-ion battery," J. Power Sources, 195 (2010), pp. 2961-2968

[46] L. Song and J. Evans, "Electrochemical-thermal model of lithium polymer batteries," J. Electrochem. Soc., 147 (2000), pp. 2086-2095

[47] M. Xiao and S. Choe, "Dynamic modeling and analysis of a pouch type LiMn$_2$O$_4$/Carbon high power Li-polymer battery based on electrochemical-thermal principles," J. Power Sources, 218 (2012), pp. 357-367

[48] M. Doyle, T. Fuller, and J. Newman, "Modeling of galvanostatic charge and discharge of the lithium/polymer/insertion cell," J. Electrochem. Soc., 140 (1993), pp. 1526-1533

[49] K. Kumaresan, G. Sikha and R. White, "Thermal model for a Li-ion cell," J. Electrochem. Soc., 155 (2008) pp. A164-A171

[50] L. Cai and R. White, "Mathematical modeling of a lithium ion battery with thermal effects in COMSOL Inc. multiphysics (MP) software," J. Power Sources, 196 (2011), pp. 5985-5989

[51] K. Smith and C. Wang, "Power and thermal characterization of a lithium-ion battery pack for hybrid-electric vehicles," J. Power Sources, 160 (2006), pp. 662-673

[52] C. Zhu, X. Li, L. Song, and L. Xiang, "Development of a theoretically based thermal model for lithium ion battery pack," J. Power Sources, 223 (2013), pp. 155-164

[53] P. Northrop, V. Ramadesigan, S. De, and V. Subramanian, "Coordinate transformation, orthogonal collocation, model reformulation and simulation of electrochemical-thermal behavior of lithium-ion battery stacks," J. Electrochem. Soc., 158 (2011), pp. A1461-A1477

[54] X. Zhang, "Thermal analysis of a cylindrical lithium-ion battery," Electrochimica Acta, 56 (2011), pp. 1246-1255

[55] R. Yang, G. Chen, A. Kumar, and G. Snyder, "Transient cooling of thermoelectric coolers and its applications for microdevices," J. Fleurial, Energy Conversion and Management 46 (2005), pp. 1407-1421

[56] M. Doyle and Y. Fuentes, "Computer simulations of a lithium-ion polymer battery and implications for higher capacity next-generation battery designs," J. Electrochem. Soc., 150 (2003), pp. A706-A713

[57] T. Fuller, M. Doyle, and J. Newman, "Simulation and optimization of the dual Lithium ion insertion cell," J. Electrochem. Soc., 141 (1994), pp. 1-10

[58] M. Doyle, A. Gozdz, C. Schmutz, J. Tarascon, and J. Newman, "Comparison of modeling predictions with experimental data from plastic lithium ion cells," J. Electrochem. Soc., 143 (1996), pp. 1890-1903

[59] F. Laman, M. Matsen, and J. Stiles, J. Electrochem. Soc., "Inductive impedance of a spirally wound Li/MoS_2 cell," 133 (1986), pp. 2441-2446

[60]   N. Munichandraiah, L. Scanlon, and R. Marsh, "Surface films of lithium: an overview of electrochemical studies," J. Power Sources, 72 (1998), pp. 203-210

[61]   G. Ning, B. Haran, and B. Popov, "Capacity fade study of lithium-ion batteries cycled at high discharge rates," J. Power Sources, 117 (2003), pp. 160-196

[62]   R. Ramasamy, R. White, and B. Popov, "Calendar life performance of pouch lithium-ion cells," J. Power Sources, 141 (2005), pp. 298-306

[63]   J. Li, E. Murphy, J. Winnick, and P. Kohl, "Studies on the cycle life of commercial lithium ion batteries during rapid charge-discharge cycling," J. Power Sources, 102 (2001), pp. 294-301

[64]   C. Chen, J. Liu, and K. Amine, "Symmetric cell approach and impedance spectroscopy of high power lithium-ion batteries," J. Power Sources, 96 (2001), pp. 321-328

[65]   R. Bouchet, S. Lascaud, and M. Rosso, "An EIS study of the anode Li/PEO-LiTFSI of a Li polymer battery," J. Electrochem Soc., 150 (2003), pp. A1385-A1389

[66]   S. Zhang, K. Xu, and T. Jow, "EIS study on the formation of solid electrolyte interface in Li-ion battery," J. Electrochimica Acta, 51 (2006), pp. 1636-1640

[67]   S. Narayanan, D. Shen, S. Surampudi, A. Attia, and G. Halpert, "Electrochemical impedance spectroscopy of lithium-titanium disulfide rechargeable cells," J. Electrochem. Soc., 140 (1993), pp. 1854-1861

[68]   J. Lee, O. Nam, and B. Cho, "Li-ion battery SOC estimation method based on the reduced order extended Kalman filtering," J. Power Sources, 174 (2007), pp. 9-15

[69]   J. Xu, C. Mi, B. Cao, and J. Cao, "A new method to estimate the state of charge of lithium-ion batteries based on the battery impedance model," J. Power Sources, 233 (2013), pp. 277-284

[70]   I. Ong and J. Newman, "Double-layer capacitance in a dual lithium ion insertion cell," J. Electrochem. Soc., 146 (1999), pp. 4360-4365

[71]   M. Doyle, J. Meyers, and J. Newman, "Computer simulations of the impedance response of lithium rechargeable batteries," J. Electrochem. Soc., 147 (2000), pp. 99-110

[72]   D. Grahame, "The electrical double layer and the theory of electrocapillarity," J. Chem. Rev., 41 (1947), pp. 441-501

132

[73] K. Oldham, J. Electroanalytical Chemistry, "A Gouy-Chapman-Stern model of the double layer at a (metal)/(ionic liquid) interface," 613 (2008), pp. 131-138

[74] K. Yang, T. Ying, S. Yiacoumi, C. Tsouris, and E. Vittoratos, "Electrosorption of ions from aqueous solutions by carbon aerogel: an electrical double-layer model," J. Langmuir, 17 (2001), pp. 1961-1969

[75] I. Borukhov, D. Andelman, and H. Orland, "Adsorption of large ions from an electrolyte solution: a modified Poisson-Boltzmann equation," J. Electrochimica Acta, 46 (2000), pp. 221-229

[76] M. Kilic and M. Bazant, "Steric effects in the dynamics of electrolytes at large applied voltages. I. double-layer charging," J. Physical review E, 75 (2007), 021502, DOI: 10.1103/PhysRevE.75.021502

[77] M. Kilic and M. Bazant, "Steric effects in the dynamics of electrolytes at large applied voltages. II. modified Poisson-Nernst-Planck equations," J. Physical review E, 75 (2007), 021503, DOI: 10.1103/PhysRevE.75.021503

[78] M. Xiao, S. Choe, "Theoretical and experimental analysis of heat generations of a pouch type $LiMn_2O_4$/carbon high power Li-polymer battery," J. Power Sources, 241 (2013), pp. 46-55